Mathematical and Computational Applications

Mesh-Free and Finite Element-Based Methods for Structural Mechanics Applications

Edited by
Nicholas Fantuzzi

Printed Edition of the Special Issue Published in
Mathematical and Computational Applications

www.mdpi.com/journal/mca

MDPI

Mesh-Free and Finite Element-Based Methods for Structural Mechanics Applications

Mesh-Free and Finite Element-Based Methods for Structural Mechanics Applications

Editor

Nicholas Fantuzzi

MDPI • Basel • Beijing • Wuhan • Barcelona • Belgrade • Manchester • Tokyo • Cluj • Tianjin

Editor
Nicholas Fantuzzi
University of Bologna
Italy

Editorial Office
MDPI
St. Alban-Anlage 66
4052 Basel, Switzerland

This is a reprint of articles from the Special Issue published online in the open access journal *Mathematical and Computational Applications* (ISSN 2297-8747) (available at: https://www.mdpi.com/journal/mca/special_issues/str_mech_appl).

For citation purposes, cite each article independently as indicated on the article page online and as indicated below:

LastName, A.A.; LastName, B.B.; LastName, C.C. Article Title. *Journal Name* **Year**, *Volume Number*, Page Range.

ISBN 978-3-0365-0136-9 (Hbk)
ISBN 978-3-0365-0137-6 (PDF)

Contents

About the Editor

Nicholas Fantuzzi is a Senior Assistant Professor at the University of Bologna. He graduated with honors in Civil Engineering in 2009 and obtained his PhD in Structural Engineering and Hydraulics in 2013. He is the owner of the Italian National Academic Qualification as Associate Professor in Mechanics of Solids and Structures. He has been the teacher of the courses "Modelling of Offshore Structures" and "Advanced Structural Mechanics" in the International Master in Offshore Engineering since 2017. His research interests are mechanics of solids and structures, fracture mechanics, implementation of numerical methods for the design of structures, application of composite materials in offshore engineering, and design and strengthening of offshore components with numerical simulations. He is currently working on the application of finite element and mesh-free methods in solids mechanics and mechanics of materials. He is the Visiting Scholar at City University of Hong Kong (2018) and Visiting Professor at Zhejiang University (2019), Chongqing University (2019, 2020), and currently at University of Rijeka (2020). He has won international awards, as well as having been a Keynote speaker at four international conferences. Moreover, he has co-organized 14 international conferences on composite materials, composite structures and computational methods. He is also the Section Editor-in-Chief of "Mathematical and Computational Applications", MDPI Publishing, as well as being a reviewer for more than 90 international journals. He has written more than 100 international peer reviewed journal papers, 8 books and more than 70 abstracts in national and international conferences.

Mathematical and Computational Applications

MDPI

Editorial

Special Issue "Mesh-Free and Finite Element-Based Methods for Structural Mechanics Applications"

Nicholas Fantuzzi

Department of Civil, Chemical, Environmental, and Materials Engineering, University of Bologna, Viale del Risorgimento 2, 40136 Bologna, Italy; nicholas.fantuzzi@unibo.it

Received: 1 December 2020; Accepted: 2 December 2020; Published: 2 December 2020

Authors of the present Special Issue are gratefully acknowledged for writing papers of very high standard. Moreover, the reviewers are also acknowledged for providing punctual and detailed reviews that improved the original manuscripts. Finally, the Guest Editor would like to thank Professors Oliver Schütze and Gianluigi Rozza (Editors-in-Chief of the MCA) for the opportunity to publish this Special Issue and Everett Zhu for accurately managing the editorial process.

The present Special Issue aimed to present relevant and innovative research works in the field of numerical analysis. The problem of solving complex engineering problems has been always a major topic in all industrial fields, such as aerospace, civil and mechanical engineering. The use of numerical methods increased exponentially in the last few years due to modern computers in the field of structural mechanics. Moreover, a wide-range of numerical methods has been presented in the literature for solving such problems. Structural mechanics problems are dealt with by using partial differential systems of equations that might be solved by using the two main classes of methods: Domain-decomposition methods, or the so-called finite element methods, and mesh-free methods where no decomposition is carried out. Both methodologies discretize a partial differential system into a set of algebraic equations that can be easily solved by computer implementation. The aim of the present Special Issue was to present a collection of recent works on these themes and a comparison of the novel advancements of both worlds in structural mechanics applications.

This Special Issue collects 10 (ten) contributions from several countries and topics all within the field of numerical analysis. This Special Issue is devoted to scientists, mathematicians and engineers who are investigating recent developments in analysis and state-of-the-art techniques on mathematical applications in numerical analysis.

Mota et al. [1] presented an assessment on porous functionally graded plates. In particular, this work aimed to assess the influence of different porosity distribution approaches on the shear correction factor, used in the context of the first-order shear deformation theory, which in turn may introduce significant effects in a structure's behavior. To this purpose, porous functionally graded plates with varying composition through their thickness were carried out. The bending behavior of these plates was studied using the finite element method with two quadrilateral plate element models.

Bellora and Vescovini [2] discussed the implementation of a continuation technique for the analysis of nonlinear structural problems, which is capable of accounting for geometric and dissipative requirements. The present strategy can be applied for solving quasi-static problems, where nonlinearities can be due to geometric or material response. The present procedure has been demonstrated to be robust and able to trace the equilibrium path in structures characterized by complex responses. Several examples are presented and discussed for a combination of material and geometry nonlinearities.

The noise emitted by ships is one of the most important noises in the ocean, and propeller noise is one of the major components of ship noise. Ebrahimi et al. [3] carried out a calculation of propeller noise using numerical methods because evaluation of propeller noise in the laboratory, despite the high accuracy and good reliability, has high costs and is very time-consuming. Software for numerical

calculation of propeller noise, based on FW-H equations, was developed and the results were validated by experimental results.

Bacciocchi and Tarantino [4] presented a work on the study of natural frequencies of functionally graded orthotropic laminated plates using a finite element formulation. The main novelty of the research was the modeling of the reinforcing fibers of the orthotropic layers assuming a nonuniform distribution in the thickness direction. The Halpin–Tsai approach was employed to define the overall mechanical properties of the composite layers starting from the features of the two constituents (fiber and epoxy resin). The analyses were carried out in the theoretical framework provided by the first-order shear deformation theory (FSDT) for laminated thick plates. Nevertheless, the same approach was used to deal with the vibration analysis of thin plates, neglecting the shear stiffness of the structure. This objective was achieved by properly choosing the value of the shear correction factor, without any modification in the formulation.

Patel et al. [5] presented a trans-disciplinary, integrated approach that used computational mechanics experiments with a flow network strategy to gain fundamental insights into the stress flow of high-performance, lightweight, structured composites by investigating the rostrum of paddlefish. The evolution of the stress in the rostrum was formulated as a network flow problem, which was generated by extracting the node and connectivity information from the numerical model of the rostrum. The changing kinematics of the system was provided as input to the mathematical algorithm that computes the minimum cut of the flow network. The flow network approach was verified using two simple classical problems.

Uzun and Civalek [6] presented the free vibration behaviors of various embedded nanowires made of different materials. The investigation was carried out by using Eringen's nonlocal elasticity theory. Silicon carbide nanowire (SiCNW), silver nanowire (AgNW) and gold nanowire (AuNW) were modeled as Euler–Bernoulli nanobeams with various boundary conditions such as simply supported (S-S), clamped simply supported (C-S), clamped–clamped (C-C) and clamped-free (C-F). The interactions between nanowires and medium were simulated by the Winkler elastic foundation model. The Galerkin weighted residual method was applied to the governing equations to gain stiffness and mass matrices. In addition, the influence of temperature change on the vibrational responses of the nanowires were also pursued as a case study.

As required by regulations, finite element analysis can be used to investigate the behavior of joints that might be complex to design due to the presence of geometrical and material discontinuities. The static behavior of such problems is mesh dependent; therefore, these results must be calibrated by using laboratory tests or reference data. Once the finite element model is correctly setup, the same settings can be used to study joints for which no reference is available. The work by Ouakka and Fantuzzi [7] analyzed the static strength of reinforced T-joints and sheds light on the following aspects: shell elements are a valid alternative to solid modeling; the best combination of element type and mesh density for several configurations is shown; the ultimate static strength of joints can be predicted, as well as when mechanical properties are roughly introduced for some FE topologies.

Li and Chen [8] presented a new complex variable method for stress and displacement problems in a noncircular deep tunnel with certain given boundary conditions at infinity. In order to overcome the complex problems caused by noncircular geometric configurations and the multiply-connected region, a complex variable method and continuity boundary conditions were used to determine stress and displacement within the tunnel lining and within the surrounding rock. The coefficients in the conformal mapping function and stress functions werre determined by the optimal design and complex variable method, respectively. The new method was validated by FLAC3D finite difference software through an example.

A Space-Time Finite Element Method (STFEM) is proposed by Dumont et al. [9] for the resolution of mechanical problems involving three dimensions in space and one in time. Special attention was paid to the nonseparation of the space and time variables because this kind of interpolation is well suited to mesh adaptation. For that purpose, a 4D mesh generation was adopted for space-time remeshing.

This original technique does not require coarse-to-fine and fine-to-coarse mesh-to-mesh transfer operators and does not increase the size of the linear systems to be solved, compared to traditional finite element methods. Computations were carried out in the context of the continuous Galerkin method. The present method was tested on linearized elastodynamics problems. The convergence and stability of the method were studied and compared with existing methods.

Finally, Moldenhauer [10] investigated two-dimensional differential equations of the kind $y' = f(x,y)$ that can be interpreted as a direction fields. Commercial finite element programs can be used for this integration task without additional programming, provided that these programs have options for the calculation of orthotropic heat conduction problems. The differential equation to be integrated with arbitrary boundaries was idealized as an finite element model with thermal 2D elements. Possibilities for application in the construction of fiber-reinforced plastics (FRP) arise, since fiber courses, which follow the local principal stress directions, make use of the superior stiffness and strength of the fibers.

Conflicts of Interest: The author declares no conflict of interest.

References

1. Mota, A.F.; Loja, M.A.R.; Barbosa, J.I.; Rodrigues, J.A. Porous Functionally Graded Plates: An Assessment of the Influence of Shear Correction Factor on Static Behavior. *Math. Comput. Appl.* **2020**, *25*, 25.
2. Bellora, D.; Vescovini, R. A Continuation Procedure for the Quasi-Static Analysis of Materially and Geometrically Nonlinear Structural Problems. *Math. Comput. Appl.* **2019**, *24*, 94.
3. Ebrahimi, A.; Seif, M.S.; Nouri-Borujerdi, A. Hydrodynamic and Acoustic Performance Analysis of Marine Propellers by Combination of Panel Method and FW-H Equations. *Math. Comput. Appl.* **2019**, *24*, 81. [CrossRef]
4. Bacciocchi, M.; Tarantino, A.M. Natural Frequency Analysis of Functionally Graded Orthotropic Cross-Ply Plates Based on the Finite Element Method. *Math. Comput. Appl.* **2019**, *24*, 52. [CrossRef]
5. Patel, R.; Riveros, G.; Thompson, D.; Perkins, E.; Hoover, J.J.; Peters, J.; Tordesillas, A. A Transdisciplinary Approach for Analyzing Stress Flow Patterns in Biostructures. *Math. Comput. Appl.* **2019**, *24*, 47. [CrossRef]
6. Uzun, B.; Civalek, O. Nonlocal FEM Formulation for Vibration Analysis of Nanowires on Elastic Matrix with Different Materials. *Math. Comput. Appl.* **2019**, *24*, 38. [CrossRef]
7. Ouakka, S.; Fantuzzi, N. Trustworthiness in Modeling Unreinforced and Reinforced T-Joints with Finite Elements. *Math. Comput. Appl.* **2019**, *24*, 27. [CrossRef]
8. Li, Y.; Chen, S. A Complex Variable Solution for Lining Stress and Deformation in a Non-Circular Deep Tunnel II Practical Application and Verification. *Math. Comput. Appl.* **2018**, *23*, 43. [CrossRef]
9. Dumont, S.; Jourdan, F.; Madani, T. 4D Remeshing Using a Space-Time Finite Element Method for Elastodynamics Problems. *Math. Comput. Appl.* **2018**, *23*, 29. [CrossRef]
10. Moldenhauer, H. Integration of Direction Fields with Standard Options in Finite Element Programs. *Math. Comput. Appl.* **2018**, *23*, 24. [CrossRef]

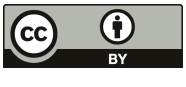

Mathematical and Computational Applications

MDPI

Article

Porous Functionally Graded Plates: An Assessment of the Influence of Shear Correction Factor on Static Behavior

Ana F. Mota [1,2,*], Maria Amélia R. Loja [1,2,3,*], Joaquim I. Barbosa [1,3] and José A. Rodrigues [1]

[1] CIMOSM, ISEL, Centro de Investigação em Modelação e Optimização de Sistemas Multifuncionais, 1959-007 Lisboa, Portugal; joaquim.barbosa@tecnico.ulisboa.pt (J.I.B.); jose.rodrigues@isel.pt (J.A.R.)
[2] Escola de Ciência e Tecnologia, Universidade de Évora, 7000-671 Évora, Portugal
[3] IDMEC, IST -Instituto Superior Técnico, Universidade de Lisboa, 1049-001 Lisboa, Portugal
* Correspondence: anafilipa.s.mota@gmail.com (A.F.M.); amelia.loja@isel.pt (M.A.R.L.)

Received: 6 March 2020; Accepted: 20 April 2020; Published: 24 April 2020

Abstract: The known multifunctional characteristic of porous graded materials makes them very attractive in a number of diversified application fields, which simultaneously poses the need to deepen research efforts in this broad field. The study of functionally graded porous materials is a research topic of interest, particularly concerning the modeling of porosity distributions and the corresponding estimations of their material properties—in both real situations and from a material modeling perspective. This work aims to assess the influence of different porosity distribution approaches on the shear correction factor, used in the context of the first-order shear deformation theory, which in turn may introduce significant effects in a structure's behavior. To this purpose, we evaluated porous functionally graded plates with varying composition through their thickness. The bending behavior of these plates was studied using the finite element method with two quadrilateral plate element models. Verification studies were performed to assess the representativeness of the developed and implemented models, namely, considering an alternative higher-order model also employed for this specific purpose. Comparative analyses were developed to assess how porosity distributions influence the shear correction factor, and ultimately the static behavior, of the plates.

Keywords: functionally graded materials; porosity distributions; first-order shear deformation theory; shear correction factor; higher-order shear deformation theory; equivalent single-layer approach

1. Introduction

Material science has undergone great evolution in recent years, representing an extremely important field for the development of many technological areas for several reasons, such as those related to a sustainable economic and environmental nature. The introduction of the functional gradient concept in the context of composite particulate materials has contributed to the design of advanced materials able to meet specific objectives, through spatial variation in composition and/or microstructure [1,2].

Functional gradient materials (FGMs) were developed in Japan in the late 1980s for thermal insulation coatings [2]. With more than three decades of history, and being a part of a wide variety of composite materials, materials with functional gradients continue to be the object of attention. This is due to their tailorability, arising from a gradual and continuous microstructure evolution and, consequently, of locally varying material properties in one or more spatial directions. Therefore, FGMs can be appropriately idealized to meet certain specifications [3,4].

Composite materials can generally be described as systems composed of a matrix and a reinforcement, the material properties of which surpass those presented by each constituent

individually [5]. The gradual and continuous evolution of their material properties provide FGMs with better mechanical behavior than traditional composite materials [6]. Among other characteristics possessed by some FGMs, such as low thermal conductivity and low residual stresses, these materials also make it possible to minimize the stress discontinuities of conventional laminated composites [5,7,8]. FGMs' high resistance to temperature and the absence of interface problems gives them great importance in several engineering applications, which is why these composite materials have been extensively studied and used in the past two decades in a wide range of science fields requiring improved mechanical and thermal performances [5–7]. This broad range of applications justifies the need to study and predict the responses of FGMs' components [9]. In the past year, Li et al. developed several studies involving, among other topics, a stability and buckling analysis of functionally graded structures such as cylinders and arches [10–14].

Considering the continuous mixture concept behind their composition, FGMs can be constituted of two or more material phases. Hence, the resulting local material properties depend on this mixture evolution, allowing for a design according to the desired functions and specifications [15]. From the literature, the most common FGMs are constituted of two material phases, often one ceramic and one metal [6,11].

The manufacturing process of sintering, which is common in the production of FGMs, is responsible for the formation of micro voids or porosities within the materials, making important the introduction of porosity effects at the structures' design stage [9]. The literature contains various studies which include dynamic and static analyses of functionally graded porous plates and beams [16–21]. In addition, there are several studies considering ring and arch structures, especially those developed by Li et al. in the past year [13,22–27].

Functionally graded porous materials (FGPs) combine both porosity and functional gradient characteristics, where the porosity may have a graded evolution across the volume, providing desirable properties for some applications (as in biomedical implants), and undesirable in others where voids may cause serious problems (as in the aeronautical sector). The change in porosity in one or more directions can be caused by local density effects or pore size alteration. Functionally graded porous materials possess a cell-based structure, which can be classified as open or closed (i.e., containing interconnected or isolated pores, respectively) [15].

Porous gradient materials also present a multifunctional character, where, among other aspects, one may highlight a high performance-to-weight ratio and resistance to shock; nevertheless, it is important to note that pores imply a local loss of stiffness. The latest advances in manufacturing processes allow the consideration of the development of porous materials with a functional gradient, using methods such as additive 3D printing. Thus, it becomes possible to design porous structures with designed variable stiffness, which can be customized for specific engineering applications, optimizing performance and minimizing weight [28]. Due to the relevant role that such materials have in a range of applications, it is important to have a wider perspective of the contexts where one can find them.

Mechanical or more generically structural components made of porous materials, bioinspired materials, can be designed for sensitive and very precise operating conditions—for example, robotic, prosthetic, and aeronautical components, among others [28]. Most of the materials used in engineering are dense; however, porous materials are also of great interest and applicability in fields such as in membranes [3]. Bioinspired materials thus have great potential for current technologies, as their unique characteristics allow them to meet various design requirements [28]. Natural or man-made, porous compacts or foams—the types of porous materials are many and diverse. Bones, wood, ceramics, and aluminum foams are just a few examples [29]. In the field of biomaterials, the inclusion of porosities allows diversification of their applicability, with ceramic and polymeric scaffolds being examples of this [3].

In the biomedical field, a bone implant must guarantee a functional gradient that mimics real bone stiffness variations. With functionally graded porous scaffolds it is possible to obtain the variations in mechanical and biological properties required for bone implants, as the presence of a porosity

gradient is imperative for bone regeneration. Thus, functionally graded porous scaffolds for bone implants are designed to achieve the ideal balance between porosity and mechanical properties [30]. Since bone implants have various requirements, it is important to have ceramic porous materials with a wide and diversified range of pore sizes and morphologies in order to accomplish these requirements. Therefore, different porous hydroxyapatite structures have been developed to mimic natural bone's bimodal structure [31]. Since implants with no porosity show weak tissue regeneration and implant fixation capability, the introduction of a pore distribution in these alloys' structures leads to bone-like mechanical properties, allowing cellular activity [32].

In another field [33], membranes produced according to the Fuji process present a structure with relatively wide pore surface, followed by a gradually tightening pore size and a clearing of pores, finishing with an isotropic structure. Thus, these membranes can be mentioned as an example of an asymmetric structure from the porosity perspective, being implemented in several applications, with filtration and medical diagnosis being some examples. Porous membranes are the object of research related to materials and structure optimization [34].

Membranes can also be used for gas separation applications, typically possessing a microporous substrate, a mesoporous intermediate layer (or more), and a microporous top layer (or more). Regarding materials, α-Al_2O_3 is the most frequent, but TiO_2, ZrO_2, SiC, and their combinations are also very common [35]. For industrial wastewater treatment applications, ceramic microfiltration membranes made of Al_2O_3, SiO_2, ZrO_2, TiO_2, and their composites present excellent behavior. These specific membranes possess multi-layered asymmetric structures, with a macroporous support followed by intermediate layers of graded porosity [36]. The use of ceramic membranes extends to catalytic membrane reactors due to the huge resistance to high temperatures and aggressive chemical environments. In this case, the membranes usually present disk-like, planar, tubular, and hollow fiber designs [37]. According to Sopyan et al., the material properties of porous ceramics (e.g., Young's modulus and flexural strength) depend exponentially on the ceramics' total porosity [31].

Secondary batteries technology uses porous membranes to isolate cathode and anode from each other, preventing a short circuit, and to allow the charge transport. Therefore, these membranes should be simultaneously excellent electric insulators and good ion conductors, presenting a great safety level. In this field of action there are microporous, ultrafiltration. and nanofiltration membranes, with organic polymers being the most used materials [34].

Metallic foams are another example of materials whose mechanical properties depend on the porosity characteristics. Recently, they have been gaining use among applications of aluminum and other alloys since the combination of properties intrinsic to metal alloys with the effects of porosity are of great interest, highlighting the low density and high energy absorption. The change in the porosity characteristics of these materials (e.g., pore size) makes it possible to obtain properties suitable for specific applications. Aluminum foams find use in structural applications, as well as automotive and aeronautics industries, as examples [38].

A well-defined spatial porosity gradient is a requirement of solid foams for some specific applications like filtration, energy adsorption, and tissue engineering. Therefore, control over porosity in terms of morphology, pore size, and pores' connectivity is a challenge in the development of fabrication processes, since these parameters have a great influence on the porous materials' performance [39]. In their work, Costantini et al. mentioned that a pore size gradient confers an increased strength and energy absorption to a material, and that this kind of material needs a more precise characterization of the porosity gradient concerning the mechanical properties [39].

Since pores can have different dimensions and distributions, porous materials can appear with different porosity gradients. In a typical rectangular plate, there are several possible porosity gradient configurations. Regardless of the specific distribution, the relevance should be placed on the correspondence to the design requirements [3], knowing that the heterogeneity and spatial gradient characteristic of porous materials will play an extremely important role in the resulting mechanical properties [40].

The Young modulus and shear modulus are strongly influenced by several factors, from the manufacturing process, to the size, shape, and distribution of the pores. Consequently, the analytical prediction of porous materials' properties is not simple because of the randomness present in their structures, and the need of a knowledge of the microstructure that is as accurate as possible in order to obtain a significant numerical prediction [29].

Concerning porosity distributions, Nguyen et al. [41] studied the mechanical behavior of porous FGPs. To this purpose they took into account two different porosity distributions, varying both through the thickness direction (namely, the so-called even and uneven distributions). Zhang and Wang [15] produced eight different porous material structures with different pore distributions, including gradient distributions, and subjected them to some mechanical tests in order to evaluate important materials properties like Young's modulus. With this work they developed techniques to estimate the effective Young's modulus of functionally gradient porous materials. Having verified that there is an obvious relation between this material property and porosity, the relationship between both is not necessarily linear. However, the experimental results constitute a good basis for validating material properties obtained through theoretical models.

With this introductory section, the importance of porous materials becomes clear, particularly regarding the development of porosity distribution models that best represent the effects on the respective effective material properties.

Hence, the present work presents three porosity distribution models, two of which are based on the reference literature, and respective estimates of material properties. For these cases, we performed a set of parametric studies focused on the static behavior of porous plates with a functional gradient in order to characterize the influence of the shear correction factor, associated with the use of the first-order shear deformation theory. These studies were performed via the finite element method considering an equivalent single layer approach. To the best of our knowledge, there are no previously published works focusing on the assessment of the influence of the shear correction factor in the static bending behavior of porous plates. Hence, this study addresses this, considering the characterization of the neutral surface deviation from the mid-plane surface, which also provides an illustrative measure of the medium's heterogeneity, typical of graded mixture and porous materials.

2. Materials and Methods

Considering the wide and varied number of applications of porous materials briefly discussed in the introductory section, the prediction of their mechanical properties is very relevant. Several models to predict the Young modulus of porous materials have recently been proposed, including linear, quadratic, and exponential models, although these are not suitable for porosities which are too low or too high [29]. Carranza et al. evaluated the Young modulus of metallic foams with fractal porosity distribution, and the respective estimates were close to the experimental results. In this way, they proved the expected effect, and verified that the appropriate choice of the porosity distribution model is an important factor [38].

2.1. Functionally Graded Materials

The flexibility in tailoring material properties makes FGMs very interesting for many applications in diverse engineering and science fields like bioengineering, mechanics, and aerospace.

The procedures for manufacturing FGMs are designed in order to obtain a specific spatial distribution of the constitutive phases. The continuous and gradual spatial distribution is responsible for the unique morphology and properties of these materials that make them stand out from others [1]. The gradual evolution of the phases can be varied, and there may even be different variations in more than one direction in the same FGM [2]. Figure 1 illustrates one example of material distribution though one direction of a dual-phase FGM.

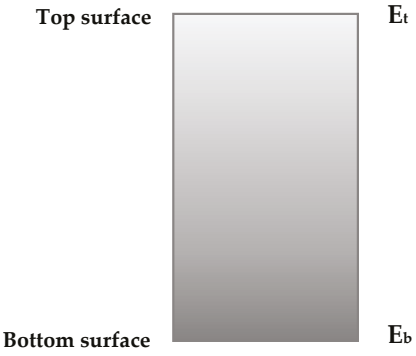

Figure 1. Example of dual-phase functional gradient material (FGM) mixture, with variation in one direction.

As a consequence of the gradual evolution of the bulk fractions and microstructure of FGMs, the respective macroscopic properties also present gradual changes. The gradual evolution of the material properties characteristic of FGMs makes it possible to design them in order to achieve specific mechanical, physical, or biological properties [1]. Since the volume fraction of the constituent phases can vary gradually in one or more directions, the present work considers the particular case of a dual-phase FGM plate in which this variation occurs in one only direction—specifically the thickness direction, as in [42]. In this case, the evolution of the volume fraction according to the direction of the z axis occurs according to the following power law:

$$V_f = \left(\frac{z}{h} + \frac{1}{2}\right)^p, \tag{1}$$

where h and z represent, respectively, the plate's thickness and the thickness coordinate, where the origin corresponds to the FGM plate's middle surface, thus $z \in [-h/2, h/2]$. Representing this material distribution, Figure 2 presents the volume fraction evolution through the thickness for some power law exponent values. As can be seen, the exponent p dictates the volume fraction behavior along the plate's thickness.

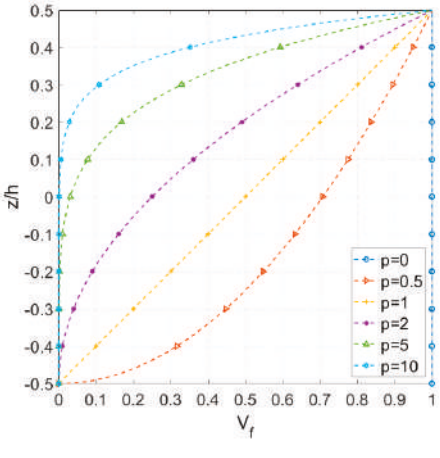

Figure 2. Evolution of the volume fraction through the thickness direction.

As the volume fraction of the phases of the constituents of FGMs is a function of the z coordinate, so too are the corresponding material properties. The effective material properties of an FGM can be estimated by the Voigt rule of mixtures, according to:

$$P_{FGM} = (P_t - P_b)V_{f_t} + P_b \tag{2}$$

where P_{FGM} is the FGM property, and P_t and P_b represent the corresponding property at top and bottom surfaces, respectively. This approach is suitable for FGMs whose phases are not very different from each other [43].

2.2. Porosity Distributions

Functionally graded porous materials combine characteristics of both FGMs and porous materials. Beyond the great rigidity–weight ratio, the incomparable mechanical properties they present explains why these distinctive materials are widely used in a wide range of diverse fields [44].

Despite great developments in manufacturing processes, the formation of micro-voids or porosities is still a fact [4], and in some specific applications this can be even desirable and designed for. Regardless of the specific case, as a consequence of these pores, the material's strength will become lower, and this should be included in mechanical behavior studies [44].

The present work considers three types of porosity distributions through the thickness, the first one being proposed by Kim et al. [45] and applied in several studies, such as those developed by Coskun et al. [46] and by Li and Zheng [22]. The last two were inspired in the uniform distribution mentioned by Du et al. [47], whose studies focus on open-cell metal foams rectangular plates considering different porosity distributions through the thickness.

- Porosity Model M1:

Concerning porous FGMs, Kim et al. [45] considered, among other things, a porosity distribution through the thickness given by:

$$\Phi(z) = \phi cos\left[\frac{\pi}{2}\left(\frac{z}{h} - \frac{1}{2}\right)\right], \tag{3}$$

where z represents the thickness coordinate, h represents the plate's thickness, and ϕ is the maximum porosity value.

Thus, the rule of mixtures is affected by this distribution and the effective Young modulus (E) and Poisson's ratio (υ) can be estimated as follows:

$$E(z) = \left[(E_t - E_b)\left(\frac{z}{h} + \frac{1}{2}\right)^p + E_b\right](1 - \Phi(z)), \tag{4}$$

$$\upsilon(z) = \left[(\upsilon_t - \upsilon_b)\left(\frac{z}{h} + \frac{1}{2}\right)^p + \upsilon_b\right](1 - \Phi(z)). \tag{5}$$

In both Equations (4) and (5), the indexes t and b indicate the top and bottom surfaces, respectively.

Figure 3 illustrates, in a normalized form, the porosity distribution through the thickness, showing an evolution from an absence of pores in the bottom surface to a maximum porosity in the top surface, and the normalized Young's modulus evolution through the thickness for different maximum porosity values and power law exponents, elucidating how this model of porosity distribution affects this material property.

The next two porosity distribution models were based on the uniform distribution referred to in [47].

In both models, the porosity coefficient (e_0) is given by Equation (6), and parameter β can be calculated through the relation in Equation (7).

$$e_0 = 1 - \frac{E_b}{E_t}, \tag{6}$$

$$\beta = \frac{1}{e_0} - \frac{1}{e_0}\left(\frac{2}{\pi}\sqrt{1-e_0} - \frac{2}{\pi} + 1\right)^2, \tag{7}$$

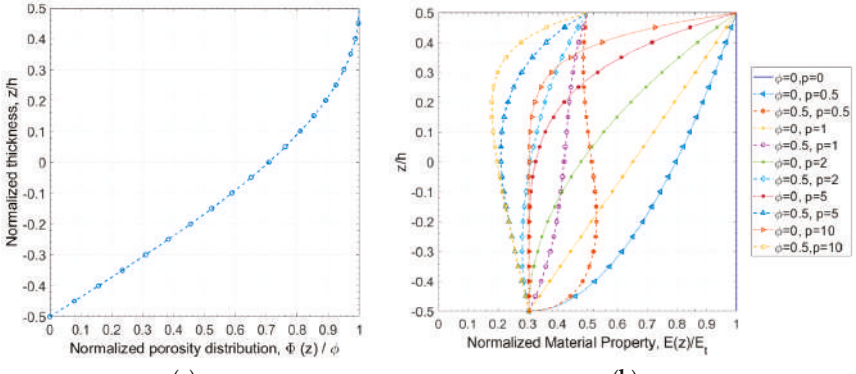

(**a**) (**b**)

Figure 3. Normalized: (**a**) porosity model M1 and (**b**) Young's modulus (E(z)) through the thickness direction.

- Porosity Model M2:

In this model, the material properties, namely Young's modulus and Poisson's ratio, are estimated by Equations (8) and (9), and the graph of the evolution of the normalized Young modulus through the thickness is presented in Figure 4.

$$E(z) = \left[(E_t - E_b)\left(\frac{z}{h} + \frac{1}{2}\right)^p + E_b\right](1 - e_0\beta), \tag{8}$$

$$v(z) = \left[(v_t - v_b)\left(\frac{z}{h} + \frac{1}{2}\right)^p + v_b\right](1 - e_0\beta). \tag{9}$$

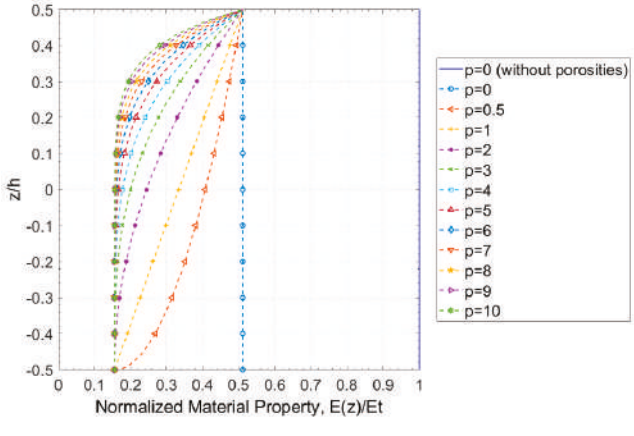

Figure 4. Variation of the normalized Young's modulus (E(z)) through the thickness for porosity model M2.

- Porosity Model M3:

This model introduces to the previous one a porosity gradient through the thickness, with the respective effective materials properties being given by:

$$E(z) = \left[(E_t - E_b)\left(\frac{z}{h} + \frac{1}{2}\right)^p + E_b\right]\left[1 - e_0\beta cos^2\left(2\pi\frac{z}{h}\right)\right], \tag{10}$$

$$v(z) = \left[(v_t - v_b)\left(\frac{z}{h} + \frac{1}{2}\right)^p + v_b\right]\left[1 - e_0\beta cos^2\left(2\pi\frac{z}{h}\right)\right]. \tag{11}$$

Figure 5 shows the variation of the normalized Young's modulus through the thickness. Note that the porosity distribution fluctuates between maxima and minima along the thickness.

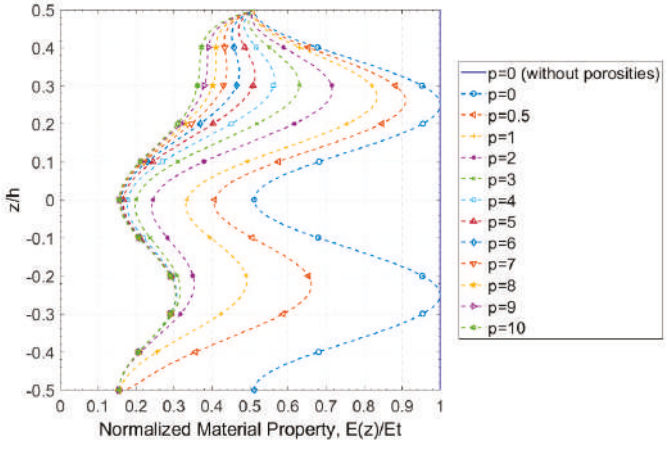

Figure 5. Porosity model M3: normalized Young's modulus (E(z)) through the thickness.

Note that on the upper surface the normalized Young's modulus takes the same value for all power law exponents evaluated once the equality $E(z) = E_t(1 - e_0\beta)$ is verified. On the opposite surface, Young's modulus is given by $E(z) = E_b(1 - e_0\beta)$, which justifies the fact that the corresponding $p = 0$ curve constitutes an exception from the others, since this particular case corresponds to a plate made up of a single phase whose Young's modulus is given by E_t, while in the remaining cases the bottom face corresponds to the phase with Young's modulus given by E_b.

In all three porosity distribution models, the shear modulus is estimated by:

$$G(z) = \frac{E(z)}{2(1 + v(z))}. \tag{12}$$

In Figures 3b, 4 and 5, the curve corresponding to the case of null power law exponent without porosity is also presented. In this case the represented material property is given by Equation (2), taking the value of E_t. Thus, the corresponding normalized form takes the value 1 through the entire plate thickness.

2.3. Constitutive Relation and Finite Element Models

The static behavior of porous plates with functional classification was evaluated for a set of studies through finite element analysis based on the first-order shear deformation theory (FSDT) and on third-order shear deformation theory (HSDT). According to FSDT the displacement field can be described by:

$$u(x, y, z) = u^0(x, y) + z{\cdot}\theta_x^0(x, y),$$

$$v(x,y,z) = v^0(x,y) + z{\cdot}\theta_y^0(x,y), \qquad (13)$$
$$w(x,y,z) = w^0(x,y),$$

where *u(x,y,z)*, *v(x,y,z)*, and *w(x,y,z)* are the displacements of a certain plate coordinate point, and u^0*(x,y)*, v^0*(x,y)* and w^0*(x,y)* represent the displacements of a mid-plane point associated to them. The normals to the mid-plane rotations are represented by θ_x^0 and θ_y^0, respectively. Thus, this model considers a total of five degrees of freedom per node, $q = \left[u^0, v^0, w^0, \theta_x^0, \theta_y^0\right]$. Considering small deformations, the elasticity kinematic relation leads to the following strain field, omitting dependencies for simplicity reasons:

$$\begin{array}{rrr} \varepsilon_x = \varepsilon_x^0 + z{\cdot}k_x^0 & & \gamma_{xz} = \gamma_{xz}^0 \\ \varepsilon_y = \varepsilon_y^0 + z{\cdot}k_y^0 & & \gamma_{yz} = \gamma_{yz}^0 \\ \gamma_{xy} = \gamma_{xy}^0 + z{\cdot}k_{xy}^0 & & \\ \varepsilon_x^0 = \frac{\partial u^0}{\partial x} & k_x^0 = \frac{\partial \theta_x^0}{\partial x} & \gamma_{xz}^0 = \theta_x^0 + \frac{\partial w^0}{\partial x} \\ \varepsilon_y^0 = \frac{\partial v^0}{\partial y} & k_y^0 = \frac{\partial \theta_y^0}{\partial y} & \gamma_{yz}^0 = \theta_y^0 + \frac{\partial w^0}{\partial y} \\ \gamma_{xy}^0 = \frac{\partial u^0}{\partial y} + \frac{\partial v^0}{\partial x} & k_{xy}^0 = \frac{\partial \theta_y^0}{\partial x} + \frac{\partial \theta_x^0}{\partial y} & \end{array} \qquad (14)$$

where ε_x, ε_y, and γ_{xy} correspond to the two in-plane normal strains and to the in-plane total shear strain, respectively. The interlaminar transverse shear strains are represented by γ_{yz} and γ_{xz}. This strain field is characterized by a null normal transverse strain ($\varepsilon_z = 0$), denoting thickness inextensibility. Since the FGM considered in the studies carried out can be considered as an isotropic material, the constitutive law governing the relationship between the stress and strain fields is given by:

$$\begin{bmatrix} \sigma_x \\ \sigma_y \\ \sigma_{xy} \\ \sigma_{yz} \\ \sigma_{xz} \end{bmatrix} = \begin{bmatrix} Q_{11} & Q_{12} & 0 & 0 & 0 \\ Q_{12} & Q_{22} & 0 & 0 & 0 \\ 0 & 0 & Q_{66} & 0 & 0 \\ 0 & 0 & 0 & k{\cdot}Q_{44} & 0 \\ 0 & 0 & 0 & 0 & k{\cdot}Q_{55} \end{bmatrix} \cdot \begin{bmatrix} \varepsilon_x \\ \varepsilon_y \\ \gamma_{xy} \\ \gamma_{yz} \\ \gamma_{xz} \end{bmatrix}. \qquad (15)$$

The coefficients Q_{ij}, provided by [48], stand for the elastic coefficients, which in the present work depend on the *z* coordinate due to the variation in material properties through the thickness direction:

$$\begin{array}{l} Q_{11} = Q_{22} = \frac{E_{FGM}(z)}{1-v_{FGM}^2(z)} \\ Q_{12} = \frac{v_{FGM}(z){\cdot}E_{FGM}(z)}{1-v_{FGM}^2(z)}, \\ Q_{44} = Q_{55} = Q_{66} = G_{FGM}(z). \end{array} \qquad (16)$$

The HSDT displacement field also considered in this work for comparison purposes was proposed by Kant et al. [49], and is given by:

$$\begin{array}{c} u(x,y,z) = u^0(x,y) + z{\cdot}\theta_x^0(x,y) + z^3{\cdot}\theta_x^*(x,y), \\ v(x,y,z) = v^0(x,y) + z{\cdot}\theta_y^0(x,y) + z^3{\cdot}\theta_y^*(x,y), \\ w(x,y,z) = w^0(x,y) + z^2{\cdot}w^*(x,y). \end{array} \qquad (17)$$

As can be observed, this higher-order displacement field not only allows for in-plane displacements that vary as cubic functions of the thickness coordinate, but it also allows for thickness extensibility. This higher-order theory was implemented for comparison purposes, but was not the main focus of the present work.

The finite element method was used for the study presented in this work. This method is widely used due to its great versatility, able to solve a wide range of physical problems ruled by differential equations. In this numerical method, the domain of a certain problem is discretized into elementary

subdomains, which obey continuity and equilibrium requirements between adjacent subdomains. The resolution of a problem by the finite element method can generically be described by three steps [49,50], as follows. After the pre-processing stage, where all aspects related to the domain discretization and topology, material and geometrical characteristics, loading and boundary conditions are accomplished, one proceeds to the analysis phase where the intended analysis is performed and primary variables are obtained. The results of this analysis can then be post-processed in order to obtain other derived physical quantities of interest in the third and final phase of this method. The plates analyzed in the present work had a rectangular geometry configuration (Figure 6) with a graded material distribution, as already mentioned.

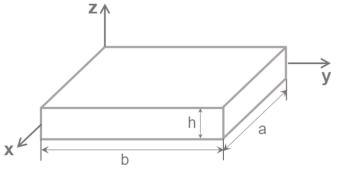

Figure 6. Plate geometry.

Taking into consideration their geometry, the plates were discretized into quadrilateral finite elements. To enable a more comprehensive study, we considered bilinear and biquadratic quadrilateral plate finite elements from the Lagrange family, as illustrated in Figure 7. The bilinear element (a) contained one node at each vertex (four nodes in total), while the biquadratic element (b) additionally contained a center node and one node at the midpoint of each side, resulting in a total of nine nodes. Each node possessed five degrees of freedom—three translations and two rotations associated to the plate mid-plane, as previously mentioned.

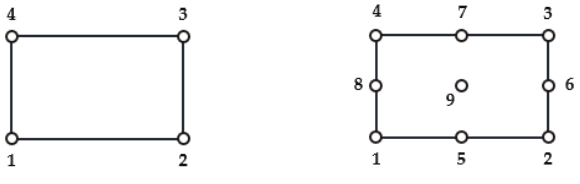

(**a**) (**b**)

Figure 7. Plate elements from Lagrange family: (**a**) bilinear element; (**b**) biquadratic element.

As the main aim of the present work is related to the assessment of the influence of the shear correction factor on the static bending of FGP plates, the procedure considered to achieve the global equilibrium equations to be solved was based on the minimization of the plates' potential energy. This mathematical formulation yields for each element a set of equilibrium equations. Considering the whole discretized domain where continuity and equilibrium aspects ensure the discretized model will be representative, we finally obtain the global equilibrium equation:

$$\{f\}^{global} = [K]^{global} \cdot \{u\}^{global}, \tag{18}$$

where $\{u\}^{global}$ denotes the problem solution (i.e., the generalized nodal displacements), $\{f\}^{global}$ represents the generalized forces applied to the plates, and $[K]^{global}$ is the global stiffness matrix. The solution of the problem is obtained after the imposition of the plates' boundary conditions.

2.4. Shear Correction Factor

The studies developed in this work are based on FSDT, which requires the introduction of a shear correction factor on the transverse shear components of the elastic stiffness coefficients matrix in order to redress the uniform transverse shear stresses/strains arising from the deformation kinematics based on the displacement field. Despite this need, FSDT-based models continue to be widely used in the modeling of structures, due to their lower computational cost when compared to other theories and also due to their applicability domain. It is possible to conclude that, even considering a bilinear element, results were very good when compared to other authors' alternative solutions and with biquadratic elements, while also having a lower computational cost. Regarding the homogeneous plates, the shear correction value considered was 5/6. However, the overall heterogeneity of FGMs due to the gradual evolution of their properties makes it desirable to calculate the correction factor for each specific case [6,43,51].

Shear correction factors determined through predictor–corrector procedures that use iteration processes depend on plate geometry, as well as boundary and load conditions. Therefore, the factors thus determined are limited to a given system and cannot be applied to different configurations. The use of energy considerations for the calculation of shear correction coefficients is quite common in studies involving laminated composite materials and FGMs [51]. Nguyen et al. [51] worked on this subject concerning FGMs, comparing the strain energies obtained from the average shear stresses and from the equilibrium to calculate the shear correction factors. Efraim and Eisenberg developed a shear correction factor depending on Poisson's ratio and the volume fractions of both material phases present in a functionally graded plate [52]. Working on FGPs, Li et al. [53] calculated the shear correction factor as a function of the power law exponent, thickness-to-length ratio (a/h), and of some constant coefficients that depend on the material phases involved.

The shear correction factor used in the present work (here represented by k) was estimated using a formulation similar to the one used by Singha et al. [54]. Accordingly, the reference surface used for the shear correction factor calculation was the neutral one and not the mid-surface as usual. To this purpose we considered an FGP with thickness h as illustrated in Figure 8, where z_{ms} and z_{ns} are the coordinates of a point in the thickness direction relative to the medium and neutral surfaces, respectively.

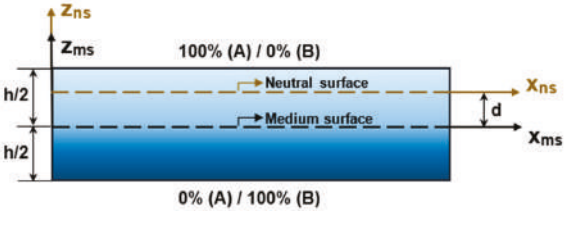

Figure 8. Medium and neutral surfaces.

According to this formulation, the shift of the neutral surface (d) is given by:

$$d = \frac{\int_{-h/2}^{h/2} E(z_{ms}) \cdot z_{ms}\, dz_{ms}}{\int_{-h/2}^{h/2} E(z_{ms})\, dz_{ms}}. \tag{19}$$

The shear correction factor is then derived from the equivalent energy principle, and can be determined by Equation (20) [54]:

$$k = \frac{\left(\int_{-\frac{h}{2}-d}^{\frac{h}{2}-d}\left(\int_{-\frac{h}{2}-d}^{z_{ns}} E(\xi)\cdot\,\xi d\xi\right) dz_{ns}\right)^2}{\int_{-\frac{h}{2}-d}^{z_{ns}} \overline{Q}_{55}\, dz_{ns}\cdot \int_{-\frac{h}{2}-d}^{\frac{h}{2}-d} \frac{\left(\int_{-\frac{h}{2}-d}^{z_{ns}} E(\xi)\cdot\,\xi d\xi\right)^2}{G(z_{ns})}}. \tag{20}$$

As applied to determine shear correction factor, all calculations carried out a posteriori were simply affected by a referential translation according to the coordinate vector $(0, 0, -d)$.

3. Results

The present section, dedicated to the presentation of results and their preliminary discussion, comprises a first verification study, after which a set of case studies considering different porosity distributions models are presented and analyzed concerning their influence on neutral surface shift, shear correction factor, and maximum transverse displacement.

3.1. Verification Studies

3.1.1. Shear Correction Factor

In the course of the literature review, no studies were found on the correction factor in the context of FGMs considering porosity distributions. For this reason, this first verification study regarding the approach applied to the correction factor determination was carried out considering a metal/ceramic functionally graded plate where the volume fraction of the ceramic phase is given by Equation (1). To this purpose, a square plate with unitary length and aspect ratio of 100 was considered, according to [43]. The results obtained for different power law exponents and Young's modulus ratios between both ceramic and metallic phases are presented in Table 1, showing an excellent agreement with the reference results for all parameter values considered.

Table 1. Shear correction factor for different material parameters.

p	E_c/E_m							
	1		**2**		**4**		**6**	
	k [43]	k	k [43]	k	k [43]	k	k [43]	k
0	5/6	0.8333	5/6	0.8333	5/6	0.8333	5/6	0.8333
1	5/6	0.8333	0.8320	0.8320	0.8305	0.8305	0.8305	0.8305
2	5/6	0.8333	0.8095	0.8095	0.7804	0.7804	0.7662	0.7662
5	5/6	0.8333	0.7891	0.7891	0.7175	0.7175	0.6643	0.6641
10	5/6	0.8333	0.7989	0.7989	0.7316	0.7318	0.6743	0.6746
p	E_c/E_m							
	8		**10**		**15**		**20**	
	k [43]	k	k [43]	k	k [43]	k	k [43]	k
0	5/6	0.8333	5/6	0.8333	5/6	0.8333	5/6	0.8333
1	0.8308	0.8308	0.8312	0.8312	0.8319	0.8319	0.8323	0.8323
2	0.7593	0.7594	0.7563	0.7563	0.7555	0.7556	0.758	0.7580
5	0.6238	0.6235	0.5923	0.5919	0.5381	0.5377	0.5046	0.5043
10	0.6262	0.6266	0.5856	0.5860	0.5073	0.5080	0.4513	0.4521

3.1.2. Porosity Distribution Model 1 (M1)

The first porosity model (M1) was submitted to verification studies. For this, and according to reference [6], an FGM square plate with 17.6 μm thickness and an aspect ratio of 20 was considered. Regarding the constituent materials, the Young moduli of the top and bottom surfaces were assumed

to be E_t = 14.4 GPa and E_b = 1.44 GPa respectively, and in this particular study, the Poisson ratio was considered constant, assuming the value of 0.38. The plate, simply supported, was considered under a uniformly distributed load with 100 kPa magnitude and was discretized in a 10 × 10 mesh of four node finite elements (Q4).

The normalized transverse displacement and the respective relative deviation to the reference, presented in Table 2, were obtained by Equations (21) and (22), respectively.

$$\overline{w} = \frac{E_b \cdot h^3}{q_0 \cdot a^4} w\left(\frac{a}{2}, \frac{b}{2}, 0\right), \tag{21}$$

$$\delta(\%) = \frac{\overline{w}^{present} - \overline{w}^{reference}}{\overline{w}^{reference}} \cdot 100(\%). \tag{22}$$

Table 2. Results of the porosity distribution model 1 (M1) verification study.

p	ϕ	$\overline{w}$	δ (%)
	0	4.220×10^{-3}	1.49
0	0.2	4.798×10^{-3}	0.43
	0.5	6.242×10^{-3}	−0.57
1	0.5	1.452×10^{-2}	0.26
5	0.5	2.685×10^{-2}	−0.18

The small relative deviations observed make it possible to conclude that there is very good agreement between the present model and the reference results, although a different approach was applied. In particular, the higher relative deviation occurs when considering an isotropic homogeneous material without porosities (p = 0, ϕ = 0).

3.2. Case Studies

In order to perform a set of parametric studies relevant for this work's objectives, we carried out simulations on a set of case studies, in which FGM square plates with 25 mm thickness and aspect ratio 20 were considered. The material properties involved in the studies presented in this section are given in Table 3, and the volume fraction of TiO_2 is given by Equation (1). The plates were considered simply supported and submitted to a uniform load with 100 kPa of magnitude.

Table 3. Material properties.

Material	Young's Modulus (GPa)	Poisson's Ratio
Aluminum (Al)	70	0.33
Titanium Oxide (TiO_2)	230	0.27

The case studies show the influence of the different porosity distribution models in the neutral surface shift, shear correction factor, and maximum transverse displacement for a range of power law exponents. The influence of finite element type used was also studied.

3.2.1. Influence on Neutral Surface Shift and Shear Correction Factor

In this subsection we present the studies performed to explore the effects of the porosity distribution on the neutral surface shift and shear correction factor.

- Porosity Distribution Model 1 (M1):

When considering porosities distributed according to model M1, it is important to evaluate how the maximum porosity value combined with the power law exponent affects the neutral surface shift and the

shear correction factor. For this purpose, the following sets of values were respectively considered for the maximum porosity value and for the exponent of the power law: $\phi = \{0,\ 0.1,\ 0.2,\ 0.3,\ 0.4,\ 0.5,\ 0.6\}$ and $p = \{0,\ 1,\ 2,\ 5,\ 10\}$. The results obtained are presented in Table 4, Figures 9 and 10.

Table 4. Porosities distribution M1: neutral surface' shift and shear correction factor.

ϕ	p	d (m)	d/h	k
0	0	0	0	5/6
	1	2.2222×10^{-3}	0.0889	0.8279
	2	2.7027×10^{-3}	0.1081	0.7828
	5	2.4631×10^{-3}	0.0985	0.7344
	10	1.7921×10^{-3}	0.0717	0.7499
0.1	0	-2.3222×10^{-4}	−0.0093	0.8316
	1	2.0233×10^{-3}	0.0809	0.8289
	2	2.4955×10^{-3}	0.0998	0.7843
	5	2.2257×10^{-3}	0.0890	0.7359
	10	1.5422×10^{-3}	0.0617	0.7505
0.2	0	-4.9832×10^{-4}	−0.0199	0.8297
	1	1.7903×10^{-3}	0.0716	0.8304
	2	2.2520×10^{-3}	0.0901	0.7865
	5	1.9481×10^{-3}	0.0779	0.7378
	10	1.2519×10^{-3}	0.0501	0.7513
0.3	0	-8.0630×10^{-4}	−0.0323	0.8275
	1	1.5138×10^{-3}	0.0606	0.8325
	2	1.9620×10^{-3}	0.0785	0.7894
	5	1.6190×10^{-3}	0.0648	0.7403
	10	9.1039×10^{-4}	0.0364	0.7522
0.4	0	-1.1669×10^{-3}	−0.0467	0.8248
	1	1.1805×10^{-3}	0.0472	0.8353
	2	1.6107×10^{-3}	0.0644	0.7934
	5	1.2227×10^{-3}	0.0489	0.7436
	10	5.0299×10^{-4}	0.0201	0.7534
0.5	0	-1.5948×10^{-3}	−0.0638	0.8217
	1	7.7050×10^{-4}	0.0308	0.8390
	2	1.1761×10^{-3}	0.0470	0.7988
	5	7.3631×10^{-4}	0.0295	0.7477
	10	8.5279×10^{-6}	0.0003	0.7546
0.6	0	2.1109×10^{-3}	0.0844	0.8177
	1	2.5421×10^{-4}	0.0102	0.8439
	2	6.2495×10^{-4}	0.0250	0.8059
	5	1.2505×10^{-4}	0.0050	0.7529
	10	-6.0425×10^{-4}	−0.0242	0.7560

Independent of the ϕ value, the neutral surface shift increased from $p = 0$ to $p = 2$, where it had its maximum value, then decreasing from $p = 2$ to $p = 10$. Additionally, for all maximum porosity values considered, except for the case where $\phi = 0.6$, the shear correction factor decreased for power law exponents between 0 and 5, increasing for the last transition from $p = 5$ to $p = 10$. This is explained by the fact that, for higher values of the power law exponent, the functionally graded plate approaches a homogeneous isotropic composition, and at the limit where p tends to infinity, the plate will consist of a single phase (aluminum in this case), so the value of the shear correction factor tends to the typical value 5/6.

When the maximum porosities took the values 0 or 0.1, the shear correction factor decreased from $p = 0$ to $p = 5$, increasing for higher values of power law exponent. For the remaining values of

maximum porosities this factor increased in the transition from $p = 0$ to $p = 1$, decreased from $p = 1$ to $p = 5$, and increased again until $p = 10$.

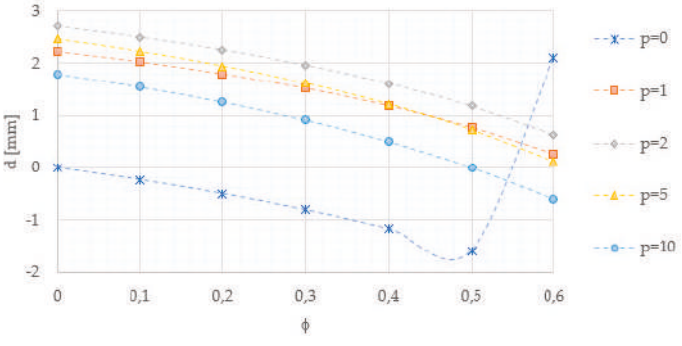

Figure 9. Porosity distribution model M1: evolution of neutral surface shift.

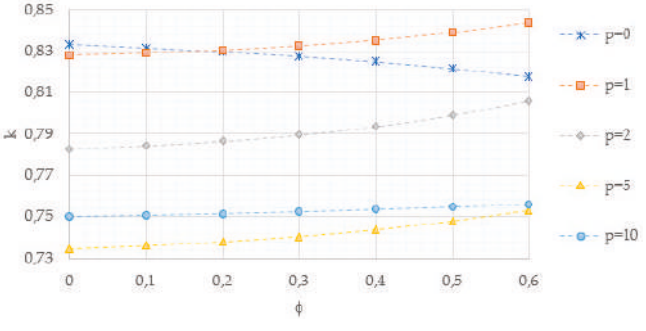

Figure 10. Porosity distribution model M1: evolution of shear correction factor.

In the case of an isotropic homogeneous plate ($p = 0$), the shear correction factor decreased when the maximum porosity values increased. This was also true for the neutral surface shift, excepting for the abrupt increase in the transition between $\phi = 0.5$ and $\phi = 0.6$. For other power law exponents, as the maximum porosity values increased the neutral surface shift decreased and the shear correction factor increased.

- Porosity Distribution Models 2 and 3 (M2 and M3):

Concerning these models, we evaluated the influence of the power law exponent, taking the set of integers from 0 to 10. Figures 11 and 12 show the evolution of neutral surface shift and shear correction factor, respectively, for both distribution models M2 and M3. The curves show a neutral surface shift behavior similar to the one observed in the previous study and a shear correction factor with a decreasing behavior up to $p = 5$, after which it increased with the exponent of the power law. This behavior was similar in both models. The porosity distribution M3 led to smaller neutral surface shifts, and the difference between both models increased with increasing power law exponent.

The porosity distribution model M3 generated lower values for the shear correction factor, with the difference between the two models decreasing with the increase in the power law exponent, as opposed to what was observed for the neutral surface shift.

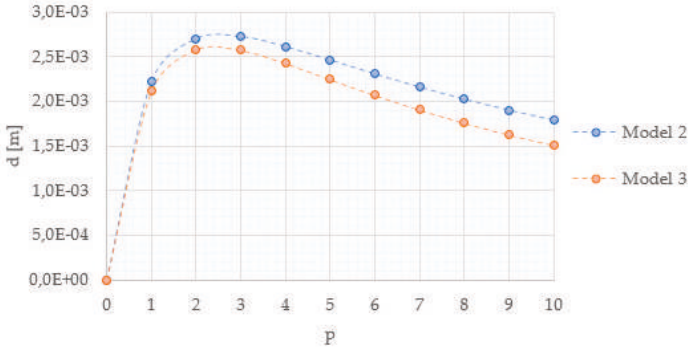

Figure 11. Porosity distribution models M2 and M3: evolution of neutral surface shift.

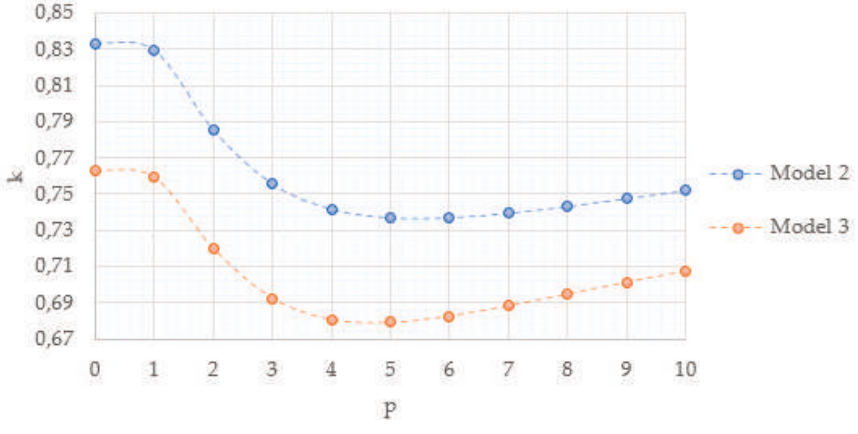

Figure 12. Porosity distribution models M2 and M3: evolution of the shear correction factor.

3.2.2. Influence on Absolute Maximum Transverse Displacement

In the studies presented in this section, the absolute maximum transverse displacement corresponds to the magnitude of the plate's center displacement given the considered boundary and load conditions. The results include both 4-node (Q4) and 9-node (Q9) plate finite element results, using the calculated shear correction factor (Section 2.4) here denoted by k^{calc} and the often used value of 5/6. The relative deviations presented were determined by the following equations:

$$\delta_{Q_4}(\%) = \frac{w^{Q_4}_{(k=\frac{5}{6})} - w^{Q_4}_{(k^{calc})}}{w^{Q_4}_{(k^{calc})}} \cdot 100(\%), \tag{23}$$

$$\delta_{Q_9}(\%) = \frac{w^{Q_9}_{(k=\frac{5}{6})} - w^{Q_9}_{(k^{calc})}}{w^{Q_9}_{(k^{calc})}} \cdot 100(\%). \tag{24}$$

In the convergence study presented for porosity distribution model 1, the relative deviations were determined by Equation (25), where the index i denotes the order of the data in the respective results table.

$$\delta_{mesh}(\%) = \frac{w_i - w_{i-1}}{w_{i-1}} \cdot 100(\%), \; i \geq 2 \tag{25}$$

- Porosity Distribution Model 1 (M1):

We developed convergence studies in order to evidence the reason for the discretization selection. To illustrate them, we present the results obtained for two sets of distinct parameterizations of maximum porosities and power law exponent values, considering Q4 finite elements and FSDT. The results achieved and presented in Table 5 show that the mesh refinement from 10×10 elements presents a deviation of less than 0.2%. Based on this evidence, the following studies were performed considering a mesh of 10×10 elements.

Table 5. Porosity distribution model M1: convergence study.

ϕ	p	Mesh	$w(\frac{a}{2},\frac{b}{2},0)$ (m)	δ_{mesh} (%)
0.1	1	4×4	-1.3855×10^{-4}	-
		6×6	-1.4035×10^{-4}	1.30
		8×8	-1.4091×10^{-4}	0.39
		10×10	-1.4116×10^{-4}	0.18
		12×12	-1.4129×10^{-4}	0.10
		14×14	-1.4137×10^{-4}	0.06
		16×16	-1.4142×10^{-4}	0.04
		18×18	-1.4146×10^{-4}	0.03
		20×20	-1.4149×10^{-4}	0.02
0.5	5	4×4	-2.5263×10^{-4}	-
		6×6	-2.5597×10^{-4}	1.32
		8×8	-2.5701×10^{-4}	0.40
		10×10	-2.5747×10^{-4}	0.18
		12×12	-2.5773×10^{-4}	0.10
		14×14	-2.5788×10^{-4}	0.06
		16×16	-2.5798×10^{-4}	0.04
		18×18	-2.5804×10^{-4}	0.03
		20×20	-2.5809×10^{-4}	0.02

The results obtained regarding transverse displacement at the plate's center are presented in Table 6. In this study, the displacement increased with increasing maximum porosity for all power law exponents considered, as expected.

Table 6. Porosity distribution model M1: plates center transverse displacement for different finite models and shear correction factor approaches.

ϕ	p	Q4		Q9	
		k^{calc}	$k = 5/6$	k^{calc}	$k = 5/6$
		$w(\frac{a}{2},\frac{b}{2},0)$ (m)	δ_{Q4} (%)	$w(\frac{a}{2},\frac{b}{2},0)$ (m)	δ_{Q9} (%)
0	**0**	-7.9330×10^{-5}	0.00	-7.9625×10^{-5}	0.00
	1	-1.3168×10^{-4}	−5.14	-1.3215×10^{-4}	−4.96
	2	-1.5267×10^{-4}	−7.17	-1.5321×10^{-4}	−6.94
	5	-1.7054×10^{-4}	−5.51	-1.7114×10^{-4}	−5.33
	10	-1.8510×10^{-4}	−2.95	-1.8574×10^{-4}	−2.85
0.3	0	-9.9540×10^{-5}	−0.94	-9.9930×10^{-5}	−0.93
	1	-1.6493×10^{-4}	−1.81	-1.6556×10^{-4}	−1.70
	2	-1.9003×10^{-4}	−3.06	-1.9075×10^{-4}	−2.91
	5	-2.1256×10^{-4}	−1.83	-2.1335×10^{-4}	−1.73
	10	-2.3281×10^{-4}	−0.50	-2.3367×10^{-4}	−0.46
0.6	0	-1.3788×10^{-4}	−5.65	-1.3845×10^{-4}	−5.55
	1	-2.2603×10^{-4}	0.13	-2.2695×10^{-4}	0.14
	2	-2.5832×10^{-4}	0.03	-2.5936×10^{-4}	0.07
	5	-2.9115×10^{-4}	−0.07	-2.9231×10^{-4}	−0.06
	10	-3.2350×10^{-4}	−0.91	-3.2479×10^{-4}	−0.91

Comparing the results with 4-node elements and different shear correction factor approaches, the relative deviation increased from $p = 0$ to $p = 2$, decreasing with increasing power law exponents. Moreover, the increase in maximum porosity value resulted in a relative deviation increase for $p = 0$—the opposite behavior to that verified for the intermediate power law exponents. When considering p = 10, the relative deviations showed an oscillating behavior with increasing maximum porosity value. However, for maximum porosity values of 0.5 and 0.6 and intermediate power law exponents these deviations were nearly zero, except for the case of null power law exponent. The same behavior was verified when doing the same comparative study with 9-node elements, except for the specific case considering a maximum porosity value of 0.6.

Additionally, we verified that when considering the common value of 5/6 for the shear correction factor, the relative deviation between the results observed for Q4 and Q9 elements was very low, presenting a decreasing behavior with increasing maximum porosity value, except for p = 0, where the opposite was verified. With the other approach, this relative deviation also presented very low values, although the increase of maximum porosity value resulted in higher deviations for all power law exponents considered.

Figure 13 shows the plate's center displacement for different power law exponents and maximum porosity values, obtained considering Q4 finite elements. In the figure, it is clear that higher maximum porosity values corresponded to higher maximum transverse displacement magnitudes for all exponents, with the effect being more pronounced when considering larger exponents.

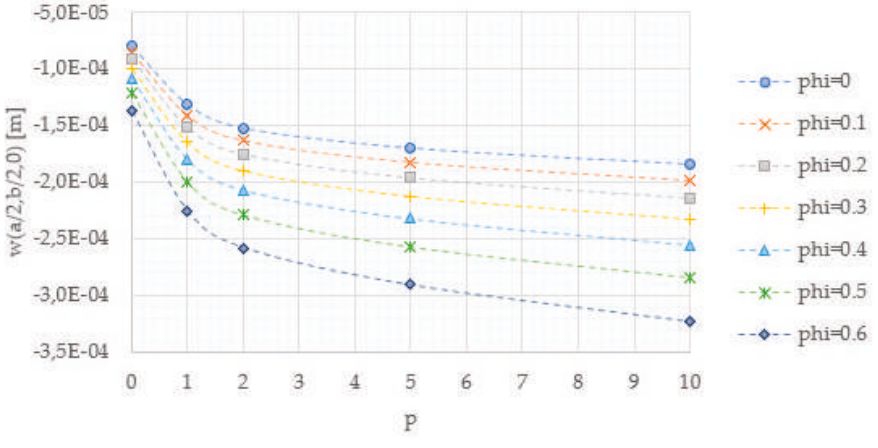

Figure 13. Porosity distribution model M1: evolution of plate's center transverse displacement.

In order to compare the results obtained by applying different shear deformation theories, keeping the configurations considered above, the plate's center displacement was determined by applying the third-order shear deformation theory (HSDT) proposed by [49], and also implemented by the authors for this purpose. The results obtained are presented in Table 7, with the relative deviations determined by:

$$\delta_{HSDT}(\%) = \frac{w_{HSDT} - w_{FSDT}}{w_{FSDT}} \cdot 100(\%). \tag{26}$$

When considering a homogeneous isotropic material ($p = 0$), the deviation between the results obtained was very small for low maximum porosity values, increasing with the increase in porosity. Fixing the power law exponent, the increase of maximum porosities values led to a decrease in the relative deviations, except for the exponent $p = 10$ where the transition between $\phi = 0.4$ and $\phi = 0.5$ led to an increase in the relative deviation. For all the maximum porosity values presented, there were slighter relative deviations in cases where the evolution of the material's constitution through the

thickness was smoother (i.e., for lower and higher power law exponents), except for the case where $\phi = 0.6$, for which the highest power law exponent presented a relative deviation higher than the other non-nulls.

Table 7. Porosity distribution model M1: plate's center transverse displacement for different shear deformation theories.

ϕ	p	$w_{FSDT}(\frac{a}{2},\frac{b}{2},0)$ (m)	$w_{HSDT}(\frac{a}{2},\frac{b}{2},0)$ (m)	δ_{HSDT} (%)
0	0	-7.9330×10^{-5}	-7.9359×10^{-5}	0.04
	1	-1.3168×10^{-4}	-1.2363×10^{-4}	−6.11
	2	-1.5267×10^{-4}	-1.3980×10^{-4}	−8.43
	5	-1.7054×10^{-4}	-1.5964×10^{-4}	−6.39
	10	-1.8510×10^{-4}	-1.7875×10^{-4}	−3.43
0.1	0	-8.5029×10^{-5}	-8.4957×10^{-5}	−0.08
	1	-1.4116×10^{-4}	-1.3402×10^{-4}	−5.05
	2	-1.6335×10^{-4}	-1.5175×10^{-4}	−7.10
	5	-1.8250×10^{-4}	-1.7308×10^{-4}	−5.16
	10	-1.9861×10^{-4}	-1.9351×10^{-4}	−2.57
0.2	0	-9.1656×10^{-5}	-9.1228×10^{-5}	−0.47
	1	-1.5208×10^{-4}	-1.4588×10^{-4}	−4.08
	2	-1.7562×10^{-4}	-1.6538×10^{-4}	−5.83
	5	-1.9628×10^{-4}	-1.8833×10^{-4}	−4.05
	10	-2.1425×10^{-4}	-2.1017×10^{-4}	−1.91
0.3	0	-9.9540×10^{-5}	-9.8380×10^{-5}	−1.17
	1	-1.6493×10^{-4}	-1.5965×10^{-4}	−3.20
	2	-1.9003×10^{-4}	-1.8120×10^{-4}	−4.64
	5	-2.1256×10^{-4}	-2.0596×10^{-4}	−3.10
	10	-2.3281×10^{-4}	-2.2936×10^{-4}	−1.48
0.4	0	-1.0919×10^{-4}	-1.0672×10^{-4}	−2.27
	1	-1.8050×10^{-4}	-1.7601×10^{-4}	−2.49
	2	-2.0744×10^{-4}	-2.0002×10^{-4}	−3.58
	5	-2.3237×10^{-4}	-2.2687×10^{-4}	−2.36
	10	-2.5551×10^{-4}	-2.5202×10^{-4}	−1.37
0.5	0	-1.2147×10^{-4}	-1.1671×10^{-4}	−3.92
	1	-2.0008×10^{-4}	-1.9602×10^{-4}	−2.03
	2	-2.2932×10^{-4}	-2.2304×10^{-4}	−2.74
	5	-2.5747×10^{-4}	-2.5241×10^{-4}	−1.97
	10	-2.8446×10^{-4}	-2.7959×10^{-4}	−1.71
0.6	0	-1.3788×10^{-4}	-1.2913×10^{-4}	−6.35
	1	-2.2603×10^{-4}	-2.2146×10^{-4}	−2.02
	2	-2.5832×10^{-4}	-2.5238×10^{-4}	−2.30
	5	-2.9115×10^{-4}	-2.8491×10^{-4}	−2.14
	10	-3.2350×10^{-4}	-3.1455×10^{-4}	−2.77

- Porosity Distribution Models M2 and M3:

The results presented in Tables 8 and 9 were obtained considering porosity distribution models M2 and M3, for Q4 and Q9 finite element discretizations and different shear correction factor approaches, respectively.

Table 8. Porosity distribution model M2: plate's center transverse displacement for different finite elements and shear correction factor approaches.

p	Q4		Q9	
	k^{calc}	$k = 5/6$	k^{calc}	$k = 5/6$
	$w(\frac{a}{2},\frac{b}{2},0)$ **(m)**	δ_{Q4} **(%)**	$w(\frac{a}{2},\frac{b}{2},0)$ **(m)**	δ_{Q9} **(%)**
0	-1.6403×10^{-4}	0.00	-1.6472×10^{-4}	0.00
1	-2.7631×10^{-4}	−5.20	-2.7747×10^{-4}	−5.01
2	-3.2144×10^{-4}	−7.21	-3.2278×10^{-4}	−6.95
3	-3.4037×10^{-4}	−7.01	-3.4178×10^{-4}	−6.76
4	-3.5137×10^{-4}	−6.28	-3.5282×10^{-4}	−6.05
5	-3.5972×10^{-4}	−5.50	-3.6120×10^{-4}	−5.31
6	-3.6697×10^{-4}	−4.81	-3.6848×10^{-4}	−4.64
7	-3.7359×10^{-4}	−4.22	-3.7512×10^{-4}	−4.06
8	-3.7975×10^{-4}	−3.72	-3.8131×10^{-4}	−3.58
9	-3.8552×10^{-4}	−3.29	-3.8710×10^{-4}	−3.17
10	-3.9093×10^{-4}	−2.94	-3.9254×10^{-4}	−2.83

Table 9. Porosity distribution model M3: plate's center transverse displacement for different finite elements and shear correction factor approaches.

p	Q4		Q9	
	k^{calc}	$k = 5/6$	k^{calc}	$k = 5/6$
	$w(\frac{a}{2},\frac{b}{2},0)$ **(m)**	δ_{Q4} **(%)**	$w(\frac{a}{2},\frac{b}{2},0)$ **(m)**	δ_{Q9} **(%)**
0	-1.1377×10^{-4}	−0.10	-1.1422×10^{-4}	−0.10
1	-1.8911×10^{-4}	−4.98	-1.8984×10^{-4}	−4.80
2	-2.2387×10^{-4}	−7.09	-2.2473×10^{-4}	−6.85
3	-2.3900×10^{-4}	−6.79	-2.3991×10^{-4}	−6.56
4	-2.4781×10^{-4}	−5.91	-2.4875×10^{-4}	−5.71
5	-2.5454×10^{-4}	−5.01	-2.5551×10^{-4}	−4.84
6	-2.6041×10^{-4}	−4.24	-2.6140×10^{-4}	−4.09
7	-2.6576×10^{-4}	−3.59	-2.6677×10^{-4}	−3.46
8	-2.7070×10^{-4}	−3.07	-2.7173×10^{-4}	−2.96
9	-2.7529×10^{-4}	−2.64	-2.7633×10^{-4}	−2.54
10	-2.7953×10^{-4}	−2.29	-2.8059×10^{-4}	−2.21

In general, both porosity distribution models led to the same verifications about relative deviations. Like in the previous study, the relative deviations δ_{Q4} and δ_{Q9} increased for increasing power law exponents between $p = 0$ and $p = 2$, after which these deviations presented a decreasing behavior. Additionally, comparing Q4 and Q9 results denoted by k^{cal} we verified that the relative deviation was maximal when $p = 0$, and presented a decreasing behavior with increasing power law exponent. When $k = 5/6$, the relative deviation of Q4 and Q9 to Q4 with k^{calc} also increased from $p = 0$ to $p = 2$, then decreased with increasing power law exponent in both comparative analyses.

Figure 14 depicts the behavior of the plate's center transverse displacement, using Q4 finite elements, for the power law exponents considered, evidencing the fact that porosity distribution model M3 provided smaller displacements than model M2, and the increase in the exponent of the power law induced a greater difference between the results obtained with each model.

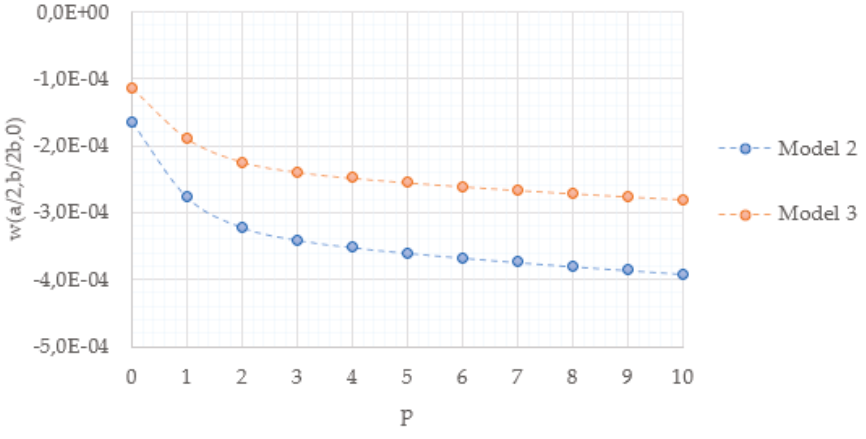

Figure 14. Evolution of the plate's center transverse displacement with the power law exponent.

Similar to the M1 porosity distribution model, the plate's center displacements for models M2 and M3 were also obtained, considering the same third-order shear deformation theory. The results obtained for both porosity distribution models with the different shear deformation theories are shown in Table 10, where the relative deviations presented were determined by Equation (26). The results show a behavior similar to the one observed and described for model M1 about the effect of the power law exponent on the relative deviation.

Table 10. Porosity distribution models M2 and M3: plate's center transverse displacement for different shear deformation theories.

p	M2			M3		
	$w_{FSDT}(\frac{a}{2},\frac{b}{2},0)$ (m)	$w_{HSDT}(\frac{a}{2},\frac{b}{2},0)$ (m)	δ_{HSDT} (%)	$w_{HSDT}(\frac{a}{2},\frac{b}{2},0)$ (m)	$w_{HSDT}(\frac{a}{2},\frac{b}{2},0)$ (m)	δ_{HSDT} (%)
0	-1.6403×10^{-4}	-1.6407×10^{-4}	0.03	-1.1377×10^{-4}	-1.1308×10^{-4}	−0.60
1	-2.7631×10^{-4}	-2.6157×10^{-4}	−5.34	-1.8911×10^{-4}	-1.7729×10^{-4}	−6.25
2	-3.2144×10^{-4}	-2.9782×10^{-4}	−7.35	-2.2387×10^{-4}	-2.0457×10^{-4}	−8.62
3	-3.4037×10^{-4}	-3.1621×10^{-4}	−7.10	-2.3900×10^{-4}	-2.1909×10^{-4}	−8.33
4	-3.5137×10^{-4}	-3.2917×10^{-4}	−6.32	-2.4781×10^{-4}	-2.2945×10^{-4}	−7.41
5	-3.5972×10^{-4}	-3.3992×10^{-4}	−5.50	-2.5454×10^{-4}	-2.3807×10^{-4}	−6.47
6	-3.6697×10^{-4}	-3.4941×10^{-4}	−4.79	-2.6041×10^{-4}	-2.4565×10^{-4}	−5.67
7	-3.7359×10^{-4}	-3.5798×10^{-4}	−4.18	-2.6576×10^{-4}	-2.5247×10^{-4}	−5.00
8	-3.7975×10^{-4}	-3.6582×10^{-4}	−3.67	-2.7070×10^{-4}	-2.5862×10^{-4}	−4.46
9	-3.8552×10^{-4}	-3.7302×10^{-4}	−3.24	-2.7529×10^{-4}	-2.6421×10^{-4}	−4.02
10	-3.9093×10^{-4}	-3.7967×10^{-4}	−2.88	-2.7953×10^{-4}	-2.6928×10^{-4}	−3.67

In the present work, the three porosity distributions analyzed showed some similarities regarding the estimation of effective material properties. Noting that for the materials considered, the product $e_0\beta$ assumed an approximate value of 0.49, we can then compare this case for models 2 and 3 (M2 and M3) to the case where in model 1 (M1) the maximum porosity value took the value 0.5. In this sense, Table 11 presents the results obtained under these conditions, considering a Q4 plate model and a shear correction factor determined with Equation (20), with respect to neutral surface shift, shear correction factor, and plate's center displacement.

Table 11. Results obtained with the three porosity distribution models considered.

p	Model 1 ($\phi = 0.5$)			Model 2			Model 3		
	d/h	k	$w(\frac{a}{2},\frac{b}{2},0)$ (m)	d/h	k	$w(\frac{a}{2},\frac{b}{2},0)$ (m)	d/h	k	$w(\frac{a}{2},\frac{b}{2},0)$ (m)
0	−0.0638	0.8217	-1.215×10^{-4}	0	5/6	-1.640×10^{-4}	2.6×10^{-25}	0.7632	-1.138×10^{-4}
1	0.0308	0.8390	-2.001×10^{-4}	0.0889	0.8291	-2.763×10^{-4}	0.0845	0.7590	-1.891×10^{-4}
2	0.0470	0.7988	-2.293×10^{-4}	0.1081	0.7853	-3.214×10^{-4}	0.1033	0.7199	-2.239×10^{-4}
5	0.0295	0.7477	-2.575×10^{-4}	0.0985	0.7371	-3.597×10^{-4}	0.0899	0.6791	-2.545×10^{-4}
10	0.0003	0.7546	-2.845×10^{-4}	0.0717	0.7519	-3.909×10^{-4}	0.0604	0.7074	-2.795×10^{-4}

These results indicate that porosity distribution M2 promoted greater displacement of the plate's center, whereas model M3 led to smaller displacements. Regarding the neutral surface shift, in the case of model M1, it started to assume a negative value when $p = 0$ (the highest shift for the exponents evaluated). Then, the neutral surface approached the medium surface and moved away, presenting this behavior from $p = 0$ to $p = 2$, after which the neutral surface shift assumed smaller and smaller values in the sense of a new approximation between the neutral and medium surfaces as the exponent of the power law increased. In models M2 and M3 the neutral surface shift presented a monotonic increasing behavior from $p = 0$ to $p = 2$, starting with coincident neutral and medium surfaces when $p = 0$, then decreasing with increasing power law exponents, presenting higher neutral surface shifts than those verified with model 3.

Regarding the shear correction factor, there was an oscillating behavior observed in model M1, with an increasing trend between $p = 0$ and $p = 1$, a decreasing one between $p = 2$ and $p = 5$, and finishing with an increasing trend again from $p = 5$ to $p = 10$. In models M2 and M3, this factor presented a decreasing behavior with increasing power law exponents until $p = 5$, and then increases from $p = 5$ to $p = 10$. It is important to note that in the results presented in Table 11 the null power law exponent corresponds to a material constituted only by titanium oxide, but with the presence of a porosity distribution.

In the particular case of model M3 considering $p = 0$, the neutral surface presented a shift from the medium surface that can numerically be considered as zero. However, it is important to highlight that this result does not lead to the expected shear correction factor value of 5/6, as verified with model M2. For this reason, the authors decided to maintain the value of 2.6×10^{-25} for the respective normalized neutral surface shift, d/h.

4. Discussion and Conclusions

The analyses carried out on the various case studies led to the following conclusions:

- In all porosity distributions models studied, the neutral surface shift increased for power law exponents between 0 and 2, and for larger exponents it showed a decreasing behavior.
- The studies of the influence of porosity distribution model M1 on the shear correction factor showed that for a certain power law exponent the shear correction factor increased with increasing maximum porosity values, except for the case in which $p = 0$ which corresponds to a plate constituted only by TiO_2. The increasing behavior was more pronounced when the power law exponent took the value 2, and was less pronounced for the higher power law exponents considered.
- Concerning the influence of the porosity distribution models on the deviation from the neutral surface, models M2 and M3 resulted in behaviors similar to each other and similar to those verified in the corresponding analysis carried out on model M1, with model M2 leading to lower neutral surface shifts. The difference between the models increased with increasing power law exponents.
- With respect to the shear correction factor, porosity distribution models M2 and M3 showed a similar behavior, with M3 presenting lower values (i.e., leading to higher corrections of the transverse shear stiffness coefficients). In this case, the difference between both models decreased with increasing power law exponents.

- Regarding the maximum transverse displacement, and in correspondence to the expected trend, all case studies showed an increasing behavior with the increase in maximum porosity values and power law exponents. In the case of model M1, for a certain power law exponent the increase in the plate's center displacement became more pronounced as the maximum porosity value increased. The increase in the magnitude of the maximum transverse displacement with the increase of power law exponent is explained by the fact that higher exponents correspond to a smaller volume fraction of the stiffer phase, TiO_2.
- The last study carried out to promote a comparison between the three porosity distributions demonstrated that model M2 led to higher displacements of the plate's center, while model M3 led to lower ones. Except for the case of null power law exponent, in which model M2 presented the higher shear correction factor and model M3 the lower one, in the remaining power law exponents considered model M1 and model M3 presented the higher and the lower shear correction factors, respectively. Moreover, the shear correction factor presented a similar behavior with the increase of power law exponent in both models M2 and M3, decreasing from $p = 0$ to $p = 5$, and increasing in the last transition between $p = 5$ and $p = 10$. The first model had a different behavior concerning the shear correction factor and power law exponent relation, first presenting an increase in the transition between $p = 0$ and $p = 1$, decreasing for the intermediate exponents, and increasing in the transition between the two largest exponents presented.
- The results regarding the maximum absolute plate displacement obtained with the plate elements Q4 and Q9 were quite close to each other in most of the studied configurations. Therefore, depending on the application, in order to obtain a shorter computing time the Q4 model may be a good choice, resulting in an accuracy similar to the one obtained with the Q9 model.
- When comparing the relative deviations between the results obtained with the present FSDT and HSDT, model M1 showed an increasing relative deviation with increasing maximum porosity values when considering a null power law exponent. For all three porosity distribution models, the lower relative deviations obtained, corresponded to the lower and to the highest power law exponents (i.e., to smoother material evolutions through the thickness).
- In the future, it is important to give continuity to the development of theoretical models to describe the real porosity distributions and how they influence the resulting material properties and, consequently, the constitutive relations. Obtaining more accurate predictions of porous functionally graded material properties and/or designed ones, will continue to be an important research topic in order to allow for higher-quality predictions of structures' behavior.
- Another important aspect and a limitation of the present work is related to the behavior prediction of thicker plate structures with different porosity models, wherein higher-order models are expected to behave better. However, it will be important to compare the response achieved via higher-order models with the present results under comparable situations.

Author Contributions: A.F.M.: Data curation, Conceptualization, Methodology, Software, Verification, Writing—original draft, Writing—review and editing. M.A.R.L.: Conceptualization, Methodology, Formal analysis, Supervision, Project administration. J.I.B.: Methodology, Writing—review and editing. J.A.R.: Data curation, Writing—review and editing. All authors have read and agreed to the published version of the manuscript.

Funding: This research was funded by Project IDMEC, LAETA UIDB/50022/2020, and Project IPL/2019/MOCHVar/ISEL.

Acknowledgments: The authors wish to acknowledge the support given by FCT/MEC through Project IDMEC, LAETA UIDB/50022/2020. The authors also acknowledge the support of Project IPL/2019/MOCHVar/ISEL.

Conflicts of Interest: The authors declare no conflicts of interest.

References

1. Naebe, M.; Shirvanimoghaddam, K. Functionally graded materials: A review of fabrication and properties. *Appl. Mater. Today* **2016**, *5*, 223–245. [CrossRef]

2. Sola, A.; Bellucci, D.; Cannillo, V. Functionally graded materials for orthopedic applications—An update on design and manufacturing. *Biotechnol. Adv.* **2016**, *34*, 504–531. [CrossRef] [PubMed]
3. Miao, X.; Sun, D. Graded/Gradient Porous Biomaterials. *Materials* **2009**, *3*, 26–47. [CrossRef]
4. Kiran, S.C.; Kattimani, M.C. Assessment of porosity influence on vibration and static behavior of functionally graded magneto-electro-elastic plate: A finite element study. *Eur. J. Mech. A Solids* **2018**, *71*, 258–277. [CrossRef]
5. Zhang, Z.; Li, Y.; Wu, H.; Zhang, H.; Wu, H.; Jiang, S.; Chai, G. Mechanical analysis of functionally graded graphene oxide-reinforced composite beams based on the first-order shear deformation theory. *Mech. Adv. Mater. Struct.* **2018**, *27*, 3–11. [CrossRef]
6. Hosseini-Hashemi, S.; Taher, H.R.D.; Akhavan, H.; Omidi, M. Free vibration of functionally graded rectangular plates using first-order shear deformation plate theory. *Appl. Math. Model.* **2010**, *34*, 1276–1291. [CrossRef]
7. Thai, H.-T.; Choi, D.-H. A simple first-order shear deformation theory for the bending and free vibration analysis of functionally graded plates. *Compos. Struct.* **2013**, *101*, 332–340. [CrossRef]
8. Sayyad, A.; Ghugal, Y. Modeling and analysis of functionally graded sandwich beams: A review. *Mech. Adv. Mater. Struct.* **2018**, *26*, 1776–1795. [CrossRef]
9. Keddouri, A.; Hadji, L.; Tounsi, A. Static analysis of functionally graded sandwich plates with porosities. *Adv. Mater. Res. South Korea* **2019**, *8*, 155–177.
10. Li, Z.; Zheng, J.; Chen, Y.; Zhang, Z. Collapse mechanism of the thin-walled functionally graded cylinders encased in the saturated permeable mediums. *Eng. Struct.* **2019**, *198*. [CrossRef]
11. Li, Z.; Tang, F.; Chen, Y.; Zheng, J. Material distribution optimization of functionally graded arch subjected to external pressure under temperature rise field. *Thin-Walled Struct.* **2019**, *138*, 64–78. [CrossRef]
12. Li, Z.; Zheng, J.; Chen, Y. Nonlinear buckling of thin-walled FGM arch encased in rigid confinement subjected to external pressure. *Eng. Struct.* **2019**, *186*, 86–95. [CrossRef]
13. Li, Z.; Zheng, J.; Zhang, Z.; He, H. Nonlinear stability and buckling analysis of composite functionally graded arches subjected to external pressure and temperature loading. *Eng. Struct.* **2019**, *199*, 109606. [CrossRef]
14. Li, Z.; Zheng, J.; Sun, Q.; He, H. Nonlinear structural stability performance of pressurized thin-walled FGM arches under temperature variation field. *Int. J. Non-linear Mech.* **2019**, *113*, 86–102. [CrossRef]
15. Zhang, Y.; Wang, J. Fabrication of Functionally Graded Porous Polymer Structures using Thermal Bonding Lamination Techniques. *Procedia Manuf.* **2017**, *10*, 866–875. [CrossRef]
16. Heshmati, M.; Daneshmand, F. A study on the vibrational properties of weight-efficient plates made of material with functionally graded porosity. *Compos. Struct.* **2018**, *200*, 229–238. [CrossRef]
17. Nguyen, L.B.; Thai, C.H.; Zenkour, A.M.; Nguyen-Xuan, H. An isogeometric Bézier finite element method for vibration analysis of functionally graded piezoelectric material porous plates. *Int. J. Mech. Sci.* **2019**, *158*, 165–183. [CrossRef]
18. Gao, K.; Li, R.; Yang, J. Dynamic characteristics of functionally graded porous beams with interval material properties. *Eng. Struct.* **2019**, *197*, 109441. [CrossRef]
19. Fahsi, B.; Bouiadjra, R.B.; Mahmoudi, A.; Benyoucef, S.; Tounsi, A. Assessing the Effects of Porosity on the Bending, Buckling, and Vibrations of Functionally Graded Beams Resting on an Elastic Foundation by Using a New Refined Quasi-3D Theory. *Mech. Compos. Mater.* **2019**, *55*, 219–230. [CrossRef]
20. Zhao, J.; Wang, Q.; Deng, X.; Choe, K.; Zhong, R.; Shuai, C. Free vibrations of functionally graded porous rectangular plate with uniform elastic boundary conditions. *Compos. Part B Eng.* **2019**, *168*, 106–120. [CrossRef]
21. Merdaci, S.; Belghoul, H. High-order shear theory for static analysis of functionally graded plates with porosities. *Comptes Rendus Mécanique* **2019**, *347*, 207–217. [CrossRef]
22. Li, Z.; Zheng, J. Analytical consideration and numerical verification of the confined functionally graded porous ring with graphene platelet reinforcement. *Int. J. Mech. Sci.* **2019**, *162*. [CrossRef]
23. Li, Z.; Zheng, J.; Chen, Y.; Sun, Q.; Zhang, Z. Effect of temperature variations on the stability mechanism of the confined functionally graded porous arch with nanocomposites reinforcement under mechanical loading. *Compos. Part B Eng.* **2019**, *176*. [CrossRef]
24. Li, Z.; Zheng, J.; Zhang, Z. Mechanics of the confined functionally graded porous arch reinforced by graphene platelets. *Eng. Struct.* **2019**, *201*, 109817. [CrossRef]

25. Li, Z.; Zheng, J. Nonlinear stability of the encased functionally graded porous cylinders reinforced by graphene nanofillers subjected to pressure loading under thermal effect. *Compos. Struct.* **2020**, *233*, 111584. [CrossRef]
26. Li, Z. Exploration of the encased nanocomposites functionally graded porous arches: Nonlinear analysis and stability behavior. *Appl. Math. Model.* **2020**, *82*, 1–16. [CrossRef]
27. Li, Z.; Zheng, J. Structural failure performance of the encased functionally graded porous cylinder consolidated by graphene platelet under uniform radial loading. *Thin-Walled Struct.* **2020**, *146*, 106454. [CrossRef]
28. Masjedi, P.K.; Maheri, A.; Weaver, P.M. Large deflection of functionally graded porous beams based on a geometrically exact theory with a fully intrinsic formulation. *Appl. Math. Model.* **2019**, *76*, 938–957. [CrossRef]
29. Kovacik, J. Correlation between Elastic Modulus, Shear Modulus, Poisson's Ratio and Porosity in Porous Materials. *Adv. Eng. Mater.* **2008**, *10*, 250–252. [CrossRef]
30. Han, C.; Li, Y.; Wang, Q.; Wen, S.; Wei, Q.; Yan, C.; Hao, L.; Liu, J.; Shi, Y. Continuous functionally graded porous titanium scaffolds manufactured by selective laser melting for bone implants. *J. Mech. Behav. Biomed. Mater.* **2018**, *80*, 119–127. [CrossRef]
31. Sopyan, I.; Mel, M.; Ramesh, S.; Khalid, K. Porous hydroxyapatite for artificial bone applications. *Sci. Technol. Adv. Mater.* **2007**, *8*, 116–123. [CrossRef]
32. Yılmaz, E.; Gökçe, A.; Findik, F.; Gülsoy, H.; Özkan; Iyibilgin, O. Mechanical properties and electrochemical behavior of porous Ti-Nb biomaterials. *J. Mech. Behav. Biomed. Mater.* **2018**, *87*, 59–67. [CrossRef] [PubMed]
33. Wang, I.-F.; Ditter, J.F.; Morris, R. Microfiltration membranes having high pore density and mixed isotropic and anisotropic structure. U.S. Patent EP0846024B1, 22 August 2001.
34. Lu, W.; Yuan, Z.; Zhao, Y.; Zhang, H.; Zhang, H.; Li, X. Porous membranes in secondary battery technologies. *Chem. Soc. Rev.* **2017**, *46*, 2199–2236. [CrossRef]
35. Meulenberg, W.A.; Schulze-Küppers, F.; Deibert, W.; van Gestel, T.; Baumann, S. Ceramic Membranes: Materials–Components–Potential Applications. *ChemBioEng Rev.* **2019**, *6*, 198–208. [CrossRef]
36. Yu, L.; Kanezashi, M.; Nagasawa, H.; Tsuru, T. Phase inversion/sintering-induced porous ceramic microsheet membranes for high-quality separation of oily wastewater. *J. Membr. Sci.* **2020**, *595*, 117477. [CrossRef]
37. Zhang, G.; Jin, W.; Xu, N. Design and Fabrication of Ceramic Catalytic Membrane Reactors for Green Chemical Engineering Applications. *Engineering* **2018**, *4*, 848–860. [CrossRef]
38. Carranza, J.C.; Pérez, L.; Ganesan, R.; Casas, B.Y.; Drew, R.A.L.; Ruiz-Aguilar, C.; Figueroa, I.A.; Alfonso, I. Effect of fractal distribution of the porosity on mechanical properties of Al foams manufactured by infiltration. *J. Braz. Soc. Mech. Sci. Eng.* **2019**, *41*, 379. [CrossRef]
39. Costantini, M.; Jaroszewicz, J.; Kozon, L.; Szlazak, K.; Swieszkowski, W.; Garstecki, P.; Stubenrauch, C.; Barbetta, A.; Guzowski, J. 3D-Printing of Functionally Graded Porous Materials Using On-Demand Reconfigurable Microfluidics. *Angewandte Chemie* **2019**, *131*, 7702–7707. [CrossRef]
40. Legrand, A.; Craig, G.A.; Bonneau, M.; Minami, S.; Urayama, K.; Furukawa, S. Understanding the multiscale self-assembly of metal-organic polyhedra towards functionally graded porous gels. *Chem. Sci.* **2019**, *10*, 10833–10842. [CrossRef]
41. Nguyen, N.V.; Nguyen, H.X.; Lee, S.; Nguyen-Xuan, H. Geometrically nonlinear polygonal finite element analysis of functionally graded porous plates. *Adv. Eng. Softw.* **2018**, *126*, 110–126. [CrossRef]
42. Bernardo, G.; Damásio, F.; Silva, T.; Loja, A. A study on the structural behaviour of FGM plates static and free vibrations analyses. *Compos. Struct.* **2016**, *136*, 124–138. [CrossRef]
43. Nguyen, T.-K.; Sab, K.; Bonnet, G. First-order shear deformation plate models for functionally graded materials. *Compos. Struct.* **2008**, *83*, 25–36. [CrossRef]
44. Mota, A.F.; Loja, A. Mechanical Behavior of Porous Functionally Graded Nanocomposite Materials. *C J. Carbon Res.* **2019**, *5*, 34. [CrossRef]
45. Kim, J.; Żur, K.K.; Reddy, J. Bending, free vibration, and buckling of modified couples stress-based functionally graded porous micro-plates. *Compos. Struct.* **2019**, *209*, 879–888. [CrossRef]
46. Coskun, S.; Kim, J.; Toutanji, H. Bending, Free Vibration, and Buckling Analysis of Functionally Graded Porous Micro-Plates Using a General Third-Order Plate Theory. *J. Compos. Sci.* **2019**, *3*, 15. [CrossRef]
47. Du, Y.; Wang, S.; Sun, L.; Shan, Y. Free Vibration of Rectangular Plates with Porosity Distributions under Complex Boundary Constraints. *Shock. Vib.* **2019**, *2019*, 1–16. [CrossRef]
48. Reddy, J.N. *Mechanics of Laminated Composite Plates and Shells*; Informa UK Limited: Colchester, UK, 2004.

49. Kant, T.; Swaminathan, K. Analytical solutions for free vibration of laminated composite and sandwich plates based on a higher-order refined theory. *Compos. Struct.* **2001**, *53*, 73–85. [CrossRef]
50. Zienkiewicz, O.C.; Taylor, R.L. *The Finite Element Method*, 5th ed.; Butterworth-Heinemann: Oxford, UK, 2000; Volume 1.
51. Nguyen, T.-K.; Sab, K.; Bonnet, G. Shear Correction Factors for Functionally Graded Plates. *Mech. Adv. Mater. Struct.* **2007**, *14*, 567–575. [CrossRef]
52. Lu, H.; Yao, Y.; Yin, J.; Lin, L. Functionally graded carbon nanotube and nafion/silica nanofibre for electrical actuation of carbon fibre reinforced shape memory polymer. *Pigment. Resin Technol.* **2016**, *45*, 93–98. [CrossRef]
53. Li, H.; Liu, N.; Pang, F.; Du, Y.; Li, S. An Accurate Solution Method for the Static and Vibration Analysis of Functionally Graded Reissner–Mindlin Rectangular Plate with General Boundary Conditions. *Shock. Vib.* **2018**, *2018*, 1–21. [CrossRef]
54. Singha, M.; Prakash, T.; Ganapathi, M. Finite element analysis of functionally graded plates under transverse load. *Finite Elements Anal. Des.* **2011**, *47*, 453–460. [CrossRef]

Mathematical and Computational Applications

MDPI

Article

A Continuation Procedure for the Quasi-Static Analysis of Materially and Geometrically Nonlinear Structural Problems

Davide Bellora and Riccardo Vescovini *

Dipartimento di Scienze e Tecnologie Aerospaziali, Politecnico di Milano, Via La Masa 34, 20156 Milano, Italy; davide.bellora@mail.polimi.it

* Correspondence: riccardo.vescovini@polimi.it; Tel.: +39-02-2399-8332

Received: 14 October 2019; Accepted: 30 October 2019; Published: 2 November 2019

Abstract: Discussed is the implementation of a continuation technique for the analysis of nonlinear structural problems, which is capable of accounting for geometric and dissipative requirements. The strategy can be applied for solving quasi-static problems, where nonlinearities can be due to geometric or material response. The main advantage of the proposed approach relies in its robustness, which can be exploited for tracing the equilibrium paths for problems characterized by complex responses involving the onset and propagation of cracks. A set of examples is presented and discussed. For problems involving combined material and geometric nonlinearties, the results illustrate the advantages of the proposed hybrid continuation technique in terms of efficiency and robustness. Specifically, less iterations are usually required with respect to similar procedures based on purely geometric constraints. Furthermore, bifurcation plots can be easily traced, furnishing the analyst a powerful tool for investigating the nonlinear response of the structure at hand.

Keywords: continuation methods; bifurcations; limit points; cohesive elements

1. Introduction

Nonlinear analyses are commonly performed during the design phases of advanced, modern constructions. An example can be found in the design process of lightweight aerospace structures, where the capability of accurately predicting the behaviour in the post-buckling range is a task of paramount importance. The problem can often be studied by considering just nonlinearties of geometrical nature, where analytical and semi-analytical approaches can be successfully employed [1–5]. However, a proper assessment of damage tolerance demands for numerical simulations capable of predicting also the propagation of cracks, thus including nonlinear effects related to the material response. Meaningful examples illustrating the relevance of nonlinear phenomena in structural problems can be found, e.g., in the works of Refs. [6,7], while qualitative aspects on branching of cracks are reported in Ref. [8]. Due to the inherent complexity of responses involving both geometrical and material nonlinearities, the finite element approach is often the most straightforward one for performing the analysis. In this context, many numerical techniques were developed in the years for handling the peculiar aspects that characterize the response of structures in the nonlinear field. Arc-length strategies have been widely used for solving problems characterized by the presence of limit points. The presence of the load parameter as additional unknown of the problem allows the load to be increased or decreased throughout the iterative process. Pioneering work in this field is due to Riks [9] and Wemper [10]. Noteworthy are the successive efforts to develop the updated normal path method by Ramm and the spherical arc-length by Crisfield [11]. Despite the efficiency in capturing the elastic response of the structure, classical arc-length approaches can be inadequate in the presence of delamination phenomena, as the constraint equation is based on global quantities,

while the failure process tends to involve few degrees of freedom. To overcome these limitations, different strategies were proposed based on the modification of the constraint equation to consider the local nodes involved in the delamination process [12–14] or by enriching the constraint equation with information regarding the energy dissipated during the process [15–17]. An example is found in Ref. [18], where path following techniques were discussed in the framework of Embedded Finite Element Method (E-FEM).

Another class of numerical solution techniques refers to the so-called continuation approach. These path-following techniques were originally introduced by Davidenko [19,20] in the early fifties. They rely on the idea of transforming a nonlinear system of equations into a differential one. The system is parametrized with respect to a solution parameter, and is solved as an initial value problem [21–23]. The application of continuation methods to nonlinear structural analyses offers several interesting features. It allows to trace the primary equilibrium path of the structure, also in presence of snaps [24], to detect and compute the critical points [24–26] and to trace the bifurcation branches [27,28]. As a result, continuation methods enable to trace the complete bifurcation diagram of the structure, which is of particular interest for gathering deeper insight into the behavior of the structure.

While a consistent number of examples concerning the use of continuation methods for the nonlinear analysis of elastic structures are available in the literature, relatively few applications can be found for handling problems characterized by the presence of crack propagation phenomena. To the best of the authors' knowledge, no continuation methods were specifically developed for problems involving strain-softening responses.

In this article a novel continuation approach is proposed, offering the capability of handling structural responses characterized by geometrically and materially nonlinear problems. The continuation is performed referring to a modified version of the the Riks' method [24] in conjunction with a constraint regarding the dissipated energy [15,16]. The approach tries to combine the efficiency of geometric-based procedures in the elastic field, with that of the dissipative ones in the presence of damage. The resulting approach can accurately trace the equilibrium paths and shows excellent robustness on bifurcation branches dominated by dissipative phenomena.

The performance of the approach is demonstrated by means of five numerical examples. The first two ones illustrate the ability of the methods to compute the bifurcation diagram of simple elastic problems. Then, test cases characterized by mixed geometric-material nonlinearities are assessed. Finally, the application of the methods as quasi-static solution strategies is demonstrated in a challenging example dominated by material nonlinearities.

The paper is organized as follows. Introductory aspects on continuation methods are presented in Section 2, where the formulation of the nonlinear finite element approximation is briefly presented. The detection of critical points is discussed in Section 3 by introducing algorithmic aspects for classifying bifurcations and limit points, while the technique for implementing branch-switching is the subject of Section 4. Geometric and dissipative constraint equations are introduced in Section 5, and an overview of the method is provided in Section 6. The application of the method to a set of nonlinear problems is illustrated in Section 7, where test cases involving geometrically and materially nonlinear responses are presented.

2. Preliminaries

Continuation methods are a class of numerical techniques for computing the approximate solution of a system of parametrized nonlinear equations [19,20]. Denoting with $\tilde{\lambda}$ the quantity adopted for the parametrization, the procedure consists in constructing an approximation x_i of $x(\tilde{\lambda}_i)$ for a sequence of parameter values $\tilde{\lambda}_1, \ldots, \tilde{\lambda}_N$ in the interval of definition of the parameter itself.

Within the context of the finite element approach, the nonlinear equilibrium equations of a structure can be represented, in their general form, as:

$$\mathbf{f}_{\text{int}}(\mathbf{a}) - \lambda \hat{\mathbf{f}} = 0 \tag{1}$$

where $\mathbf{f}_{\text{int}}$ defines the vector of the internal forces, and $\hat{\mathbf{f}}$ provides the shape of the external forces. Nodal displacements are denoted as $\mathbf{a}$, while λ is the load parameter.

The system of Equation (1) can be seen in terms of continuation techniques after noticing that the set of equations defines implicitly a curve $\mathbf{c}$ of solution points that can be continuously parametrized by means of the parameter $\tilde{\lambda}$. Starting from an initial equilibrium solution condition defined by $[\mathbf{a}_0, \lambda_0]$—which, in turn, corresponds to an initial value $\tilde{\lambda}_0$ of the parameter $\tilde{\lambda}$—the continuation problem consists in calculating the locus of solutions given by the branch $\mathbf{c}(\tilde{\lambda})$. The process is terminated when a target point is reached.

The choice of the parametrization is a focal aspect in the development of a continuation technique. This choice is, in general, not unique and, according to its definition, different methods can be obtained. One possibility is given by the adoption of the load factor λ, leading to a force-control approach. Another choice consists in considering the displacements of a subset of nodes, which leads to a displacement-based control. These two kinds of parametrization are inadequate for handling turning points, where the surfaces $\lambda = \text{const}$ and $a_i = \text{const}$ are tangent to the equilibrium path, and no intersections can be found. On the contrary, a more suitable approach consists in adopting a parametrization that is always nearly orthogonal to the equilibrium path, so that an intersection between the surface and the path is always ensured. This is the case of a parametrization based on the arc-length of the curve s [24]. By introducing a parametrization based on s, the load factor λ becomes an additional unknown and a scalar constraint equation must be added to Equation (1). The augmented system is then obtained as:

$$\mathbf{H} = \begin{cases} \mathbf{f}_{\text{int}}(\mathbf{a}) - \lambda \hat{\mathbf{f}} = 0 \\ g(\mathbf{a}, \lambda, s) = 0 \end{cases} \tag{2}$$

where $g(\mathbf{a}, \lambda, s)$ is the general expression of the additional constraint equation.

Starting from the initial solution $[\mathbf{a}_0, \lambda_0]$, the equilibrium path $\mathbf{c}(s)$ can be regarded as the solution of the initial value problem obtained by differentiating the augmented system in Equation (2) with respect to s:

$$\frac{\mathrm{d}\mathbf{H}(\mathbf{c})}{\mathrm{d}\mathbf{c}} \mathbf{c}' = 0, \quad \| \mathbf{c}' \| = 1, \quad \mathbf{c}(0) = [\mathbf{a}_0, \lambda_0] \tag{3}$$

where $(\cdot)'$ denotes the derivative with respect to the path parameter s.

The solution of Equation (3) can be achieved by using predictor-corrector techniques: the differential problem is initially integrated coarsely, then an iterative method is used as a stabilizer for solving locally $\mathbf{H}(\mathbf{c}(s)) = 0$.

It is worth observing that predictor-corrector continuation methods are considerably different if compared to the predictor-corrector techniques for the numerical integration of initial value problems. In fact, despite the similarity between the two strategies, *the corrector process in the continuation methods thrives on the powerful contractive properties of the solution set* $\mathbf{H}^{-1}(0)$ *for iterative methods such as Newton's method* [21]. This property is not valid for the solution curves of general initial value problems, where the corrector process converges, in the limit, to an approximating point, whose quality depends on the size of the step.

One can observe that the system of Equation (3) involves the presence of derivatives with respect to the parameter s, which is one of the main differences between arc-length and continuation methods. This is an essential feature of continuation methods and allows to easily detect critical points along the equilibrium path and to trace bifurcation branches. The main drawback is given by the need for solving a linear system for computing the derivatives, and to perform an eigenvalue decomposition for detecting critical points.

With this regard, the development of a continuation algorithm capable of tracing the complete bifurcation diagram relies on the definition of:

- a method for detecting and computing critical points, and capable of distinguishing between limit and bifurcation points
- a method for moving from the primary path to a bifurcational branch
- a strategy to follow the equilibrium path along the solution branches

Different continuation methods can be realized by referring to different parametrizations and constraint equations. The performance of the method can be modified by adopting different strategies to perform the prediction or the correction. In addition, a consistent number of procedures can be adopted to perform branch-switching or detect critical points. As result, it is possible to create a wide range of methods characterized by different performance.

In the implementation proposed here, critical points are detected looking at the positive eigenvalues of the stiffness matrix, while their classification is based on the analysis of the stiffness parameter; the eigenvector injection method is adopted for switching from the primary to the bifurcational path, while a novel energy-based path-following technique is proposed for performing the continuation.

3. Critical Points

In this section, the procedure for detecting and approximating the critical points is described. Critical points are equilibrium points corresponding to the singularity of the tangent stiffness matrix $\mathbf{K}$. According to the theory of stability of conservative systems, the stability of an equilibrium configuration is ensured by the positive definiteness of the quadratic form $\mathcal{Q}$, defined as:

$$\mathcal{Q}(\mathbf{a}) = \frac{1}{2}\mathbf{a}^T\mathbf{K}\mathbf{a} \tag{4}$$

where $\mathbf{K}$ is the tangent stiffness matrix. The transition state between a stable and an unstable equilibrium configuration is characterized by the appearance of a singularity in the matrix $\mathbf{K}$. It follows that critical points define the limits of stability of the equilibrium path. The k-th critical point can be defined by means of the following generalized eigenvalue problem:

$$(\mathbf{K} - \omega_k\mathbf{I})\mathbf{v}_k = 0 \tag{5}$$

where ω_k and $\mathbf{v}_k$ are the k-th eigenvalue and eigenvector of the stiffness matrix, respectively, whereas $\mathbf{I}$ is the identity matrix.

The eigenvalues ω_k are supposed to be arranged according to the sequence

$$\omega_1 \leq \omega_2 \leq \cdots \leq \omega_N \tag{6}$$

where N is the dimension of the stiffness matrix. When the critical state is reached, one or more eigenvalues ω_k in the sequence of Equation (6) are zero.

Critical points can be divided into limit and bifurcation points. In particular the following two conditions are considered:

$$\begin{cases} \lambda' = 0, & \text{Limit Point} \\ \hat{\mathbf{f}}^T\mathbf{v}_k = 0, & \text{Bifurcation Point} \end{cases} \tag{7}$$

The first condition of Equation (7) states that the load does not vary with respect to the path parameter in the neighborhood of a limit point. This also means that limit points are equilibrium configurations associated with a local maximum or minimum of the applied load. In most cases, limit points separate stable and unstable equilibrium paths, although this is not a rule. The presence of a limit point is commonly associated with snap-through phenomena, causing sudden snaps to a stable configuration and not adjacent to the original one. In the neighborhood of limit points there exists one unique branch, thus no further equilibrium branches need to be traced.

On the contrary, multiple equilibrium configurations exist in the neighbourhood of a bifurcation point, each of these solutions belonging to a different equilibrium branch and characterized by a different tangent. During the solution process, it is then necessary to distinguish between limit and bifurcation points to establish whether the continuation should be carried out along the emanating branches or not. For this purpose, a procedure based on the evaluation of the stiffness parameter S_p is adopted.

3.1. Stiffness Parameter

The stiffness parameter is a scalar quantity defined as [26]:

$$S_p = \frac{\frac{\mathrm{d}\mathbf{a}}{\mathrm{d}\lambda}\Big|_0^T \hat{\mathbf{f}}}{\frac{\mathrm{d}\mathbf{a}}{\mathrm{d}\lambda}^T \hat{\mathbf{f}}} \tag{8}$$

where the subscript 0 defines the initial state.

The value of S_p provides a relative measure of the incremental stiffness along the direction in which the solution is moving. During the incremental solution process, this parameter is computed through substitution of the increments into the derivatives, leading to the incremental expression:

$$S_p = \frac{\frac{1}{\Delta\lambda_0}\Delta\mathbf{a}_0^T\hat{\mathbf{f}}}{\frac{1}{\Delta\lambda_j}\Delta\mathbf{a}_j^T\hat{\mathbf{f}}} = \frac{\Delta\lambda_j}{\Delta\lambda_0}\frac{\Delta\mathbf{a}_0^T\hat{\mathbf{f}}}{\Delta\mathbf{a}_j^T\hat{\mathbf{f}}} \tag{9}$$

where $\Delta\mathbf{a}_0$ and $\Delta\lambda_0$ are the increments computed in the first load step, and $\Delta\mathbf{a}_j$ and $\Delta\lambda_j$ are the total increments computed at the current load step. As seen from Equation (9), the initial value of S_p is equal to one. Whenever the structure loses stiffness with respect to the initial value, viz. $\Delta\mathbf{a}_j^T\hat{\mathbf{f}} > \Delta\mathbf{a}_0^T\hat{\mathbf{f}}$ and $\Delta\lambda_j < \Delta\lambda_0$, the parameter S_p becomes smaller than one. On the other hand, if the structure undergoes a stiffening response, i.e., $\Delta\mathbf{a}_j^T\hat{\mathbf{f}} < \Delta\mathbf{a}_0^T\hat{\mathbf{f}}$ and $\Delta\lambda_j > \Delta\lambda_0$, S_p is greater than the unity. Furthermore, the stiffness parameter is positive on stable equilibrium branches and negative on unstable branches. As a matter of fact, S_p turns out to be negative for unstable branches because, in such cases, the increment of the load parameter is negative.

An important feature of the stiffness parameter is that, in correspondence of the limit points, it satisfies the condition:

$$S_p = 0 \tag{10}$$

as implicit in the definition of limit point itself. On the other hand, the relative stiffness is different from zero in the presence of a bifurcation point and, after crossing the point, the sign of S_p does not change.

It is worth observing that the condition of Equation (10) is hardly met during the numerical solution of the problem, as the solution is computed for a discrete set of points only. For this reason, the detection of the limit point is performed referring to a numerical approach, described in the next section, for checking the condition given by Equation (10).

3.2. Detection and Classification

Among the various strategies for the computation of critical points [23,25], the approach proposed here is based on the analysis of the sign of the eigenvalues of the tangent stiffness matrix. This approach is simple and robust, and is associated with a relatively small computational effort. It is preliminarily assumed that the eigenvalues of $\mathbf{K}$ are well separated, which implies that multiple or clustered bifurcations cannot be handled.

The tangent stiffness matrix $\mathbf{K}$ of a structure, evaluated in its initial, undeformed state, is a positive definite quantity. When a critical point is reached, one eigenvalue, at least, becomes null and, just after crossing the point, the eigenvalue becomes negative. Based on this consideration, it is straightforward to implement the condition:

$$\mathrm{sign}(\omega_k(s_i)) \neq \mathrm{sign}(\omega_k(s_{i-1})) \tag{11}$$

The critical points subsequent to the first one are captured by monitoring the sign of the lowest positive eigenvalue. In particular, the following condition is employed:

$$N_{\text{pos}}(s_i) < N_{\text{pos}}(s_{i-1}) \tag{12}$$

where N_{pos} is the number of positive eigenvalues of the tangent stiffness matrix $\mathbf{K}$.

This strategy is particularly simple as the counting of the positive eigenvalues of $\mathbf{K}$ is just needed.

Once a critical point is detected, the classification between limit and bifurcation points relies upon the valuation of the stiffness parameter (see Equation (10) as outlined in the pseudo-code reported in Algorithm 1.

Algorithm 1 Classification of critical points.

```
if sign(S_p(s_i)) ≠ sign(S_p(s_{i-1})) then
    Critical point = Limit
else if sign(S_p(s_i)) = sign(S_p(s_{i-1})) then
    Critical point = Bifurcation
end if
```

Note, s_{i-1} and s_i are the values of the path parameter s just before and just after the critical point, respectively. The criterion summarized in Algorithm 1 is based on the fact that the stiffness parameter undergoes a change of sign whenever a limit point is crossed. Hence, the critical point is a limit point if a change of sign is detected in S_p, otherwise it is a bifurcation point.

3.3. Approximation

Once critical points are identified and classified, an approximation of the critical state is needed. In continuation methods, bifurcation points are used as initial solutions for tracing bifurcation branches. It follows that the quality of the prediction affects the convergence of the solution along the bifurcation branches. An accurate prediction is then sought. On the other hand, the requirements on the accuracy of the limit point predictions are less strict, as no equilibrium branches emanate from them.

Based on these observations, limit points are determined by means of a linear approximation seeking for the zero of $S_p(s)$. Given the quantities $S_p(s_{i-1})$, $S_p(s_i)$, the linear approximation reads:

$$\begin{aligned} S_p(s) &= S_p(s_{i-1}) + \frac{S_p(s_i) - S_p(s_{i-1})}{\Delta\lambda} \left[\lambda(s) - \lambda(s_{i-1})\right] \\ \mathbf{a}(s) &= \mathbf{a}(s_{i-1}) + \frac{\Delta\mathbf{a}}{\Delta\lambda} \left[\lambda(s) - \lambda(s_{i-1})\right] \end{aligned} \tag{13}$$

where s_{i-1} and s_i are the values of the path parameter in the converged equilibrium points before and after the critical point, respectively, and:

$$\begin{aligned} \Delta\lambda &= \lambda(s_i) - \lambda(s_{i-1}) \\ \Delta\mathbf{a} &= \mathbf{a}(s_i) - \mathbf{a}(s_{i-1}) \end{aligned} \tag{14}$$

Setting $S_p(s) = 0$ in Equation (13), and denoting with an asterisk the critical state, the critical load $\lambda(s^*) = \lambda^*$ is obtained as:

$$\lambda^* = \lambda(s_{i-1}) - \frac{\Delta\lambda}{S_p(s_i) - S_p(s_{i-1})} S_p(s_{i-1}) \tag{15}$$

while the deformed configuration $\mathbf{a}(s^*) = \mathbf{a}^*$ is obtained after substituting Equation (15) into the second of Equation (13), and is obtained as:

$$\mathbf{a}^* = \mathbf{a}(s_{i-1}) + \frac{\Delta \mathbf{a}}{\Delta \lambda}(\lambda^* - \lambda(s_{i-1})) \tag{16}$$

This strategy is fast and tends to guarantee satisfactory precision for obtaining an estimate of the limit points.

Regarding the approximation of the bifurcation points, an iterative procedure is implemented to achieve improved accuracy. It is based on the polynomial approximation of the critical point $\tilde{\mathbf{x}}(s^*)$, and seeks the zero of $\omega_k(s)$. In turn, the polynomial approximation is obtained through a Taylor expansion of $\omega_k(s)$ as:

$$\omega_k(s) = \omega_k(s_i) + \omega_k'(s_i)(s - s_i) \tag{17}$$

where s_i corresponds to the value of the path parameter at the converged equilibrium solution before the critical point.

A first estimate of the critical state $\tilde{\mathbf{x}}^* = \tilde{\mathbf{x}}(s^*)$, relative to the point $\tilde{\mathbf{x}}(s_i)$, is given by:

$$\tilde{\mathbf{x}}^* = \tilde{\mathbf{x}}(s_i) + \tilde{\mathbf{x}}'(s_i)\Delta s^* \tag{18}$$

where the vector of the unknowns $\tilde{\mathbf{x}}$ and its derivative $\tilde{\mathbf{x}}'$ are defined as:

$$\tilde{\mathbf{x}} = \left\{ \mathbf{a}^{\mathrm{T}} \quad \lambda \right\}^{\mathrm{T}} \qquad \tilde{\mathbf{x}}' = \left\{ \mathbf{a}'^{\mathrm{T}} \quad \lambda' \right\}^{\mathrm{T}} \tag{19}$$

and:

$$\Delta s^* = s^* - s_i = -\frac{\omega_k(s_i)}{\omega_k'(s_i)} \tag{20}$$

and:

$$\omega'(s_i) \cong \frac{\omega(s_i) - \omega(s_{i-1})}{s_i - s_{i-1}} \tag{21}$$

Improved robustness can be achieved by modifying Equation (18) as:

$$\tilde{\mathbf{x}}(s_{i+1}) = \tilde{\mathbf{x}}(s_i) + \eta \Delta s^* \tilde{\mathbf{x}}'(s_i) \tag{22}$$

where η is a scale factor, chosen while keeping in mind that small values are associated with high accuracy, but high costs, while the opposite holds for high values of η. In the present study, a proper tradeoff between quality and computational costs was found by taking η equal to 0.1.

A new value of ω_k, corresponding to the point $\tilde{\mathbf{x}}(s_{i+1})$, can be computed and, according to Equations (18) and (20), a new estimate of $\tilde{\mathbf{x}}^*$ and Δs^* is also available. The procedure is repeated until convergence is met according to the criterion:

$$\left| \frac{\Delta s^*}{\Delta s_0} \right| \leq \mathrm{tol}_{\Delta s} \tag{23}$$

where Δs_0 is the step length adopted to start the analysis, where $\mathrm{tol}_{\Delta s}$ is the tolerance defined by the user. Based on an extensive set of preliminary investigations, a value of $\mathrm{tol}_{\Delta s} = 5 \times 10^{-3}$ is set by default in the algorithms proposed in this work. To prevent excessively long loops, the criterion of Equation (23) is accompanied by a check on the maximum number of iterations.

4. Branch-Switching Method

After detecting the critical points, a numerical strategy is needed to compute the initial solution, which is then used to start the continuation procedure along the bifurcation branches. An extensive review of branch-switching methods is available in [25]. In the present method, the eigenvector

injection method is adopted. It relies on the idea of perturbing the configuration at the critical state by using the eigenvector $\mathbf{v}_k$ associated with the eigenvalue $\omega_k(s^*) = 0$ [27].

The perturbation is introduced according to:

$$\mathbf{a}_0 = \mathbf{a}^* + \xi \frac{\mathbf{v}_k}{\| \mathbf{v}_k \|} \tag{24}$$

where ξ is a scale factor defined as:

$$\xi = \pm \frac{\| \mathbf{a}^* \|}{\tilde{\tau}} \tag{25}$$

and $\tilde{\tau}$ is a scalar variable prescribed by the user and referred to as buckling mode scale factor, while the sign of ξ determines the side of the bifurcation branch to be traced.

The initial solution is completed by:

$$\lambda_0 = \lambda^* \tag{26}$$

The tangent vector in $[\mathbf{a}_0, \lambda_0]$ is approximated as:

$$\mathbf{a}_0' = \text{sign}(\xi) \frac{\mathbf{v}_k}{\| \mathbf{v_k} \|} \tag{27}$$

$$\lambda_0' = 0 \tag{28}$$

After computing the initial solution, it is possible to start the continuation process, and the equilibrium points along the branch are so identified.

It is highlighted that a proper choice of $\tilde{\tau}$ is needed for guaranteeing convergence on the desired branch. If this value is too small, the eigenvector injection method is likely to diverge, whereas a too large value may determine a perturbation size incapable of deviating the solution on the bifurcation branch, and the continuation process is likely to converge on the primary path again [27].

Usually, suitable values of $\tilde{\tau}$ are in the range between 10 and 100. However, no general rules exist for properly selecting the value of $\tilde{\tau}$, and a trial and error strategy is, generally, the only viable solution.

To deal with this problem, it is necessary that the branch-switching algorithm allows the restart of the analysis of the bifurcation branch with a different value of $\tilde{\tau}$.

5. Path-Following Continuation Technique

In most cases, continuation techniques are developed by adopting a geometric constraint in Equation (2), an example of which is given by the Riks continuation technique [24]. This kind of constraint is well-suited for those problems dominated by nonlinearities of geometric type. On the contrary, the adoption of a geometric constraint can be source of convergence difficulties whenever the nonlinearities are mainly due to the material response that would lead to localized failure [16]. For instance, this is the case of delamination phenomena, where the strain field is localized in the surroundings of the crack tip. It follows that geometric constraints based on global quantities can be inadequate to capture the deformation process.

Starting from a recent arc-length technique proposed by the authors [17], the continuation technique proposed here tries to overcome the above mentioned difficulties by adopting a modified version of the Riks technique in conjunction with an approach based on the evaluation of the dissipated energy, as outlined in the next sections.

5.1. Modified Riks Method

The modified Riks continuation method is a modified version of the technique described in [24] and relies on a constraint equation involving the displacement vector $\mathbf{a}$ and its derivative $\mathbf{a}'$.

As opposed to original implementation proposed by Riks, the equation is adopted here in a modified form, where the contribution due to the load parameter is prevented from entering the equation. In particular, the constraint equation is formulated as:

$$g(\mathbf{a}, s) = \mathbf{a}_1'^T(\mathbf{a} - \mathbf{a}_1) - (s - s_1) = 0 \tag{29}$$

where $\mathbf{a}_1$ denotes an equilibrium point on the path, while s_1 is the value of the arc-length at this point; the terms $\mathbf{a}$ defines an arbitrary point on the surface defined by the constraint equation.

An extensive set of preliminary analyses revealed that Equation (29) offers the main advantage of preventing the doubling back of the solution, a problem often encountered when adopting the classical Riks formulation.

The continuation procedure is performed referring to a predictor-corrector technique, where the increments $\Delta\mathbf{a}$ and $\Delta\lambda$ are decomposed as:

$$\Delta\mathbf{a} = \Delta\mathbf{a}_j + \mathrm{d}\mathbf{a}\ , \qquad \Delta\lambda = \Delta\lambda_j + \mathrm{d}\lambda \tag{30}$$

where $\Delta\mathbf{a}$ and $\Delta\lambda$ are the total increments at the current step, $\Delta\mathbf{a}_j$ and $\Delta\lambda_j$ are the iterative increments at the last iteration j, and $\mathrm{d}\mathbf{a}$ and $\mathrm{d}\lambda$ are the iterative increments referred to the current $(j+1)$iteration.

The predictor solution is computed according to:

$$\Delta\mathbf{a}_0 = \mathbf{a}_1 + \mathbf{a}_1'\Delta s \qquad \Delta\lambda_0 = \lambda_1 + \lambda_1'\Delta s \tag{31}$$

The corrector phase is performed referring to the Newton's method, which is applied to solve the augmented system of Equation (2) using Equation (29) as constraint, so:

$$\begin{cases} \mathbf{K}\mathrm{d}\mathbf{a} - \hat{\mathbf{f}}\mathrm{d}\lambda = \mathbf{r} \\ \mathbf{a}_1'\Delta\mathbf{a} = \Delta s \end{cases} \tag{32}$$

where $\mathbf{r}$ is the residual at the end of the j-th iteration, defined as:

$$\mathbf{r} = \Delta\lambda_j\hat{\mathbf{f}} - \mathbf{f}_{int}(\Delta\mathbf{a}_j, \Delta\lambda_j) \tag{33}$$

Substituting Equation (30) in Equation (32), the iterative increments $\mathrm{d}\mathbf{a}$ and $\mathrm{d}\lambda$ are obtained as:

$$\mathrm{d}\mathbf{a} = \mathbf{a}_I\mathrm{d}\lambda + \mathbf{a}_{II} \tag{34a}$$

$$\mathrm{d}\lambda = -\frac{\mathbf{a}_1'^T\mathbf{a}_{II}}{\mathbf{a}_1'^T\mathbf{a}_I} \tag{34b}$$

having assumed that $\Delta s \approx \mathbf{a}_1'^T\Delta\mathbf{a}_j$, and

$$\mathbf{a}_I = \mathbf{K}^{-1}\hat{\mathbf{f}} \qquad \mathbf{a}_{II} = \mathbf{K}^{-1}\mathbf{r} \tag{35}$$

It is worth noting that Equation (34)b resembles the expression of $\mathrm{d}\lambda$ of the Riks arc-length method [24]. However, the two equations differ in the term $\mathbf{a}_1'$ of Equation (34)b, viz., the derivative of the displacement vector in the last converged equilibrium point, which is replaced by the displacement increment of the predictor step $\Delta\mathbf{a}_1$ in the Riks formulation.

To gather insight into the constraint equation developed here, it is possible to compare Equations (34)b and (29), and re-write the constraint as:

$$\mathbf{a}_1'^{\mathrm{T}}\mathrm{d}\mathbf{a} = 0 \tag{36}$$

The expression of Equation (36) defines a hyperplane in the subspace of displacements, which is normal to the vector $\mathbf{a}_1'$. In addition, Equation (36) can be thought as the projection of the Riks constraint equation onto the subspace of displacements.

After reaching convergence, the tangent vector $\tilde{\mathbf{x}}' = [\mathbf{a}', \lambda']$ is computed by solving the linear system obtained from the differentiation of Equation (32) with respect to s. The linear system is derived as:

$$\begin{cases} \mathbf{K}\mathbf{a}' - \hat{\mathbf{f}}\lambda' = 0 \\ \mathbf{a}_1'^T\mathbf{a}' - 1 = 0 \end{cases} \tag{37}$$

The vector $[\mathbf{a}', \lambda']$ defines the direction of the tangent vector, but not its orientation [22]. To this aim the scalar β is introduced as:

$$\beta = \frac{\Delta\mathbf{a}^{\mathrm{T}}\mathbf{a}'}{\parallel \Delta\mathbf{a}^{\mathrm{T}}\mathbf{a}' \parallel} \tag{38}$$

On the basis of the sign assumed by β, the orientation is defined by reversing $\tilde{\mathbf{x}}'$ when $\beta < 0$. This criterion imposes that the tangent vector points towards the direction that forms an angle smaller than 90° with respect to the last computed displacement increment $\Delta\mathbf{a}$.

5.2. Dissipated Energy Method

The adoption of a purely geometric constraint equation can be inadequate for analyzing those probelms characterized by material nonlinearities, especially in the presence of strain-softening responses. To overcome these difficulties, a second constraint, to be used in conjunction with the previous geometric one, is introduced.

The method makes use of the energy release rate G. In the context of the finite element approximation, it is obtained as [16]:

$$G = \frac{1}{2}\left(\lambda\dot{\mathbf{a}}^{\mathrm{T}} - \dot{\lambda}\mathbf{a}^{\mathrm{T}}\right)\hat{\mathbf{f}} \tag{39}$$

where the symbol $\dot{(\,)}$ denotes differentation with respect to time.

Applying a forward Euler approximation of Equation (39), the expression of the energy dissipated in the current step, $\Delta\tau$, is obtained as:

$$\Delta\tau = (\tau - \tau_1) = \frac{1}{2}\left(\lambda_1\Delta\mathbf{a}^{\mathrm{T}} - \Delta\lambda\mathbf{a}_1^{\mathrm{T}}\right)\hat{\mathbf{f}} \tag{40}$$

where τ is the total dissipated energy and τ_1 the amount of energy dissipated up to the last converged equilibrium condition. From inspection of Equation (40), a constraint equation for the continuation method can be derived as:

$$g(\Delta\mathbf{a}, \Delta\lambda) = \frac{1}{2}\left(\lambda_1\Delta\mathbf{a}^{\mathrm{T}} - \Delta\lambda\mathbf{a}_1^{\mathrm{T}}\right)\hat{\mathbf{f}} - (\tau - \tau_1) = 0 \tag{41}$$

where the parametrization is now performed with respect to the parameter τ, i.e., the dissipated energy, instead of the arc-length s. More specifically, the constraint specified by Equation (41) imposes that the energy dissipated in the current load step is equal to the amount $(\tau - \tau_1)$.

As done for the modified Riks continuation, a predictor-corrector method is employed for solving the governing equations. However, derivatives are now taken with respect to the parameter τ. The predictor step is then:

$$\Delta\mathbf{a}_0 = \mathbf{a}_1 + \mathbf{a}_1'\Delta\tau \qquad \Delta\lambda_0 = \lambda_1 + \tau\lambda_1'\Delta\tau \tag{42}$$

while the corrector phase is based upon the Newton solution of Equation (2) together with Equation (41), leading to the linearized system:

$$\begin{cases} \mathbf{K}\mathrm{d}\mathbf{a} - \hat{\mathbf{f}}\mathrm{d}\lambda = \mathbf{r} \\ \frac{1}{2}\lambda_1\Delta\mathbf{a} - \frac{1}{2}\mathbf{a}_1^{\mathrm{T}}\Delta\lambda = \Delta\tau \end{cases} \tag{43}$$

By substituting Equation (30) into Equation (43), the system can be represented in matrix form as:

$$\begin{bmatrix} \mathbf{K} & -\hat{\mathbf{f}} \\ \mathbf{h}^{\mathrm{T}} & w \end{bmatrix} \begin{Bmatrix} \mathrm{d}\mathbf{a} \\ \mathrm{d}\lambda \end{Bmatrix} = \begin{Bmatrix} \mathbf{r} \\ -g_1 \end{Bmatrix} \tag{44}$$

where:

$$\mathbf{h}^{\mathrm{T}} = \frac{\partial g}{\partial \mathbf{a}} \quad w = \frac{\partial g}{\partial \lambda} \tag{45}$$

and:

$$g_1 = g\left(\Delta\mathbf{a}_1, \Delta\lambda_1\right) \tag{46}$$

The iterative increments $\mathrm{d}\mathbf{a}$ and $\mathrm{d}\lambda$ are computed from Equation (44) applying the Sherman–Morrison formula [16]):

$$\begin{Bmatrix} \mathrm{d}\mathbf{a} \\ \mathrm{d}\lambda \end{Bmatrix} = \begin{Bmatrix} \mathbf{d}_I \\ -g_1 \end{Bmatrix} - \frac{1}{\mathbf{h}^{\mathrm{T}}\mathbf{d}_{II} - w} \begin{Bmatrix} (\mathbf{h}^{\mathrm{T}}\mathbf{d}_I + g_1)\mathbf{d}_{II} \\ -\mathbf{h}^{\mathrm{T}}\mathbf{d}_I - g_1(1 + \mathbf{h}^{\mathrm{T}}\mathbf{d}_{II} - w) \end{Bmatrix} \tag{47}$$

where the terms $\mathbf{d}_I$ and $\mathbf{d}_{II}$ are the solutions of the following linear systems:

$$\mathbf{K}\mathbf{d}_I = \mathbf{r}, \qquad \mathbf{K}\mathbf{d}_{II} = -\hat{\mathbf{f}} \tag{48}$$

After reaching convergence, the tangent vector $[\mathbf{a}', \lambda']$ is computed through the solution of the linear system obtained by taking the derivative with respect to τ of Equation (43):

$$\begin{cases} \mathbf{K}\mathbf{a}' - \hat{\mathbf{f}}\lambda' = 0 \\ \frac{1}{2}\lambda_1 \mathbf{a}'^{\mathrm{T}}\hat{\mathbf{f}} - \frac{1}{2}\lambda' \mathbf{a}^{\mathrm{T}}\hat{\mathbf{f}} - 1 = 0 \end{cases} \tag{49}$$

As observed in the previous section, the orientation of the tangent vector is not available from the solution of Equation (49), and the evaluation of the parameter β of Equation (38) is thus performed.

5.3. Switching from Geometric to Dissipation-Based Constraints

Aiming at combining the advantages (and ranges of employment) of the techniques previously outlined, a single continuation approach is developed based on the geometric and dissipation strategies. As a matter of fact, the strategy based on the dissipated energy cannot be adopted in the context of purely elastic conditions, as it would fail to converge to the equilibrium solution. Similarly, convergence issues could arise when the modified Riks approach is adopted in the presence of damage phenomena. For this reason, the two approaches are combined referring to amount of energy dissipated. In particular, two threshold values are defined, namely $\Delta\tau_{\text{switch}}$ and $\Delta\tau_{\text{sback}}$.

The analysis is started by adopting the modified Riks continuation method to trace the first load steps, which are always elastic, provided their size is chosen to be sufficiently small. When the energy dissipated in the current step exceeds $\Delta\tau_{\text{switch}}$, the dissipative continuation technique is activated. Then, as soon as the energy dissipated during the current step falls below $\Delta\tau_{\text{sback}}$, the solution strategy is switched back to the modified Riks continuation. In absence of specific motivations, the two thresholds can be generally be taken equal each other. The approach is summarized in Algorithm 2.

Algorithm 2 Switch between two continuation techniques.

if $\Delta\tau \geq \Delta\tau_{\text{switch}}$ **then**

  Dissipative Method

else if $\Delta\tau < \Delta\tau_{\text{sback}}$ **then**

  Modified Riks Continuation Method

end if

It is remarked that the adoption of the two mentioned strategies determines the presence of a double parametrization, as the modified Riks continuation method is parametrized with respect to the arc-length s, and the dissipated energy constraint equation relies on the parameter τ. This peculiarity may be source of difficulties whenever a critical point is detected between two equilibrium points computed by means of different strategies (e.g., one adopting the modified Riks continuation method and the other adopting the dissipative procedure). This aspect has to be carefully monitored during the solution process, and possible critical points so obtained should be recomputed.

6. Implementation

To clarify the various steps involved in the solution process, an overview of the method is provided in the flowchart of Figure 1. The relevant equations adopted at each steps are reported by observing that they vary according to the continuation strategy currently active – this can be either the modified Riks or the dissipation-based method.

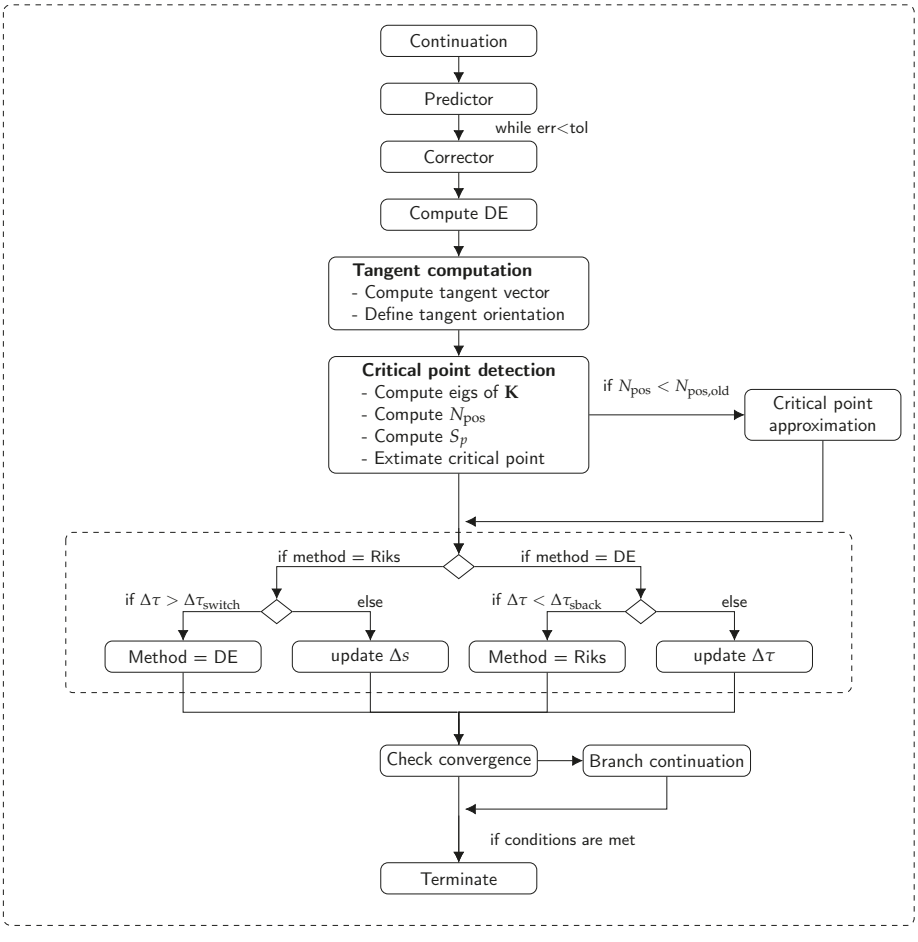

Figure 1. Flowchart of the continuation procedure.

At the beginning of the procedure, the modified Riks method is set by default, so all the equations reported henceforth are those relative to the Riks approach during the first loop. The initial predictor

step is performed on the basis of Equation (31) or (31), while Newton-Raphson iterations are repeated during the corrector phase referring to Equation (37) or (43). The procedure is arrested when the error is below the threshold defined by the tolerance. The successive step consists in the evaluation of the dissipated energy, which is used subsequently to define the continuation algorithm. The evaluation of the tangent vector requires the solution of the linear systems according to Equation (37) or (49), while the parameter β of Equation (38) is adopted for defining the orientation.

The successive phase consists in detecting the critical points, which is performed by evaluating the eigenvalues of the stiffness matrix **K**. Depending on the number of positive eigenvectors and the value of the stiffness parameter, it can be established whether a critical point is obtained, and its nature, i.e., bifurcation or limit. After detecting a critical point, the approximation procedure is activated following the procedure outlined in Section 3.3.

The method to be used in the subsequent step is defined by comparing the dissipated energy $\Delta\tau$ with the threshold values defined by the user. In the presence of dissipation phenomena, the method is set as DE, otherwise the Riks continuation is maintained. Note that the switch between the two strategies is controlled by the algorithm outlined in Algorithm 2.

The step length is finally updated following the approach presented in Ref. [17], and convergence is finally checked. Whenever one or more bifurcation points are detected throughout the iteration process, the continuation along the secondary equilibrium path is performed.

7. Results

In this section, the continuation strategy is applied to the analysis of problems involving both geometric or material nonlinearities. These kind of nonlinearities can be present independently or in combination. All the simulations are performed using the open source finite element code PyFem [29], that was used as underlying framework for implementing the numerical procedure. The elements used for the analyses are nonlinear four-node, plane-strain continuum elements. To model delamination phenomena, the cohesive element proposed by Camanho et al. [30] was implemented in PyFem. Mesh sizes were defined on the basis of preliminary convergence studies. In those analyses involving the use of cohesive elements, the mesh size was chosen to guarantee a proper description of the process zone, referring to the length l_{p} defined by [31,32]:

$$l_{\mathrm{p}} = \gamma \frac{E G_c}{N^2} \tag{50}$$

where γ is a scalar nondimensional parameter, here taken as 0.884, E denotes the Young's modulus, G_c is the fracture toughness in mode I, and N is the interfacial strength.

It is noted that the ability of the method to converge to the correct solution and to successfully trace the bifurcation diagrams is strongly affected by the choice of the parameter $\tilde{\tau}$. To this aim, preliminary tests were carried out to properly choose the value of the parameter.

The section of results is organized as follows. Two preliminary test cases, an axially compressed column and a simple one-degree-of-freedom (one-DOF) problem, are discussed in Sections 7.1 and 7.2 to illustrate the application of the method to geometrically nonlinear problems. The application of the continuation approach is then presented for two problems, a beam and an arch embedding initial cracks, in Sections 7.3 and 7.4, where materially nonlinear responses are of concern. Bifurcation plots are presented for these two cases, and the robustness of the approach is illustrated against an alternative formulation based on a purely geometric constraint equation. Finally, the procedure is presented as a mean for solving quasi-static problems for a relatively complex nonlinear example, a perforated beam loaded in mode I, which is discussed in Section 7.5.

7.1. Subcritical Bifurcation (One-DOF Problem)

This first example deals with the nonlinear response of a simple 1-DOF problem characterized by the presence of a sub-critical bifurcation point. It follows that equilibrium branches emanating

from the bifurcation are, in this case, unstable. The structure is composed by a rigid truss and a linear spring, as illustrated in Figure 2. The length l is equal to 10 mm, while the stiffness of the spring is $k_{\mathrm{g}} = 100$ N/mm. An horizontal load of intensity P is applied at the free end of the rigid bar.

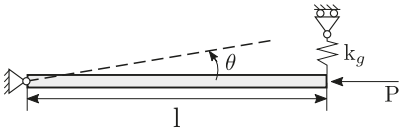

Figure 2. Sketch of the truss-spring system.

The numerical model is obtained by using a linear spring element and truss with a very high stiffness value to simulate the ideal infinite value.

The numerical predictions obtained with the proposed continuation method are compared with the analytical solution of the problem, which is given by:

$$P(\theta) = k_g l \cos(\theta) \tag{51}$$

where θ is the rotation angle and P the applied load. The results are summarized in Figure 3.

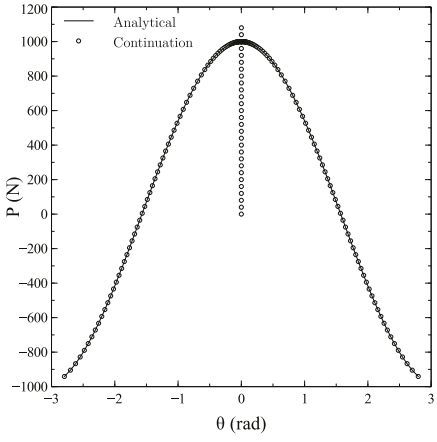

Figure 3. Bifurcation plot for the spring-truss example.

As observed, perfect matching is achieved when comparing the analytical and the numerical solution. The continuation procedure correctly identifies the overall bifurcation plot, and provides an accurate description of the three equilibrium paths emanating from the bifurcation point. Note that the solution process is carried out without activation of the dissipative continuation technique as the response is purely elastic.

7.2. Supercritical Bifurcation (Axially Compressed Column)

The second assessment regards the analysis of a column subjected to a compressive end load. The bifurcation is defined as supercritical as both sides of the bifurcation branch are locally stable equilibrium paths characterized by increasing values of the load factor [23]. A sketch of the structure is provided in Figure 4. The column is fixed at one end and free at the second one, while a concentrated force is applied at the free end. The overall length l is equal to 10 mm and the thickness h is 1 mm. An isotropic homogeneous material of modulus $E = 230$ GPa and $\nu = 0.25$ is assumed. Ten finite elements are used for discretization.

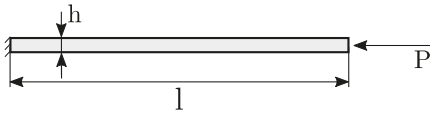

Figure 4. Cantilever beam with end compressive load.

The problem does not involve any kind of dissipative phenomena, so the modified Riks continuation approach is maintained throughout the solution process. The results are compared against those obtained by using the Crisfield arc-length approach, whose implementation in the PyFem code was already assessed in Ref. [17]. It is worth noting that the Crisfield method is not developed for tracing bifuraction diagrams in one single run. For this reason, two distinct nonlinear analyses were performed by assuming initial imperfections with opposite sign and shape equal to the first buckling mode. On the contrary, the continuation method allows to plot the bifuraction diagram in one single run, with no need for introducing initial imperfections.

The results are summarized in Figure 5, where the axial displacement of the bottom-most corner of the column is reported against the axial load.

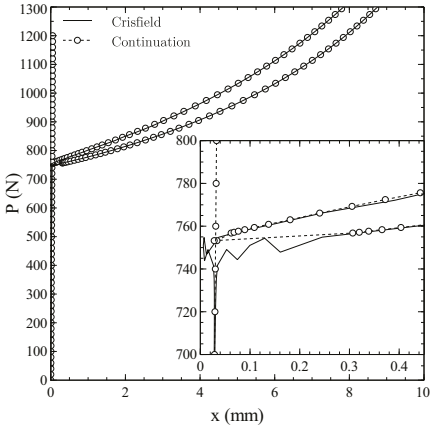

Figure 5. Bifurcation plot for axially compressed column.

The close matching with the results obtained using the Crisfield method demonstrates the ability of the continuation method to deal with the solution of equilibrium branches arising from supercritical bifurcation points.

In addition, the quality of the prediction can be noted by inspection of the region in the neighborhood of the bifurcation. As seen from the zoom of the plot, the continuation approach provides a precise description of the equilibrium branches departing from the critical point. In contrast, the Crisfield approach undergoes small oscillations, and convergence to spurious equilibrium configurations is observed in proximity of the bifurcation. Again, it is remarked that no initial imperfections are needed within the context of the continuation approach, so the bifurcation is precisely detected.

7.3. Beam Containing an Initial Crack

Previous test cases are restricted to geometrically nonlinear phenomena, and material nonlinearities are not accounted for. In the example presented here, a beam containing an initial delamination is considered and the propagation of the crack is accounted for by making use of cohesive elements characterized by a bilinear cohesive law. Further details regarding the implementation of these elements in the PyFem code are available in [33]. A sketch of the structure is reported in Figure 6.

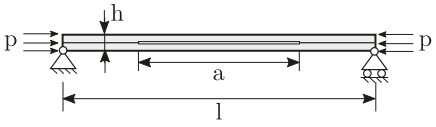

Figure 6. Beam with initial crack.

The beam's length and thickness are denoted with l and h, respectively. The central portion of the beam is characterized by the presence of an initial crack, whose length is equal to a. The material is isotropic with modulus $E = 230$ GPa and Poisson's ratio 0.25, and a plane strain constitutive law is assumed.

The structure is hinged at the bottom left vertex, while the translation along the direction normal to the beam axis is constrained at the bottom right end. The load is introduced in the form of a compressive force per unit length of magnitude p.

As seen from Figure 6, the structure is divided into two equal parts with respect to the midline running parallel to the beam axis. The two outer portions are connected by means of two layers of cohesive elements. The fracture toughnesses in mode I and II are taken as 0.5 N/mm, while the interfacial strengths are fixed at 1.0 N/mm^2. The penalty stiffness of the cohesive elements is 5000 N/mm^3.

The centrally located pre-damaged area is simulated by means of cohesive elements with reduced properties, whose aim is to avoid interpenetration between the upper and lower parts of the structure during the deformation process [32].

The finite element model is composed of 200 nonlinear shell elements and 20 cohesive elements. Note, the mesh size is chosen in order to guarantee the presence of 4/5 elements in the process zone, whose size is estimated referring to Equation (50).

In the first part of the procedure, the primary equilibrium path is computed. Starting from the undeformed configuration, the load is progressively increased, and the corresponding equilibrium points are found. During this first phase, the eigenvalues of the stiffness matrix are determined at each step of the iterative process, and the presence of critical points is verified. Whenever a critical point is detected, it is approximated referring to the procedure outlined in Section 3, depending on whether it is a limit or a bifurcation point. As an example, the initial part of the primary path is reported in Figure 7a, just after the detection of the first bifurcation point. The procedure is then switched to the continuation procedure, and the tracing of the equilibrium path restarts from the last equilibrium point available. The complete primary path up to a load of 300 N is presented in Figure 7b together with the four bifurcation points detected.

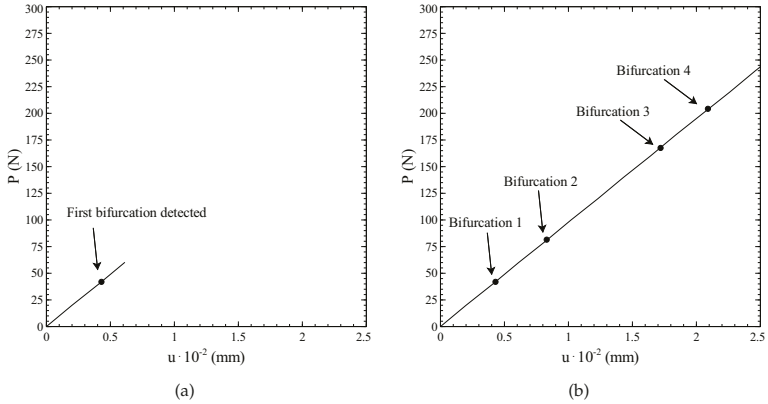

Figure 7. Primary equilibrium path: (**a**) detection of the first critical point, (**b**) full equilibrium path.

As reported in Figure 7b, the primary path is characterized by an almost linear behaviour, consisting of a progressive shortening of the beam with no bending deflections. After the first bifurcation point, the primary equilibrium path becomes unstable. However, the absence of initial imperfections and the symmetry of the problem make its computation possible. It is also noted that no damage phenomena are associated with this primary equilibrium configurations.

In the second phase of the solution process, the equilibrium branches departing from the bifurcation points are computed. The branch associated with a positive sign of the first buckling mode is plotted in Figure 8a, while the branch obtained by assuming a negative sign is reported in Figure 8c. The two corresponding deformed shapes are presented in in Figure 8b,d, respectively.

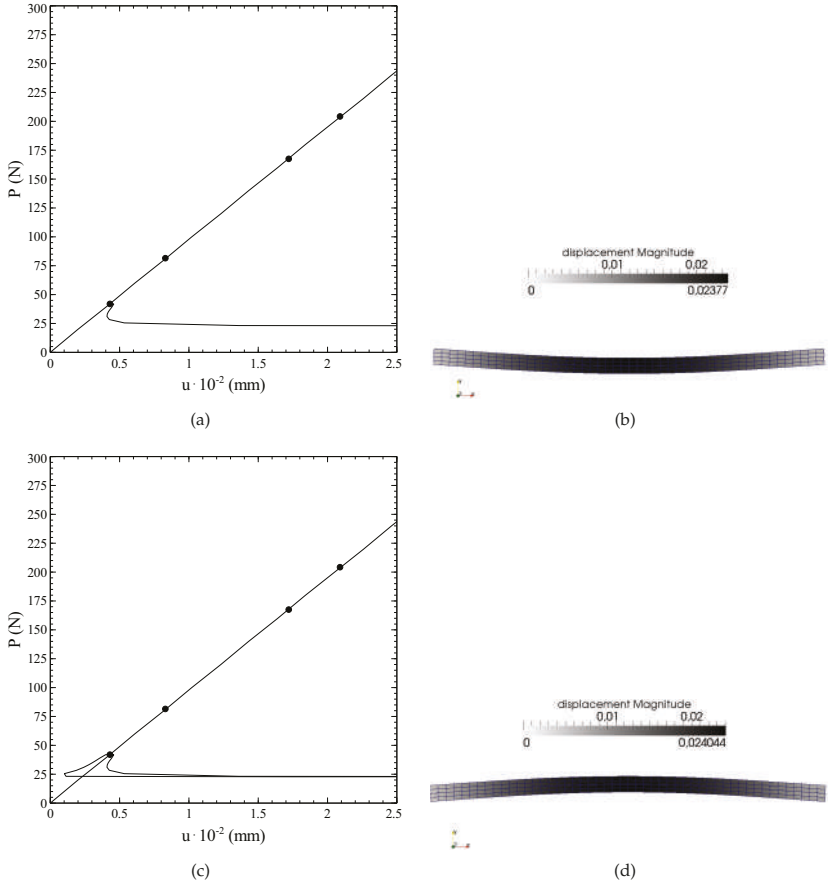

Figure 8. Computation of the first bifurcation branch: (**a**) positive side of the branch, (**b**) corresponding deformed shape, (**c**) negative side of the branch, (**d**) corresponding deformed shape.

In a similar fashion, the procedure is repeated for all the bifurcations points. The results of Figure 9 illustrate the force-displacement curves and the corresponding deformed shapes during the evaluation of the fourth equilibrium branch.

The curve of Figure 9c corresponds also with the complete bifurcation diagram, comprehensive of all the equilibrium paths departing from the bifurcation points detected.

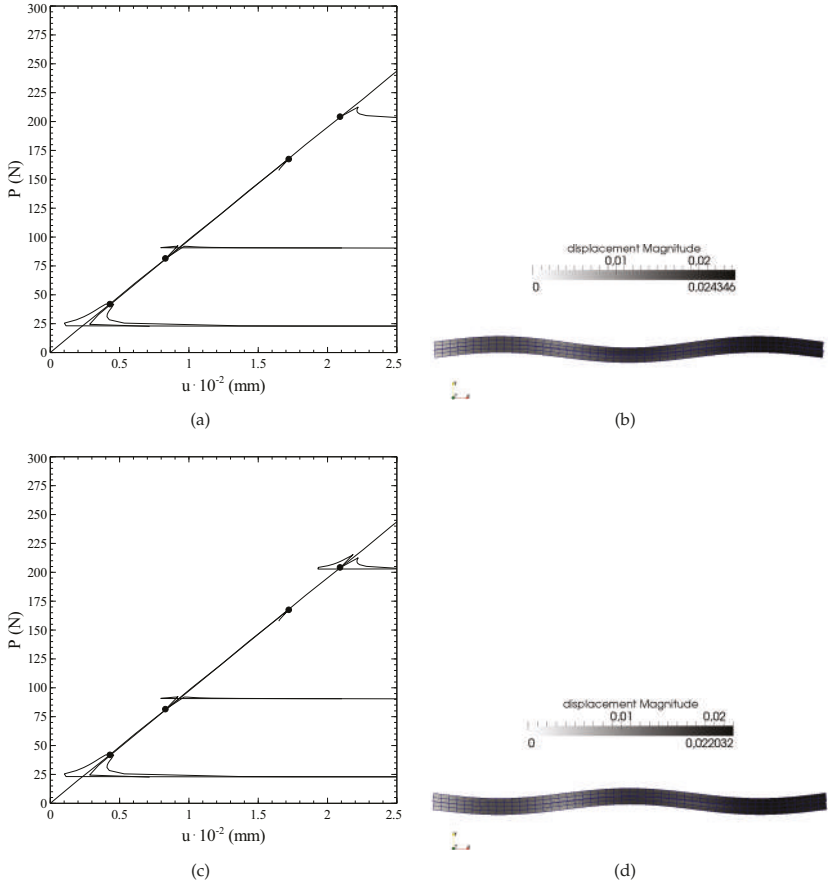

Figure 9. Computation of the fourth bifurcation branch: (**a**) positive side of the branch, (**b**) corresponding deformed shape, (**c**) negative side of the branch, (**d**) corresponding deformed shape.

A summary of the deformed configurations obtained at the end of the loading process along the four equilibrium branches is reported in Figure 10.

From Figure 10 it can be noted that all the deformed shapes but the third one exhibit the typical buckled pattern of pristine beams. In this case, the deformed configurations are characterized by one to three half-waves, and a partial damaging of the cohesive elements is observed due to the shear transfer mechanism between the upper and lower portion of the beam. As result, the fracture is dominated by a mode II mechanism. As observed from Figure 9c, the corresponding load-deflection curves are associated with a slight drop of load just after the bifurcation point, motivated by the contemporary onset of the buckling half-waves and damage mechanism in mode II. Afterwards, no additional load is carried by the structure, and the shortening happens at a constant load level.

A different response is observed for the third equilibrium branch, whose post-buckled pattern is reported in Figure 10c. In this case, the damage mechanism is governed by mode I component, with a clear opening between the upper and lower portions of the structure. The propagation is unstable and sudden, and is responsible for a drastic drop of load, not clearly visible from the complete bifurcation diagram. For clarity purposes, the force-displacement curve is reported in Figure 11 by restricting the plot to the third equilibrium branch, where the collapse induced by the onset of the buckling phenomenon can be fully appreciated.

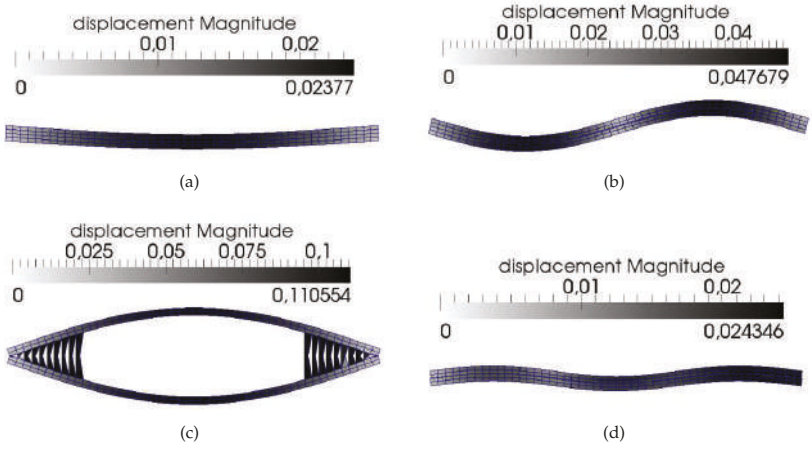

Figure 10. Post-critical deformed shapes along the equilibrium paths 1 to 4: (**a**) path 1, (**b**) path 2, (**c**) path 3, (**d**) path 4.

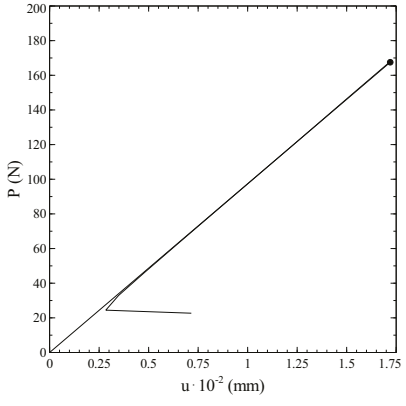

Figure 11. Detail of the force-displacment curve for the equilibrium branch 3.

The unloading phase happens in a steep manner, along a path which is close, but distinct, from loading one. After the drop of load, all the cohesive elements are completely damaged, thus the solution is arrested.

It is interesting to investigate the performance of the method in terms of number of iterations along the equilibrium branches previously considered. The results are summarized in Table 1 with regard to two different solution procedures. In one case, denoted with hybrid, the procedure refers to the combined geometric-dissipative approach summarized in Figure 1; in the other case, denoted with geometric, the dissipative constraint is removed, and the procedure is forced to adopt the purely geometric Riks constraint. As far as the number of iterations is a function of the parameter $\tilde{\tau}$ of Equation (25), a preliminary assessment was performed to obtain the values of $\tilde{\tau}$—reported in the brackets—guaranteeing the smallest number of iterations.

Table 1. Number of increments using different constraint equations. ($\bar{\tau}$ in the parenthesis).

Constraint	N. of Incr.						N. of Iter.
	Primary	Branch 1	Branch 2	Branch 3	Branch 4	Tot	Tot
Hybrid	10	18 (10)	90 (10)	35 (50)	40 (20)	193	332
Geometric	15	40 (10)	22 (10)	38 (20)	31 (30)	146	150

As summarized in Table 1, the adoption of the dissipative constraint determines an increase of the total number of iterations with respect to the modified Riks case. The increase is motivated by the mainly geometric nature of the post-critical configurations associated with the equilibrium branches 1, 2 and 4. In these cases, the sources of nonlinearity can be mostly attributed to the deflected patterns, as seen from Figure 10, thus the advantages offered by a dissipation based-criterion cannot be fully appreciated. On the contrary, the number of iterations is slightly smaller when the combined dissipative-geometric constraint is adopted for tracing the third equilibrium branch, i.e., the one characterized by the opening of the initial crack. While the comparison in terms of iterations seems to suggest the adoption of a purely geometric constraint, it is important to notice that the quality of the predictions in the two cases is not equal. In particular, the adoption of a geometric constraint tends to determine relatively large increments, and the step size can be hardly controlled. It follows that the equilibrium path is not accurately described. On the other hand, the adoption of a dissipative constraint provides an excellent control of the step size, so enabling to trace the equilibrium branches with improved degree of refinement.

7.4. Fixed-Fixed Arch

An additional example is discussed regarding the configuration illustrated in Figure 12.

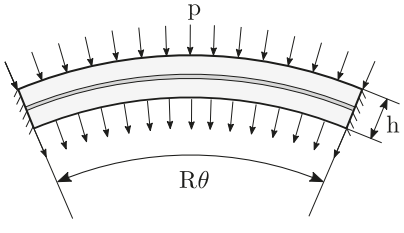

Figure 12. Arch subjected to distributed pressure.

The structure is an arch characterized by a radius R equal to 10 mm, an arc-length angle θ of $\pi/4$ radians, and a radius-to-thickness ratio of 100. The material elastic properties are those considered in the previous example. The two ends of the beam are fixed, while a uniformly distributed force per unit length p is applied along the radial direction at the upper and lower surface of the arch, as illustrated in Figure 6. In order to account for material nonlinear responses, a layer of cohesive elements is introduced along the midline of the arch. In this case the fracture toughnesses in mode I and II are 0.5 N/mm, while the interfacial strengths are equal to 15 N/mm^2. The mesh is made of 100 nonlinear shell elements and 50 cohesive elements.

The bifurcation plot is presented in Figure 13 by reporting the nodal displacement of the central upper node versus the nodal force applied at the same node.

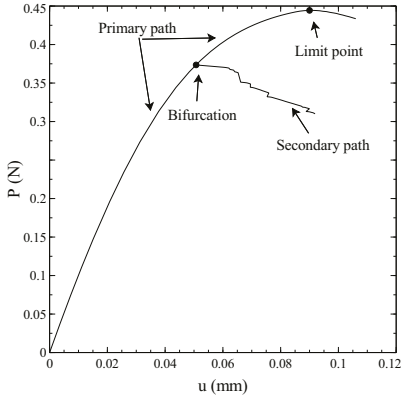

Figure 13. Bifurcation plot of the arch subjected to distributed pressure.

In this case, two critical points are detected along the primary path. The first one is a bifurcation point, as seen from the equilibrium path emanating from it. The second one is a limit point, and corresponds to a local maximum of the load carried by the structure. The primary path is now characterized by a nonlinear behaviour, where a progressive reduction of the linear stiffness is observed. No damage phenomena are observed along the major part of this path, as cohesive elements display the initiation of damage mechanisms just in the surroundings of the limit point.

The secondary equilibrium branch is characterized by an unloading phase, associated with a progressive failure of all the cohesive elements in mode II. From the curve of Figure 13, it can be observed the step-wise shape of the secondary equilibrium path, which is related to the failure of the interface elements. In any case, the layer of cohesive elements is distributed along all the overall structure, thus the role played by dissipative phenomena is significant.

To further address the relevance of dissipative phenomena, a comparison is presented between the performances achieved by considering the geometric-dissipative constraint, and those obtained with a run based on the adoption of a purely geometric constraint. The number of increments and iterations to complete the analysis are summarized in Table 2, where the optimal value of the parameter $\tilde{\tau}$ is reported in the brackets.

Table 2. Number of increments using different constraint equations. ($\tilde{\tau}$ in the parenthesis).

Constraint	**N. of Incr.**			**N. of Iter.**
	Primary	Branch 1	Total	
Hybrid	47	160 (20)	207	276
Geometric	47	160 (30)	207	445

In this test, the advantages offered by the use of the hybrid constraint are clearer. While the number of increments along the two paths is, by chance, identical, the total number of iterations is much smaller when the energy control is active. The reduction of iterations determines a gain of approximately 15% in terms of computational time. In fact, the post-bifurcational response is dominated by the material nonlinearities, so the control over the dissipated energy is the more efficient approach.

7.5. Perforated Beam

This final example illustrates the use of the continuation approach as a mean for solving a nonlinear problem characterized by a complex response, where nonlinearites are due to geometric and material behaviour. The numerical solution strategy is not used here for tracing the bifurcation plot, but for obtaining the primary equilibrium path, as commonly done when solving a nonlinear

quasi-static problem. The problem was analyzed using arc-length hybrid strategies in a previous work form the authors [17].

The analysis regards the mode I opening of a cantilever beam characterized by the presence of five equally spaced, square holes. The beam is loaded at the tip by means of two concentrated forces, as indicated in Figure 14, where all the relevant geometric dimensions are reported. An isotropic material is considered, with modulus equal to 1000 MPa and Poisson's ratio 0.3.

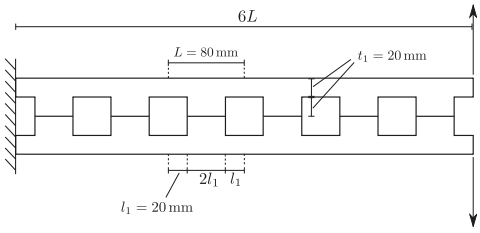

Figure 14. Cantilever perforated beam: geometry and dimensions.

To capture the onset and the propagation of the crack, a layer of cohesive elements is introduced along the horizontal line of symmetry of the structure. The fracture toughnesses in mode I and II are equal to 0.01 N/mm, while the interfacial tensile and shear strength are taken as 1 N/mm^2. A penalty stiffness of 100 N/mm^3 is assumed. The resulting finite element model is composed of 288 two-dimensional, plane-strain continuum elements, and 24 cohesive elements.

The curves reporting to the vertical displacement of the loaded nodes are plotted against the applied load in Figure 15. The comparison is presented for two different strategies. In one case the continuation method is applied as implemented, thus allowing the automatic switch between geometric and dissipative constraint. In the second case the constraint is forced to be of purely geometric, with the scope of illustrating the advantages due to the hybrid continuation approach presented here.

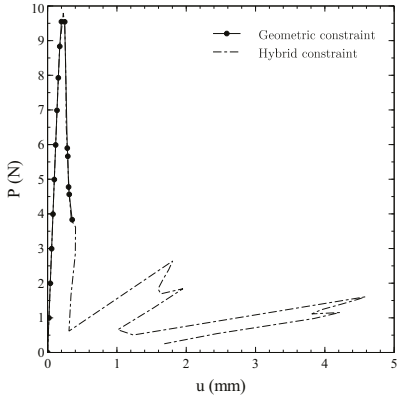

Figure 15. Force-displacement curve using different constraints.

As seen from the figure, the adoption of a purely geometric constraint leads to a premature failure of the analysis, which terminates along the first descending branch of the curve. On the contrary, the hybrid implementation is capable of capturing the subsequent portions of the equilibrium path. Note that each sudden drop is due to the opening of the holes. After the first peak, a snap-back behaviour can be observed, where a secondary snap characterizing the unloading phase. Indeed, a partial recovery of the load-carrying capability is observed in the post-peak region, followed by another snap-back.

The deformed shapes at the end of the analysis are reported in Figure 16.

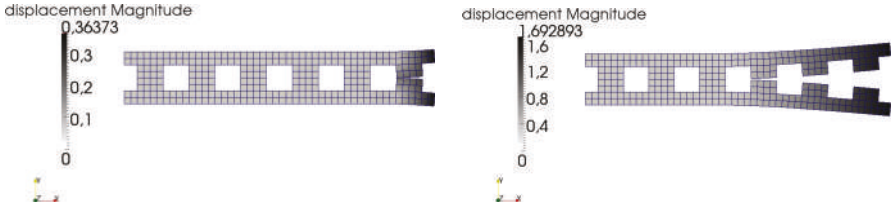

(a) (b)

Figure 16. Deformed configuration at the end of the analysis by using: (**a**) geometric constraint, (**b**) hybrid constraint.

While the initiation of the opening of the first crack coincides with the failure of the purely geometric approach (Figure 16a), the improved robustness properties of the hybrid method are clearly visible from Figure 16b.

It is useful to illustrate the comparison between the two strategies in terms of numerical performance of the solution procedure, as done in Table 3.

Table 3. Summary of numerical performance for the perforated cantilever beam.

Constraint	N. of Incr.	N. of Iter.	Step Cuts	N. of Fully Damaged Coh. Els
Geometric	17	59	3	2
Hybrid	35	85	1	12

The results provide a clear picture of what highlighted by inspection of the force-displacement response. In particular, the geometric continuation is capable of obtaining the solution in the initial part of the curve, where 17 increments are performed. At the onset of the first crack, the step length is reduced 3 times, demonstrating the difficulties experienced by the method to obtain the solution. Then, after reaching the complete damaging of two cohesive elements, the analysis is terminated.

On the other hand, the hybrid strategy is capable of reaching the condition characterized by a number of 12 completely damaged cohesive elements. No step length reductions are observed. Clearly, the total time for the analysis and the number of increments are higher.

8. Conclusions

This work discussed the development and implementation of a numerical continuation technique for analyzing structural problems characterized by geometric and material nonlinearities. The continuation strategy can be successfully applied for detecting bifurcation and limit points as well as tracing the equilibrium paths, which is a useful mean for gathering insight into the response of the structure. For instance, the complete post-buckling behaviour can be assessed by performing one single quasi-static analysis, with no needs to introduce initial imperfections in the finite element model.

The effectiveness of the current implementation was checked by means of illustrative examples, where cohesive elements were employed for capturing the onset and propagation of cracks. Main advantage of the approach is the robustness of the numerical solution strategy, which is based upon a hybrid constraint equation that includes both geometric and dissipative considerations. Thus crack propagation phenomena can be accurately predicted, whilst standard geometric-based approaches tend to undergo converge issues. In addition, the method can be used as a technique for solving quasi-static nonlinear problems, when the analysis of secondary equilibrium paths is not of concern. The effectiveness of the approach was illustrated with a test case characterized by the presence of sharp snap-backs, and secondary snap-backs. The analyst can benefit for the adoption of

a unique, integrated solution scheme, which can be used for solving the structural boundary value problem, as well as exploring multiple equilibrium paths with improved robustness.

Acknowledgments: This study did not receive funds.

Author Contributions: The two authors equally contributed to the present paper.

Conflicts of Interest: The authors declare no conflict of interest.

References

1. Buermann, P.; Rolfes, R.; Tessmer, J.; Schagerl, M. A Semi-Analytical Model for Local Post-Buckling Analysis of Stringer- and Frame-Stiffened Cylindrical Panels. *Thin Walled Struct.* **2006**, *44*, 102–114. [CrossRef]
2. Brubak, L.; Hellesland, J. Semi-analytical Postbuckling and Strength Analysis of Arbitrarily Stiffened Plates in Local and Global Bending. *Thin Walled Struct.* **2007**, *45*, 620–633. [CrossRef]
3. Vescovini, R.; Bisagni, C. Two-step procedure for fast post-buckling analysis of composite stiffened panels. *Comput. Struct.* **2013**, *128*, 38–47. [CrossRef]
4. Barriére, L.; Marguet, S.; Castanié, B.; Cresta, P.; Passieux, J.C. An adaptive model reduction strategy for post-buckling analysis of stiffened structures. *Thin Walled Struct.* **2013**, *73*, 81–93. [CrossRef]
5. Milazzo, A.; Oliveri, V. Post-buckling analysis of cracked multilayered composite plates by pb-2 Rayleigh–Ritz method. *Compos. Struct.* **2015**, *132*, 75–86. [CrossRef]
6. Cricrì, G.; Perrella, M.; Calì, C. Experimental and numerical post-buckling analysis of thin aluminium aeronautical panels under shear load. *Strain* **2014**, *50*, 208–222. [CrossRef]
7. Citarella, R.; Giannella, V.; Lepore, M. DBEM crack propagation for nonlinear fracture problems. *Frattura ed Integrità Strutturale* **2015**, *34*, 514–523.
8. Pook, L. Determination of fatigue crack paths. *Int. J. Bifurc. Chaos* **1997**, *7*, 469–475. [CrossRef]
9. Riks, E. The Application of Newton's Method to the Problem of Elastic Stability. *J. Appl. Mech.* **1972**, *39*, 1060–1065. [CrossRef]
10. Wempner, G. Discrete approximations related to nonlinear theories of solids. *Int. J. Solids Struct.* **1971**, *7*, 1581–1599. [CrossRef]
11. Crisfield, M. A fast incremental/iterative solution procedure that handles "snap-through". *Comput. Struct.* **1981**, *13*, 55–62. [CrossRef]
12. May, I.; Duan, Y. A local arc-length procedure for strain softening. *Comput. Struct.* **1997**, *64*, 297–303. [CrossRef]
13. Schellekens, J.; Borst, R.D. A non-linear finite element approach for the analysis of mode-I free edge delamination in composites. *Int. J. Solids Struct.* **1993**, *30*, 1239–1253. [CrossRef]
14. Borst, R.D. Computation of post-bifurcation and post-failure behavior of strain-softening solids. *Comput. Struct.* **1987**, *25*, 211–224. [CrossRef]
15. Gutierrez, M. Energy release control for numerical simulations of failure in quasi-brittle solids. *Commun. Numer. Methods Eng.* **2004**, *20*, 19–29. [CrossRef]
16. Verhoosel, C.; Remmers, J.; Gutierrez, M. A dissipation-based arc-length method for robust simulation of brittle and ductile failure. *Int. J. Numer. Methods Eng.* **2009**, *77*, 1290–1321. [CrossRef]
17. Bellora, D.; Vescovini, R. Hybrid geometric-dissipative arc-length methods for the quasi-static analysis of delamination problems. *Comput. Struct.* **2016**, *175*, 123–133. [CrossRef]
18. Rastiello, G.; Riccardi, F.; Richard, B. Discontinuity-scale path-following methods for the embedded discontinuity finite element modeling of failure in solids. *Comput. Methods Appl. Mech. Eng.* **2019**, *349*, 431–457. [CrossRef]
19. Davidenko, D. On a new method of numerical solution of systems of nonlinear equations. *Doklady Akademii Nauk SSSR* **1953**, *4*, 601–602. [in Russian].
20. Davidenko, D. On approximate solution of systems of nonlinear equations. *Ukrainian Math. J.* **1953**, *5*, 196–206. [in Russian].
21. Allgower, E.; Georg, K. *Introduction to Numerical Continuation Method*; SIAM: Philadelphia, PA, USA, 2003.
22. Rheinboldt, W. Numerical Analysis of Continuation Methods for Nonlinear Structural Problems. *Comput. Struct.* **1981**, *13*, 103–113. [CrossRef]
23. Seyde, R. *Practical Bifurcation and Stability Analysis*; Springer: New York, NY, USA, 2009.

24. Riks, E. An incremental approach to the solution of snapping and buckling problems. *Int. J. Solids Struct.* **1979**, *2*, 529–551. [CrossRef]
25. Shi, J. Computing critical points and secondary paths in nonlinear structural stability analysis by the finite element method. *Comput. Struct.* **1996**, *58*, 203–220. [CrossRef]
26. Bergan, P.; Horrigmoe, G.; Bråkeland, B.; Søreide, T. Solution techniques for non- linear finite element problems. *Int. J. Numer. Methods Eng.* **1978**, *12*, 1677–1696. [CrossRef]
27. Wagner, W.; Wriggers, P. A simple method for the calculation of postcritical branches. *Eng. Comput.* **1988**, *5*, 103–109. [CrossRef]
28. Magnusson, A.; Svensson, I. Numerical treatment of complete load–deflection curves. *Int. J. Numer. Methods Eng.* **1998**, *41*, 955–971. [CrossRef]
29. Borst, R.D.; Crisfield, M.; Remmers, J.; Verhoosel, C. *Non-Linear Finite Element Analysis of Solids and Structures*; John Wiley & Sons: New York, NY, USA, 2012.
30. Camanho, P.; Dávila, C.G.; Moura, M.D. Numerical simulation of mixed-mode progressive delamination in composite materials. *J. Compos. Mater.* **2003**, *37*, 1415–1424. [CrossRef]
31. Turon, A.; Dávila, C.; Camanho, P.; Costa, J. An engineering solution for using coarse meshes in the simulation of delamination with cohesive zone models. Available online: https://ntrs.nasa.gov/search.jsp?R=20050160472 (accessed on 30 October 2019).
32. Vescovini, R.; Dávila, C.; Bisagni, C. Failure analysis of composite multi-stringer panels using simplified models. *Compos. B Eng.* **2013**, *45*, 939–951. [CrossRef]
33. Bellora, D. Quasi-static solution procedures for the finite element analysis of delaminations. M.Sc. Thesis, Politecnico di Milano, Milano, Italy, 2015.

Mathematical and Computational Applications

MDPI

Article

Hydrodynamic and Acoustic Performance Analysis of Marine Propellers by Combination of Panel Method and FW-H Equations

Abouzar Ebrahimi [1], Mohammad Saeed Seif [1,*] and Ali Nouri-Borujerdi [2]

[1] Center of Excellence in Hydrodynamic and Dynamic of Marine Vehicles, Sharif University of Technology, Tehran, Iran
[2] Mechanical Engineering Department, Sharif University of Technology, Tehran, Iran
* Correspondence: seif@sharif.edu

Received: 13 August 2019; Accepted: 5 September 2019; Published: 9 September 2019

Abstract: The noise emitted by ships is one of the most important noises in the ocean, and the propeller noise is one of the major components of the ship noise. Measuring the propeller noise in a laboratory, despite the high accuracy and good reliability, has high costs and is very time-consuming. For this reason, the calculation of propeller noise using numerical methods has been considered in recent years. In this study, the noise of a propeller in non-cavitating conditions is calculated by the combination of the panel method (boundary element method) and solving the Ffowcs Williams-Hawkings (FW-H) equations. In this study, a panel method code is developed, and the results are validated by the experimental results of the model tests carried out in the cavitation tunnel of the Sharif University of Technology. Software for numerical calculation of propeller noise, based on FW-H equations, is also developed and the results are validated by experimental results. This study shows that the results of the panel method code have good agreement with experimental results, and that the maximum error of this code for the thrust and torque coefficients is 4% and 7%, respectively. The results of the FW-H noise code are also in good agreement with the experimental data.

Keywords: panel method; marine propeller; noise; FW-H equations; experimental test

1. Introduction

In recent years, the use of numerical methods has become very common in modeling the flow around marine propellers. Although the experimental methods have a higher accuracy and reliability than numerical methods, the higher costs and the need for special equipment has caused numerical methods to be preferred.

The boundary element method (BEM) is one of the methods used to solve the governing equations of fluid mechanics, acoustics, electromagnetics, etc. In this method, using mathematical theorems, the equations from the interior of the solution domain are transferred to the boundaries of the domain. Therefore, compared to other numerical methods such as finite element or finite volume method which interior of domain should be considered, BEM exhibits less solution time and computation cost and therefore it is preferred to other methods.

The panel method is one of boundary element methods. In this method, the surface of the body is divided into small panels and a combination of source and doublets is distributed to each panel. After calculating the strength of sources and doublets, velocity and pressure distribution on surface panels can be obtained. For lifting bodies, a wake surface should be assumed at the trailing edge of body, and the effect of panels of this surface on body panels should be considered.

In recent decades, the panel method has been widely used to solve the flow around the bodies, especially marine propellers. A literature review shows that a lot of research has been done on the

use of the panel method for the hydrodynamic analysis of objects. For instance, Hess and Smith [1], in 1962, invented the panel method for analyzing the motion of three dimensional bodies in fluid. The formulation of these researchers was presented for the arbitrary three dimensional bodies and could not be used for lifting bodies. In 1972, Hess [2] developed this method for lifting bodies and calculated the pressure distribution around an aircraft model and lift force. The panel method was first used in 1985 by Hess and Valarezo [3] to model the flow around the ship propeller. In this study, they obtained the pressure distribution around a propeller using quadrilateral panels and calculated the thrust and torque coefficients. In 2010, Baltazar et al. [4] modeled cavitation around a propeller using the panel method. The results of this study show that the panel method can model cavitation on propeller blades with good accuracy. Also, several papers have been published between the years 1985 to 2010, but most have done similar work.

In 2010, Gaggero et al. [5] modeled the flow around the propeller using the panel method and computational fluid dynamics. The results of the panel method show that this method has a good and acceptable accuracy compared to the CFD method.

According to the importance of propeller noise, various methods have been proposed to reduce it. Methods used to reduce the noise of marine propellers can be divided into two main methods, namely:

- Using equipment
- Modification of the geometry

Each of these methods is fully described in a review paper published by Ebrahimi et al. [6]. In recent years, calculating the noise of marine propellers using numerical methods has also been developed by researchers. For numerical calculation of noise, a numerical method such as panel method is required to obtain flow quantities and then these quantities are used as input for calculation of noise for a receiver at the desired location. Seol and Park [7] carried out several experiments on a propeller model in MOERI cavitation tunnel and measured the noise of propeller in cavitating and non-cavitating condition. Also, they used combination of time domain acoustic analogy and panel method for the numerical investigation of the propeller noise.

In another study by Kellett et al. [8] in 2013, the noise generated by the propeller of a LNG carrier ship was measured numerically and experimentally. Bagheri et al. [9] conducted a research on a three bladed propeller of the Gawn series and used the ANSYS Fluent commercial software for calculation of the propeller noise. Testa et al. [10] calculated the noise of E779A propeller model by using the FW-H equations in presence of unsteady sheet cavitation. They also used potential-based panel method for modelling flow around propeller. Gorji et al. [11] performed a research on calculation of noise of a marine propeller using a RANS solver in the low frequencies band.

Bagheri et al. [12] carried out some numerical and experimental tests on the noise of marine propellers and the effects of cavitation on the sound pressure level of propeller. They used viscous flow with FW-H solver for noise calculation.

In present research, a boundary element method is used for hydrodynamic analysis of marine propellers. Also, the FW-H equations are used for acoustic performance analysis of these propellers. For this purpose, two codes have been developed by authors and their results validated using experimental tests carried out in cavitation tunnel of Sharif University of Technology. The most significant novelty of our paper is that we used experimental noise measurements to validate the results of the FW-H equations code.

2. Formulation of the Panel Method

For development of the panel method formulation for marine propeller, the flow around propeller in computational domain of Ω is assumed to be irrotational, incompressible and inviscid. By these assumptions, the flow governing equations (Navier-Stokes equation) are simplified into

the three-dimensional Laplace equation where is $\nabla^2\phi$. By using Green's second identity, the general solution of this equation is as follows [13]:

$$\int_{\Omega}\left(\phi_1\nabla^2\phi_2-\phi_2\nabla^2\phi_1\right)dV=\int_{S}\left(\phi_1\nabla\phi_2-\phi_2\nabla\phi_1\right)\cdot\vec{n}dS \tag{1}$$

On the right-hand side of the Equation (1), integrating is done on the surface S, which includes the body surface, Kutta strip and wake surfaces of the object (Figure 1). If the points P, Q and O are defined as the control point, source point and the origin of the coordinates, respectively, the distance vector $\vec{R}$ is defined as follows:

$$\vec{R}=\vec{OQ}-\vec{OP}\qquad r=\left|\vec{R}\right| \tag{2}$$

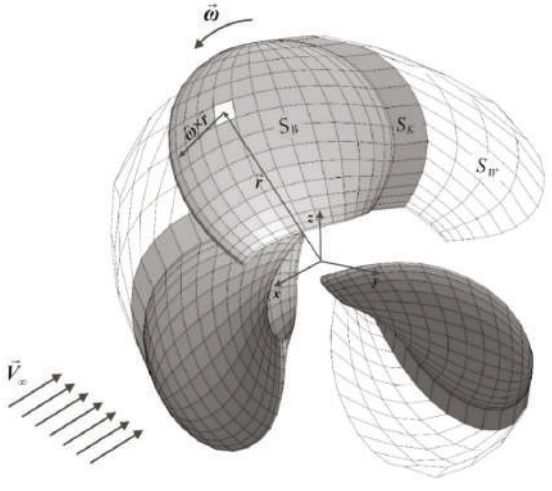

Figure 1. Body surface, Kutta strip and wake surface.

Now, if we suppose $\phi_1=1/r$ and $\phi_2=\phi$, where ϕ is potential of flow, Equation (1) becomes:

$$\int_{\Omega}\left(\frac{1}{r}\nabla^2\phi\right)dV-\int_{\Omega}\left(\phi\nabla^2\frac{1}{r}\right)dV=\int_{S}\left(\frac{1}{r}\nabla\phi-\phi\nabla\frac{1}{r}\right)\cdot\vec{n}dS \tag{3}$$

In the case where P is outside of the domain Ω, then ϕ_1 and ϕ_2 satisfy Laplace's equation [13]. Therefore, the first and second terms on the left-hand side of Equation (3) will be zero. Then:

$$\int_{S}\left(\frac{1}{r}\nabla\phi-\phi\nabla\frac{1}{r}\right)\cdot\vec{n}dS=0 \tag{4}$$

In the case of flow around the propeller, the point P is located on the body surface. When point P approaches to point Q and $r\to 0$, the above integral is singular $(1/r\to\infty)$. Therefore, the point P should be excluded from S using a small hemisphere of radius ε. Therefore, the integration region will change to $S+S_\varepsilon$:

$$\int_{S}\left(\frac{1}{r}\nabla\phi-\phi\nabla\frac{1}{r}\right)\cdot\vec{n}dS+\int_{S_\varepsilon}\left(\frac{1}{r}\nabla\phi-\phi\nabla\frac{1}{r}\right)\cdot\vec{n}dS=0 \tag{5}$$

Using mathematical methods, the value of second integral is $-2\pi\phi(P)$. Then Equation (5) becomes:

$$\phi(P) = \frac{1}{2\pi}\int_S (\frac{1}{r}\nabla\phi - \phi\nabla\frac{1}{r})\cdot\vec{n}dS \tag{6}$$

This equation gives the potential of flow (ϕ) at any point of body surface in terms of $\nabla\phi$ and ϕ on the boundaries of domain. In Equation (6), the first and second terms of the integral can be interpreted as a dipole with strength of ϕ and a source with strength of $\nabla\phi$, respectively. To expand the above equation, as shown in Figure 1, the integration surface S is divided to body surface (S_B), Kutta strip (S_K), and wake surface (S_W). Also, N_B, N_K and N_W are number of panels on body surface, Kutta strip, and wake surface, respectively.

Therefore, Equation (6) can written as below:

$$\phi(P) = \frac{1}{2\pi}\int_{S_B} (\frac{1}{r}\nabla\phi - \phi\nabla\frac{1}{r})\cdot\vec{n}dS + \frac{1}{2\pi}\int_{S_K+S_W} (\frac{1}{r}\nabla\phi - \phi\nabla\frac{1}{r})\cdot\vec{n}dS \tag{7}$$

The thickness of Kutta and wake surfaces are assumed to be zero. Then, $\nabla\phi\cdot\vec{n}$ for these surfaces becomes zero. So:

$$\phi(P) = \frac{1}{2\pi}\int_{S_B} (\frac{1}{r}\nabla\phi - \phi\nabla\frac{1}{r})\cdot\vec{n}dS - \frac{1}{2\pi}\int_{S_K+S_W} \phi\nabla\frac{1}{r}\cdot\vec{n}dS \tag{8}$$

This formulation is equivalent to distributing a source with strength of $\partial\phi/\partial n$ on each panel of the body surface and a doublet with strength of ϕ on each panel of the body surface, Kutta strip and wake surface. For greater simplicity, the strength of doublets on the Kutta strip and wake surface are displayed by μ. The final form of Equation (8) is as follows:

$$\phi(P) = -\frac{1}{2\pi}\int_{S_B} \frac{\vec{n}\cdot\nabla\phi}{r}dS + \frac{1}{2\pi}\int_{S_B} \phi\frac{\vec{n}\cdot\vec{r}}{r^3}dS + \frac{1}{2\pi}\int_{S_K} \mu\frac{\vec{n}\cdot\vec{r}}{r^3}dS + \frac{1}{2\pi}\int_{S_W} \mu\frac{\vec{n}\cdot\vec{r}}{r^3}dS \tag{9}$$

2.1. Boundary Conditions

Applying boundary conditions is one of the most important steps in solving problems by numerical methods. The first boundary condition that is applied is the non-entrance condition. If the propeller assumed to be rigid, the fluid particles cannot enter into the surface and the normal velocity will be zero on the surface of the propeller. If the propeller is operating in a uniform axial flow with velocity of $\vec{V}_\infty$ and rotates with angular velocity of $\vec{\omega}$, as shown in Figure 1, the total velocity of point A on propeller blade is:

$$\vec{v}_A = \vec{V}_\infty + \vec{r}\times\vec{\omega} \tag{10}$$

Then, the non-entrance condition for all panels of body surface is [14]:

$$\left(\nabla\phi\cdot\vec{n}\right)_i = \left(\vec{v}_A\cdot\vec{n}\right)_i i = 1,\ldots,N_B \tag{11}$$

Then, Equation (9) becomes:

$$\phi(P) = -\frac{1}{2\pi}\int_{S_B} \frac{\vec{v}_A\cdot\vec{n}}{r}dS + \frac{1}{2\pi}\int_{S_B} \phi\frac{\vec{n}\cdot\vec{r}}{r^3}dS + \frac{1}{2\pi}\int_{S_K} \mu\frac{\vec{n}\cdot\vec{r}}{r^3}dS + \frac{1}{2\pi}\int_{S_W} \mu\frac{\vec{n}\cdot\vec{r}}{r^3}dS \tag{12}$$

We can rewrite the above equation in series form as follows:

$$\begin{aligned}
&\phi_i + \sum_{\substack{j=1 \\ i \neq j}}^{N_B} A_{ij}\phi_j + \sum_{j=1}^{N_K} A_{ij}\mu_j = \sum_{j=1}^{N_B} B_{ij}\left(\vec{v}_A \cdot \vec{n}\right)_j - \sum_{j=1}^{N_W} A_{ij}\mu_j \qquad i = 1, \ldots, N_B \\
&A_{ij} = -\frac{1}{2\pi} \int_{panel\ j} \frac{\vec{n}\cdot\vec{PQ}}{\left|\vec{PQ}\right|^3} ds \\
&B_{ij} = -\frac{1}{2\pi} \int_{panel\ j} \frac{1}{\left|\vec{PQ}\right|} ds
\end{aligned} \tag{13}$$

where the points P and Q are assumed to be the center of panel i and j, respectively. A_{ij} and B_{ij} are known as influence coefficients and can be calculated according to Delhommeau [15]. The first and second terms in right-hand side of Equation (13) are obtained from non-entrance boundary condition and from previous time step, respectively. Therefore, the unknowns of the above equation are the strength of doublets on body panels and doublets on Kutta strip, hence $N_B + N_K$ unknowns. Another boundary condition that is used to solve this problem is the Kutta condition. This condition for lifting bodies states that the flow should leave trailing edge smoothly and the velocity of flow there be finite [13]. One of the best ways to apply this condition is presented by Morino [16]:

$$\mu_i = (\phi_i)^u - (\phi_i)^l \; i = 1, \ldots, N_K \tag{14}$$

This means that strength of Kutta strip doublets is equal to difference of strength of upper $(\phi)^u$ and lower $(\phi)^l$ doublets. Equation (13) will give N_B equations and N_K equations will be added to system of equations by applying Kutta condition. Finally, by solving this set of $N_B + N_K$ equations, all $N_B + N_K$ unknowns will be obtained.

2.2. Hydrodynamic Forces

After the calculation of velocity potential, the total velocity on each panel can be calculated using numerical differentiation methods. Then, the unsteady Bernoulli's equation was used for calculation of total pressure [17]:

$$\frac{p - p_\infty}{\rho} = -\frac{1}{2}\left|\vec{\nabla}\phi - \vec{v}_A\right|^2 + \frac{1}{2}\left|\vec{v}_A\right|^2 - \frac{\partial\phi}{\partial t} \tag{15}$$

where $\vec{\nabla}\phi$ and $\partial\phi/\partial t$ denote the surface gradient and time derivate of velocity potential. Propeller thrust can be calculated by integration of pressure forces on panels of propeller surface. Also, viscous forces should be obtained by using empirical formulas for surface friction coefficient (C_D) of each panel [18]:

$$C_D = \frac{0.0986}{\left(\log_{10} Re_l - 1.22\right)^2} \tag{16}$$

where Re_l is local Reynolds number based on radial location of panel (x_r) and is Ux_r/v. The viscous drag of each panel is calculated as below [17]:

$$\vec{F}_D = \frac{1}{2}\rho \cdot C_D \cdot \left|\vec{v}_{tot}\right| \vec{v}_{tot} \tag{17}$$

where $\vec{v}_{tot} = \vec{v} + \vec{v}_{ref}$ and $\vec{v}_{ref} = -\vec{v}_A$. Also, $\vec{v}$ is blade surface perturbation velocity and can be obtained by taking surface gradient of velocity potential on blade panels. Then, total force and torque of propeller are obtained as [19]:

$$\begin{aligned} \vec{F} &= \int (p \cdot \vec{n} + \vec{F}_D) dS \\ \vec{M} &= \int \vec{r} \times (p \cdot \vec{n} + \vec{F}_D) dS \end{aligned} \tag{18}$$

Flowchart of panel method for calculation of hydrodynamic coefficient of propeller is shown in Figure 2. Initially, geometry of propeller and panels are generated by a function. A Kutta strip is also created due to geometric considerations, propeller rotation and flow velocity. In the next step, a function calculates the influence coefficients for the sources and doublets. Then, the systems of linear equations of Equation (13) is formed and then solved using iterative methods. By solving the equations, the velocity potential is obtained on the panels of body surface. With numerical derivation of potentials, velocity and pressure and on each panel are calculated and hydrodynamic coefficients of propeller are obtained. This process repeated until the solution converges. In this flowchart, $\vec{v}_m$ is the mean perturbation velocity of the points located on wake and Kutta surface. If these points are located in X_{old} position in time t, new position (X_{new}) of points in time $t + dt$ can be obtained using the following equation:

$$X_{new} = X_{old} + \vec{v}_m \cdot dt \tag{19}$$

where $\vec{v}_m$ is calculated as below [19]:

$$\vec{v}_m = \frac{1}{4\pi} \sum_{S_B} (\vec{n} \cdot \vec{v}_A) \frac{\vec{r}}{r^3} dS + \frac{1}{4\pi} \sum_{S_B} \phi \frac{\vec{dl} \times \vec{r}}{r^3} + \frac{1}{4\pi} \sum_{S_W + S_K} \mu \frac{\vec{dl} \times \vec{r}}{r^3} \tag{20}$$

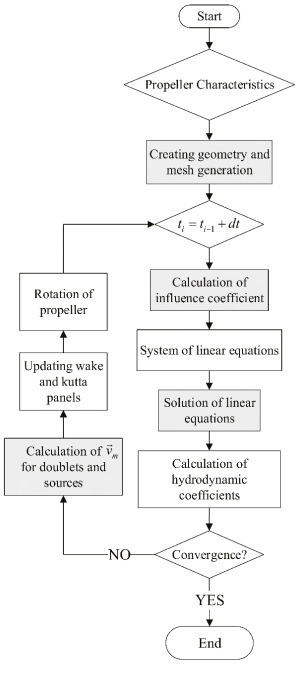

Figure 2. Flowchart of panel method.

3. Validation of Results of Panel Method

One of the most common propellers that has been used for the validation of numerical methods is the DTMB 4119 propeller. This propeller is shown in Figure 3. Also, the main particulars and details of geometry are given in Tables 1 and 2, respectively.

Figure 3. DTMB 4119 propeller.

Table 1. Main Particulars of DTMB 4119 Propeller [20].

Number of Blades	3
Diameter	0.20 m
Blade Sections Profile	NACA 66 modified (a = 0.8)
Design Advance Ratio (*J*)	0.833

Table 2. Geometry of DTMB 4119 Propeller [20].

r/R	c/D	P/D	Skew	Rake	t_{max}/c	f_{max}/c
0.2	0.3200	1.1050	0	0	0.2055	0.0143
0.3	0.3635	1.1022	0	0	0.1553	0.0232
0.4	0.4048	1.0983	0	0	0.1180	0.023
0.5	0.4392	1.0932	0	0	0.0916	0.0218
0.6	0.4610	1.0879	0	0	0.0696	0.0207
0.7	0.4622	1.0839	0	0	0.0542	0.0200
0.8	0.4347	1.0811	0	0	0.0421	0.0197
0.9	0.3613	1.0785	0	0	0.0332	0.0182
0.95	0.2775	1.0770	0	0	0.0323	0.0163
1	0.0800	1.0750	0	0	0.0316	0.0118

P is propeller pitch, r is radius of each section, R is propeller radius, c is chord of each section, D is propeller diameter, t_{max} is Maximum thickness of each section and f_{max} is maximum camber. For the validation of the results of numerical modeling for hydrodynamics and noise of DTMB 4119 propeller, some experiments were carried out with a model propeller in a cavitation tunnel of the Marine Engineering Laboratory of Sharif University of Technology (Figure 4). For measuring the thrust and torque of propeller model, a H29 dynamometer has been used in this tunnel.

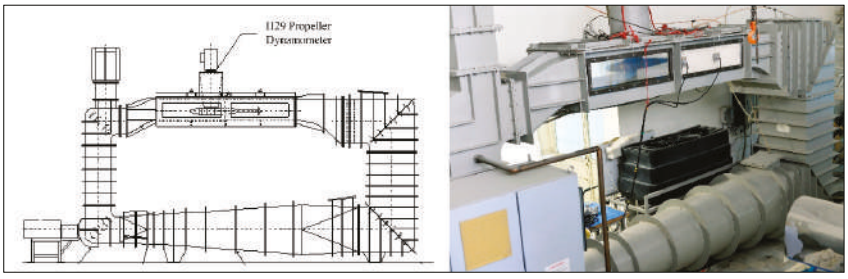

Figure 4. Cavitation Tunnel of Sharif University of Technology.

The developed code can also create the geometry of the propeller and generate mesh for it. For this purpose, the profile of propeller blades, the number of blades, the rake and skew angle and the desired grid size should be specified as input. In the panel method, it is not common to specify mesh dimensions. Because of the cosine spacing of panels in chordwise and spanwise directions, the exact size of panels cannot be specified. Grid size is shown as $m \times n$ which m and n are number of elements in chordwise and spanwise, respectively. For optimization of the grid size, thrust coefficient for design advance ratio ($J = 0.833$) is calculated for some different grids, and error of numerical results compared with experimental results for each grid size are presented in Table 3 and Figure 5. All simulations are carried out using Intel Core i7 2.6 GHz and 8 GB of RAM. Also, the CPU times for the panel method are given in Table 3.

Table 3. CPU Time and error for different grids ($J = 0.833$).

Grid	Numerical Result	Experimental Result	Error (%)	CPU Time (sec.)
10×10	0.128	0.15	14.6	242
10×15	0.132		12	521
20×20	0.144		4	1224
30×30	0.146		2.6	2545

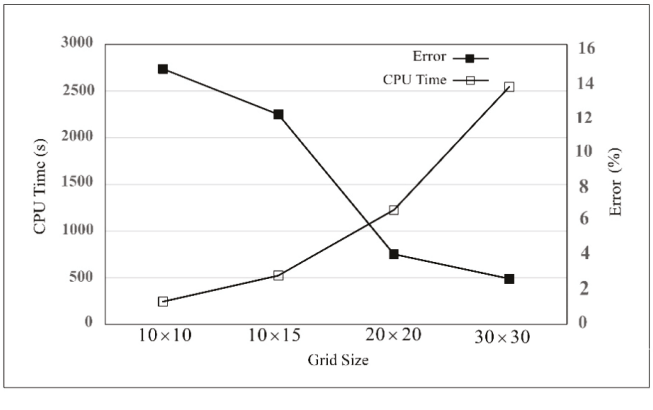

Figure 5. CPU Time and error for different grids ($J = 0.833$).

It can be seen from Figure 5 that the grid size of 20×20 compared to other grids has more appropriate CPU time and error, and then the grid is used to simulate propeller. After simulation of flow around DTMB 4119 propeller, wake surface and hydrodynamic coefficients of propeller (Thrust, torque and efficiency) are obtained. In Figure 6, the wake surface of the propeller is shown for different advance ratios.

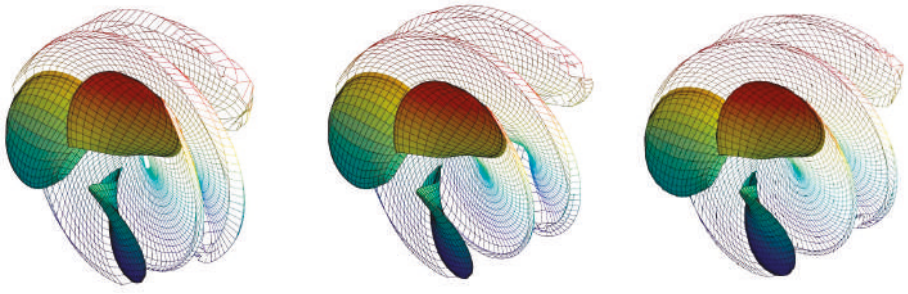

Figure 6. Wake surface of propeller for different advance ratios.

As shown in Figure 6, in low advance ratios which ship speed is low and propeller load is high (heavy duty conditions of propeller), disks of wake surface are closer together and wake rollup is intense but in higher advance ratios, disks of wake surface are more spacious and rollup is very low. Numerical simulation of propeller is performed by developed code for various advance ratios and Figure 7 compares the hydrodynamic coefficients of the propeller obtained by the panel method with experimental data.

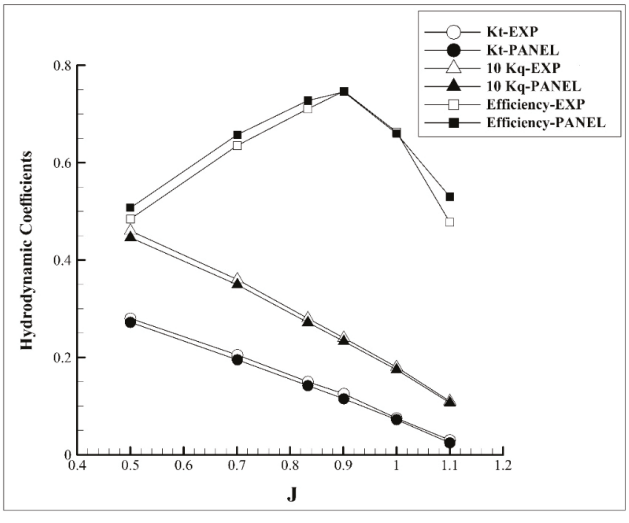

Figure 7. Hydrodynamic coefficients of DTMB 4119 propeller.

The pressure distribution in the advance ratio of $J = 0.833$ for different radial sections of the propeller blade is compared with experimental measurements [21] in Figure 8.

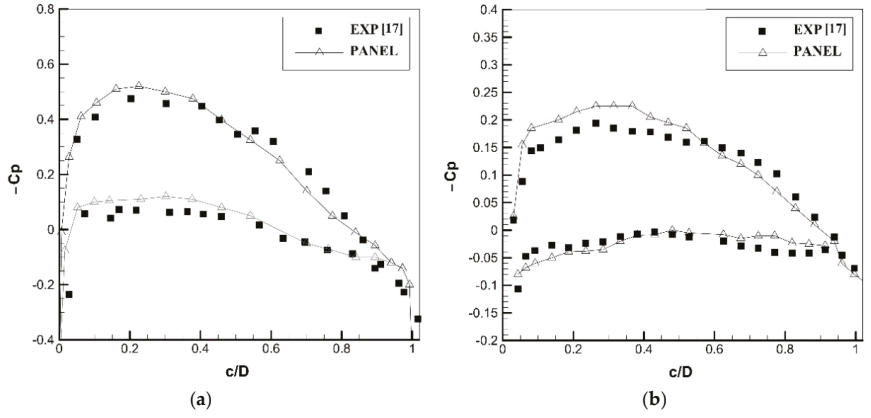

Figure 8. Experimental and panel method results for pressure distribution at (**a**) r/R = 0.3 and (**b**) r/R = 0.7.

According to Figure 7, there is satisfactory agreement between the hydrodynamic coefficients obtained from the panel method and experimental results. The maximum error of the trust coefficient calculated by the panel method is about 4% and for torque coefficient is about 7%. As can be seen in Figure 8, pressure distribution obtained from the panel method is in good agreement with the experimental data. This shows that the accuracy of the panel method results is acceptable. One reason for the greater error of the torque coefficient is the use of empirical formulas in the calculation of the friction resistance of each panel. According to the above results, the panel method can be used for hydrodynamic performance analysis of marine propellers.

4. Acoustic Formulations

In most acoustic problems, rigid bodies located in the fluid flow have very important effects on the generated noise. For this reason, Williams and Hawkings [22] in 1969 developed the Lighthill equations [23] with the assumption of rigid bodies. The equations presented by these researchers in acoustic science are known as the FW-H model. For solving the FW-H equation, Farassat et al. [24] presented a method that can predict the generated noise of moving object with arbitrary geometry. According to this formulation, total sound pressure can (p') expressed as below [24]:

$$p'\left(\vec{x},t\right) = {p'}_T\left(\vec{x},t\right) + {p'}_L\left(\vec{x},t\right) \tag{21}$$

where ${p'}_T$ and ${p'}_L$ denote the thickness and loading pressure, respectively. Thickness pressure is due to the fluid displacement caused by movement of the body within the fluid and classified as monopole noise source. Another phenomenon caused by the motion of the non-symmetric body in fluid is the distribution of positive and negative pressure on the face and back of the body. In fact, this pressure distribution is the main source of trust force in propellers. Pressure difference on both sides of the body create a dipole noise source which is referred as loading pressure. This solution is obtained with assumption of low Mach number, and hence the quadrupole noise can be neglected. These components are calculated through the following relations [24]:

$$\begin{aligned} 4\pi {p'}_T\left(\vec{x},t\right) &= \int_S \left[\frac{\rho\left(\dot{v}_n + \dot{v}_{\dot{n}}\right)}{r\left(1-M_r\right)^2}\right]_{ret} dS + \int_S \left[\frac{\rho v_n\left(r\dot{M}_r + cM_r - cM^2\right)}{r^2\left(1-M_r\right)^3}\right]_{ret} dS \\ 4\pi {p'}_L\left(\vec{x},t\right) &= \frac{1}{c}\int_S \left[\frac{\dot{L}_r}{r\left(1-M_r\right)^2}\right]_{ret} dS + \frac{1}{c}\int_S \left[\frac{L_r - L_M}{r^2\left(1-M_r\right)^2}\right]_{ret} dS \\ &\quad + \frac{1}{c}\int_S \left[\frac{L_r\left(r\dot{M}_r + cM_r - cM^2\right)}{r^2\left(1-M_r\right)^3}\right]_{ret} dS \end{aligned} \tag{22}$$

where ρ is fluid density in kg/m^3, c is sound speed in m/s, $\vec{v}$ is the noise source velocity in m/s, $\vec{r}$ is distance vector from noise source to receiver in m, r is magnitude of $\vec{r}$ in m, Mach number is $\vec{M} = \vec{v}/c$, $L = p \cdot \vec{n}$ is pressure force in N and p is hydrodynamic pressure in Pa. The dot over variables means time derivate of the variable. The *ret* subscript in this equation means that the calculations must be done using values at the retarded time.

In the first step of noise calculation, the flow around the body is simulated using the panel method and flow quantities such as pressure and velocity are obtained for panels on the body surface. Then, for receiver in position of $\vec{x}$ and time of t_i, retarded time $(\tau_{i,j})$ is obtained for panel j. After this step, all quantities required in Equation (20) must be calculated for each panel at the retarded time, numerical integrals of the equation are solved for each panel, and the acoustic pressure of each element is obtained. By summing up the acoustic pressures of all the elements, a total acoustic pressure is obtained for the specified receiver. Flowchart of noise calculation using FW-H equations is shown in Figure 9.

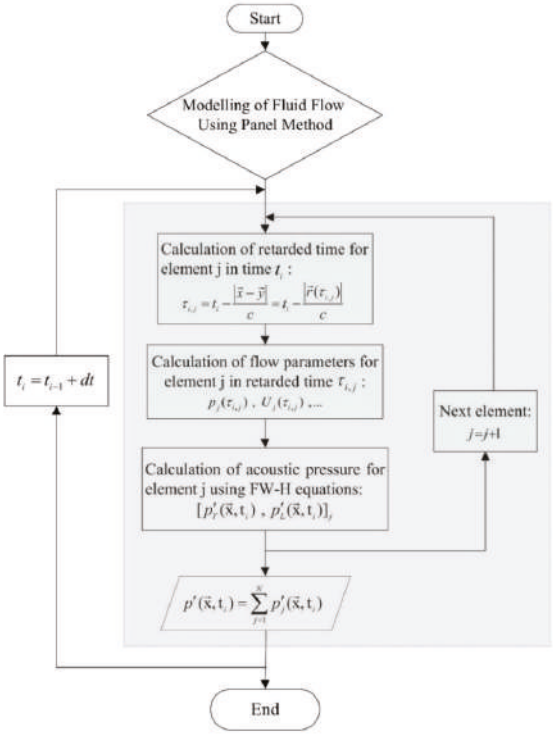

Figure 9. Flowchart of noise calculation using FW-H equations.

5. Noise of DTMB 4119 Propeller

The noise generated by the propeller is one of the most important components of the vessels noise [6]. Therefore, measuring and calculating the propeller noise is one of the interesting research subjects in naval engineering. In the first step, the results of the developed FW-H code for noise calculation should validated using experimental results obtained in cavitation tunnel. For measuring the noise of propeller, a TC4042 hydrophone has been used in cavitation tunnel of Sharif University of Technology. The arrangement of this validation hydrophone is shown in Figure 10. Also, the location of this hydrophone is given in Figure 11.

Figure 10. Arrangement of TC4042 hydrophone on cavitation tunnel.

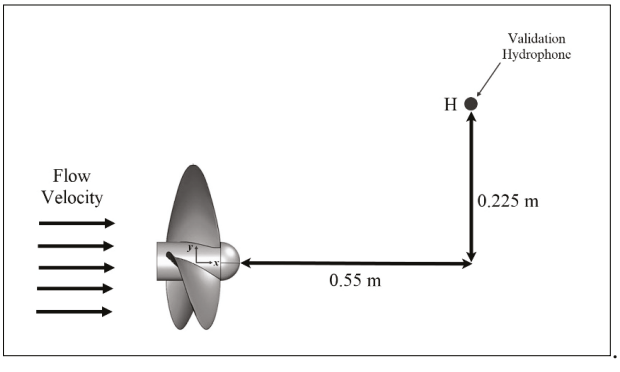

Figure 11. Location of validation hydrophone.

For validation of results of FW-H code, noise measurements done in cavitation tunnel under below conditions:

- Flow velocity: 2.2 m/s
- Propeller RPM: 792
- Advance ratio (J): 0.833

The time history of acoustic pressure as measured by validation hydrophone is shown in Figure 12.

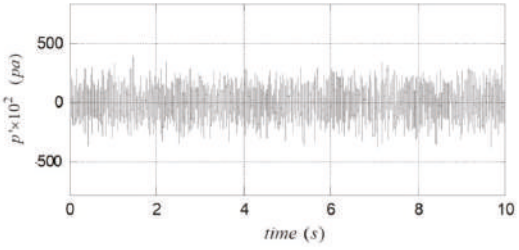

Figure 12. Time history of acoustic pressure measured by validation hydrophone.

In the post-processing stage, acoustic pressure from time domain in transferred to frequency domain by using the fast Fourier transform (FFT) and the sound pressure level is calculated using the following formula [25]:

$$SPL\left(\vec{x},t\right) = 20\log_{10}\left(p'/p_{ref}\right) \tag{23}$$

where p_{ref} is the reference pressure and related to threshold of a normal human hearing for frequency of 1 kHz which for water is 1 μPa [26]. The numerical results of noise obtained by own developed code compared by experimental results in Figure 13. Propeller and flow conditions are the same as the experimental setup.

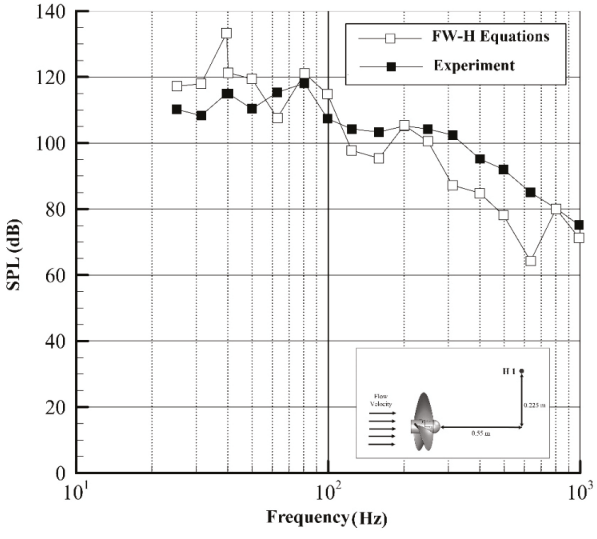

Figure 13. Validation of FW-H code results.

It can be seen that there is good agreement between the numerical and experimental results of propeller noise, especially in frequencies under 250 Hz. It seems that main sources of error of numerical results are:

- Error of panel method code for calculation of pressure and flow velocity: As mentioned in the previous sections, the results of the thrust and torque of the panel method have 4% and 7% error in comparison with the experimental results. Since the FW-H equations use panel method outputs, the above error causes an error in calculating the noise of the impeller.
- The error of FW-H code for noise calculation: FW-H equations include some integrals that are calculated numerically on the source of noise. Therefore, the numerical calculation error of these

equations can cause error in the value of noise. Also, in the solution presented in this study, the quadrupole sources of noise are neglected, which could cause a slight error in the value of propeller noise.

- The reflection of sound inside the cavitation tunnel is another reason for the difference between the experimental and numerical results. The restricted space of the cavitation tunnel causes the reverberation of sound emitted by the propeller, which results in an error in the measured noise values. For investigating the effects of sound reverberation on noise data, special equipment is needed which is not available in our laboratory.

Seol et al. [27] and Yang et al. [28] carried out some numerical studies on DTMB 4119 propeller, but since the specifications of the propeller used are not the same as the propeller model in our laboratory, the results cannot be compared.

By looking more precisely into results, it founds that both experimental and numerical results have peaks in some frequencies. It seems that these are Blade Passing Frequencies (*BPF*) of propeller. For the propeller, the rate at which the blades pass by a fixed position is called the *BPF*. This frequency is known as the blade passing frequency (*BPF*) of the blade. As regards the propeller, the *BPF* and its higher harmonics can be calculated as:

$$BPF = Z \times rps \times h \ (\mathrm{Hz}) \tag{24}$$

where Z is number of propeller blades, *rps* is the frequency of propeller rotation in Hz and h is no of harmonic. When receiver is located in an asymmetric location relative to blades, the noise of propeller in BPFs will have local peaks in comparison to other frequencies. For the receiver, which is located in the hub plane of the propeller, at an equal and constant distance from the blades at all times, *BPF* could not be seen in the SPL diagram. For noise diagrams in Figure 13, *rps* is 13.2 and Z is 3. Therefore, BPF for three first harmonics of propeller is about 39.6, 79.2 and 118.8 Hz and noise results have peaks in the first two frequencies.

After the validation of FW-H code, propeller noise calculations were made for four hydrophones (receivers). Two hydrophones located in the propeller rotation plane and two hydrophones located in front of propeller hub. The location of hydrophones and their coordinates are given in Figure 14 and Table 4.

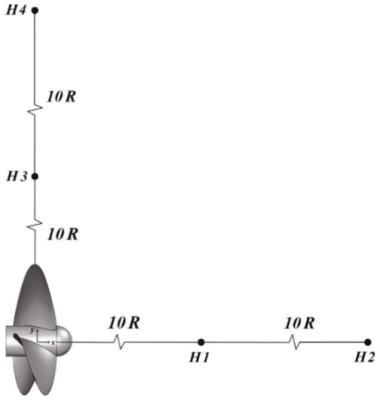

Figure 14. Location of hydrophones.

Table 4. Coordinates of hydrophones.

	X(m)	*Y(m)*	*Z(m)*
H1	1	0	0
H2	2	0	0
H3	0	1	0
H4	0	2	0

The noise of the propeller as calculated by the FW-H code for hydrophones H1 and H2 are presented in Figure 15. Noise predictions were made at a flow speed of 2.2 m/s and RPM of 792 where $J = 0.833$.

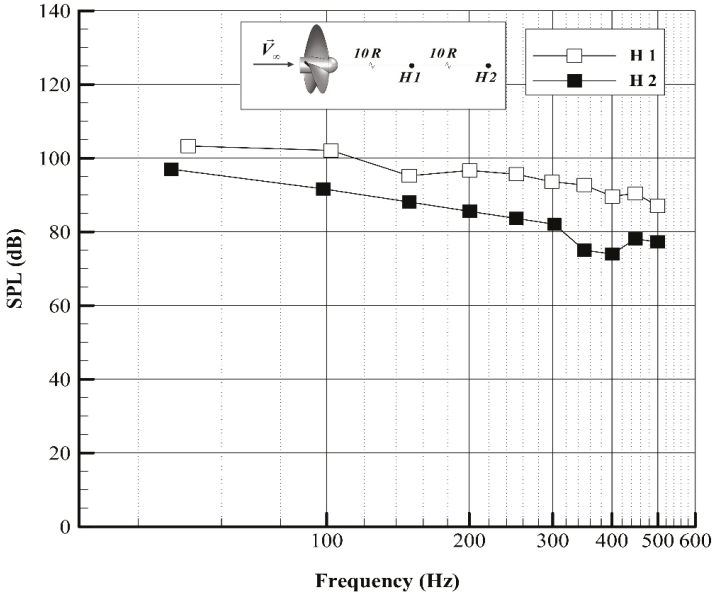

Figure 15. Sound pressure level of propeller in hydrophones H1 and H2.

Results shown in Figure 15 reveals that by increasing the distance of hydrophone from propeller, noise of H2 decreased significantly in comparison with H1. Also, in Figure 16, the propeller noise in hydrophones H3 and H4 are presented.

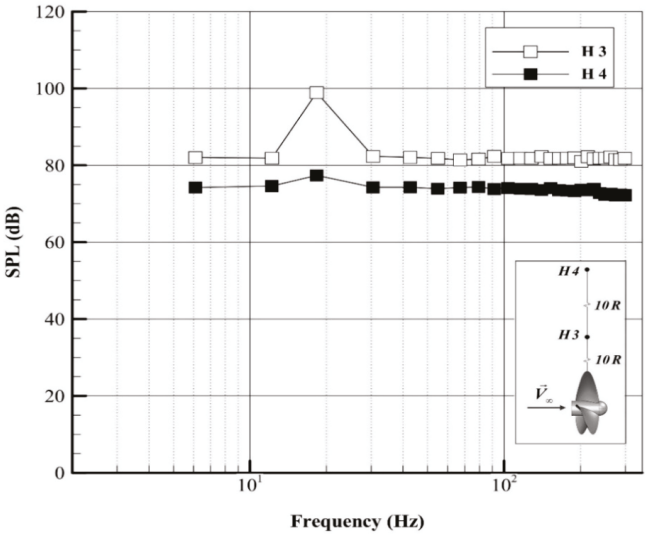

Figure 16. Sound pressure level of propeller in hydrophones H3 and H4.

As can be seen in Figure 16, with an increase of distance from the propeller, noise decreased significantly. Also, in both hydrophones, at a blade passing frequency of 18.22 Hz, the noise has a peak value which is also indicated in the Figure 16. By comparing Figures 15 and 16, it can be seen that the SPL in front of the propeller hub is higher than the SPL in the propeller rotational plane.

6. Conclusions

Measuring and calculating the noise of marine propellers is very important. In this research, the combination of the panel method and FW-H equations has been used to calculate the non-cavitating noise of marine propellers. In the first step, a numerical panel method code is developed to solve the flow around the propeller and calculate the propeller hydrodynamic coefficients. The results of this code in comparison with the experimental results had maximum error of 4% and 7% for thrust and torque coefficients, respectively.

Then, a noise calculation code based on FW-H acoustic equations was developed, which uses the outputs of the panel method code as inputs and calculates the noise of the propeller for the desired receiver. The results of this code are in good agreement with the noise of the propeller obtained using results from a test carried out in cavitation tunnel of Sharif University. Using this code, the propeller noise is measured for four hydrophones with different distances and orientations. With increasing distance from the propeller, the noise of the propeller has been significantly reduced. For the hydrophones located on the rotation plane of the propeller, as predicted by theory and experiments on propeller noise, the maximum noise has occurred at the blade passing frequency. The results show that the SPL in front of the propeller hub is higher than SPL in the propeller rotational plane.

According to the above results, the combination of the panel method and FW-H equations can be used for hydrodynamic and acoustic analysis of marine propellers.

Author Contributions: All authors contributed equally in this work.

Funding: This research received no external funding.

Conflicts of Interest: The authors declare no conflict of interest.

References

1. Hess, J.L.; Smith, A.M.O. *Calculation of Nonlifting Potential Flow about Arbitrary Three-Dimensional Bodies*; Douglas Aircraft Co.: Long Beach, CA, USA, 1962.
2. Hess, J.L. *Calculation of Potential Flow about Arbitrary Three-Dimensional Lifting Bodies*; Douglas Aircraft Co.: Long Beach, CA, USA, 1972.
3. Hess, J.; Valarezo, W. Calculation of steady flow about propellers by means of a surface panel method. *J. Propuls. Power* **1985**, *1*, 470–476. [CrossRef]
4. Baltazar, J.M.R.D.C.; De Campos, J.A.C.F. An iteratively coupled solution of the cavitating flow on marine propellers using BEM. *J. Hydrodyn.* **2010**, *22*, 796–801. [CrossRef]
5. Gaggero, S.; Villa, D.; Brizzolara, S. RANS and PANEL method for unsteady flow propeller analysis. *J. Hydrodyn.* **2010**, *22*, 547–552. [CrossRef]
6. Ebrahimi, A.; Razaghian, A.; Seif, M.; Zahedi, F.; Nouri-Borujerdi, A. A comprehensive study on noise reduction methods of marine propellers and design procedures. *Appl. Acoust.* **2019**, *150*, 55–69. [CrossRef]
7. Seol, H.; Park, C. Numerical and Experimental Study on the Marine Propeller Noise. In Proceedings of the 19th International Congress on Acoustics, Madrid, Spain, 2–7 September 2007; pp. 2–7.
8. Kellett, P.; Turan, O.; Incecik, A. A study of numerical ship underwater noise prediction. *Ocean Eng.* **2013**, *66*, 113–120. [CrossRef]
9. Bagheri, M.; Seif, M.; Mehdigholi, H. Numerical Simulation of underwater propeller noise. *J. Ocean Mech. Aerosp.* **2014**, *4*, 4–9.
10. Testa, C.; Ianniello, S.; Salvatore, F. A Ffowcs Williams and Hawkings formulation for hydroacoustic analysis of propeller sheet cavitation. *J. Sound Vib.* **2018**, *413*, 421–441. [CrossRef]
11. Gorji, M.; Ghassemi, H.; Mohamadi, J. Calculation of sound pressure level of marine propeller in low frequency. *J. Low Freq. Noise Vib. Act. Control.* **2018**, *37*, 60–73. [CrossRef]
12. Bagheri, M.R.; Seif, M.S.; Mehdigholi, H.; Yaakob, O. Analysis of noise behaviour for marine propellers under cavitating and non-cavitating conditions. *Ships Offshore Struct.* **2017**, *12*, 1–8. [CrossRef]
13. Katz, J.; Plotkin, A. *Low-Speed Aerodynamics*; Cambridge University Press: Cambridge, UK, 2001.
14. Politis, G. Unsteady Wake Rollup Modeling Using a Mollifier Based Filtering Technique. *Dev. Appl. Ocean. Eng.* **2016**, *5*, 1. [CrossRef]
15. Delhommeau, G. Amélioration des performances des codes de calcul de diffraction-radiation au premier ordre. In Proceedings of the 2nd Journées de l'Hydrodynamique, Nantes, France, 13–15 February 1989.
16. Morino, L.; Kuo, C. Subsonic potential aerodynamics for complex configurations: A general theory. *AIAA J.* **1974**, *12*, 191–197.
17. Politis, G.K. Unsteady Rollup Modeling for Wake-Adapted Propellers Using a Time-Stepping Method. *J. Ship Res.* **2005**, *49*, 216–231.
18. Blevins, R.D. *Applied Fluid Dynamics Handbook*; Van Nostrand Reinhold Co.: New York, NY, USA, 1984; p. 568.
19. Najafi, S.; Abbaspoor, M. Numerical investigation of flow pattern and hydrodynamic forces of submerged marine propellers using unsteady boundary element method. *Proc. Inst. Mech. Eng. Part M J. Eng. Marit. Environ.* **2017**, *233*, 67–79. [CrossRef]
20. Boumediene, K.; Belhenniche, S. Numerical Analysis of the Turbulent Flow around DTMB 4119 Marine Propeller. *Int. J. Mech. Aerosp. Ind. Mechatron. Manuf. Eng.* **2016**, *10*, 347–351.
21. Jessup, S. An Experimental Investigation of Viscous Aspects of Propeller Blade Flow. Ph.D. Thesis, The Catholic University of America, Washington, DC, USA, 1989.
22. Williams, J.E.F.; Hawkings, D.L. Sound Generation by Turbulence and Surfaces in Arbitrary Motion. *Philos. Trans. R. Soc. A Math. Phys. Eng. Sci.* **1969**, *264*, 321–342. [CrossRef]
23. Lighthill, M.J. On sound generated aerodynamically II. Turbulence as a source of sound. *Proc. R. Soc. Lond. Ser. A. Math. Phys. Sci.* **1954**, *222*, 1–32.
24. Farassat, F. *Derivation of Formulations 1 and 1A of Farassat*; NASA Langley Research Center: Hampton, VA, USA, 2007.
25. Kinsler, L.A.; Frey, A.R.; Coppens, A.B.; Sanders, J.V. *Fundamentals of Acoustics*; John Wiley & Sons: New York, NY, USA, 2000.
26. Council, N.R. *Low-Frequency Sound and Marine Mammals: Current Knowledge and Research Needs*; National Academies Press: Washington, DC, USA, 1994.

27. Seol, H.; Suh, J.-C.; Lee, S. Development of hybrid method for the prediction of underwater propeller noise. *J. Sound Vib.* **2005**, *288*, 345–360. [CrossRef]
28. Yang, Q.; Wang, Y.; Zhang, M. Calculation of propeller's load noise using LES and BEM numerical acoustics coupling methods. *WIT Trans. Model. Simul. Bound. Elem. Other Reduct. Methods XXXIII* **2011**, *52*, 85–97.

Mathematical and Computational Applications

MDPI

Article

Natural Frequency Analysis of Functionally Graded Orthotropic Cross-Ply Plates Based on the Finite Element Method

Michele Bacciocchi [1,2,*] and Angelo Marcello Tarantino [3]

1 DICAM Department, University of Bologna, Viale del Risorgimento, 2, 40136 Bologna BO, Italy
2 DESD Department, University of San Marino, Via Consiglio dei Sessanta, 99, 47891 Repubblica Di San Marino, San Marino
3 DIEF Department, University of Modena and Reggio Emilia, Via Vivarelli, 10, 41125 Modena MO, Italy; angelomarcello.tarantino@unimore.it
* Correspondence: michele.bacciocchi@unibo.it or michele.bacciocchi@unirsm.sm; Tel.: +39-051-209-3494

Received: 30 April 2019; Accepted: 17 May 2019; Published: 19 May 2019

Abstract: This paper aims to present a finite element (FE) formulation for the study of the natural frequencies of functionally graded orthotropic laminated plates characterized by cross-ply layups. A nine-node Lagrange element is considered for this purpose. The main novelty of the research is the modelling of the reinforcing fibers of the orthotropic layers assuming a non-uniform distribution in the thickness direction. The Halpin–Tsai approach is employed to define the overall mechanical properties of the composite layers starting from the features of the two constituents (fiber and epoxy resin). Several functions are introduced to describe the dependency on the thickness coordinate of their volume fraction. The analyses are carried out in the theoretical framework provided by the first-order shear deformation theory (FSDT) for laminated thick plates. Nevertheless, the same approach is used to deal with the vibration analysis of thin plates, neglecting the shear stiffness of the structure. This objective is achieved by properly choosing the value of the shear correction factor, without any modification in the formulation. The results prove that the dynamic response of thin and thick plates, in terms of natural frequencies and mode shapes, is affected by the non-uniform placement of the fibers along the thickness direction.

Keywords: finite element modelling; laminated composite plates; non-uniform mechanical properties

1. Introduction

The finite element (FE) method currently represents the most-utilized computational approach to solve several engineering problems and in applications whose solutions cannot be obtained analytically [1]. The technological advancements in computer sciences have allowed a fast and easy diffusion of this technique, especially in terms of structural mechanics problems. The key to the success of the FE method lies in the reduction of complex problems into simpler ones in which the reference domain is made of several discrete elements, and in its easy computational implementation. This idea was first highlighted by Duncan and Collar [2,3], and successively emphasized by Hrennikoff [4], Courant [5], Clough [6], and Melosh [7].

The approximate solutions that can be obtained by means of the FE approach are accurate and representative of the physical problem under consideration [8,9]. To the best of the authors' knowledge, the progression and development of this technique are well-described in many pertinent books, such as the ones by Oden [10], Oden and Reddy [11], Hinton [12], Zienkiewicz [13], Reddy [14], Onate [15], Hughes [16], and Ferreira [17]. These books should be used as references for the theoretical background of the numerical approach at issue. For completeness purposes, it should be recalled that various and

alternative approaches have been developed in past decades to obtain approximated but accurate solutions to several complex structural problems, not only based on the FE method [18–21].

An intriguing application that is efficiently solved by means of the FE methodology is about the structural response of plates and panels made of composite materials [22–24]. With respect to an isotropic and conventional medium, a composite material can reach superior performance by combining two (or more) constituents. A typical example of this category are fiber-reinforced composites, in which the high-strength fibers are the main load-carrying elements, whereas the matrix has the task of keeping them together and protecting the reinforcing phase from the environment [25–28]. In general, a micromechanical approach should be employed to evaluate the overall mechanical properties of these materials, starting from the features of the single constituents. The review paper by Chamis and Sendeckyj represents a fundamental contribution is this direction [29]. One of the most effective approaches that can be used toward this aim is the one proposed by Halpin [30] and Tsai [31,32], who developed a semi-empirical method and expressed the mechanical properties of the constituents in terms of Hill's elastic moduli [33,34]. Further details concerning the micromechanics of fiber-reinforced composite materials can be found in [35].

The use of a versatile numerical method also allows us to investigate the structural response of composite structures with non-uniform mechanical properties. In particular, in the present paper the reinforcing fibers are characterized by a gradual variation of their volume fraction along the plate thickness, following the same idea of functionally graded materials [36–52]. With respect to this class of materials, in which the composites turn out to be isotropic, the layers of the plate assume orthotropic features and can also be oriented. This topic clearly falls within the aim of the optimal design of composite structures [53–58]. It should be mentioned that a similar approach is followed in the design of functionally graded carbon-nanotube-reinforced composites, due to the advancements in nanostructures and nanotechnologies [59–68].

In this paper, the research is organized in two main sections. After this brief introduction, the FE formulation for laminated thick and thin plates is presented in Section 2. Here, the theoretical framework is based on the well-known first-order shear deformation theory (FSDT) for laminated composite structures [69,70]. The effect of the shear correction factor is also discussed in order to deal with thin plates [71]. In addition, the micromechanics approach based on the Halpin–Tsai model is described in detail, by also introducing the topic of variable mechanical properties. Section 3 presents the results of the numerical applications. As a preliminary test, the accuracy and convergence features of the numerical approach are discussed by means of the comparison with the semi-analytical solutions available in the literature for thin and thick laminated composite plates. Then, the natural frequencies of functionally graded orthotropic cross-ply plates are presented for several mechanical configurations. Finally, Appendix A is added to define the terms of the fundamental operators of the proposed FE formulation.

2. Finite Element (FE) Formulation for Laminated Thick and Thin Plates

The theoretical framework of the current research is based on the first-order shear deformation theory (FSDT). The governing equations are presented in this section by developing the corresponding FE formulation. The following kinematic model is assumed within each discrete element of the plate [69]:

$$\begin{array}{l} U_x^{(e)}(x,y,z,t) = u_x^{(e)}(x,y,t) + z\phi_x^{(e)}(x,y,t) \\ U_y^{(e)}(x,y,z,t) = u_y^{(e)}(x,y,t) + z\phi_y^{(e)}(x,y,t) \\ U_z^{(e)}(x,y,z,t) = u_z^{(e)}(x,y,t) \end{array} , \tag{1}$$

where $U_x^{(e)}, U_y^{(e)}, U_z^{(e)}$ are the three-dimensional displacements of the structure, whereas the degrees of freedom of the problem are given by three translations $u_x^{(e)}, u_y^{(e)}, u_z^{(e)}$ and two rotations $\phi_x^{(e)}, \phi_y^{(e)}$ defined

on the plate middle surface. These quantities can be conveniently collected in the corresponding vector $\mathbf{u}^{(e)}$, defined below

$$\mathbf{u}^{(e)} = \begin{bmatrix} u_x^{(e)} & u_y^{(e)} & u_z^{(e)} & \phi_x^{(e)} & \phi_y^{(e)} \end{bmatrix}^T. \tag{2}$$

The coordinates x, y, z specify the local reference system of the plate and t is the time variable. The superscript (e) clearly specifies that this model is valid for each element. The geometry of the plate is fully described once the lengths L_x, L_y of its sides and its overall thickness h are defined. It should be recalled that for a laminate structure one gets

$$h = \sum_{k=1}^{N_L} (z_{k+1} - z_k), \tag{3}$$

in which z_{k+1}, z_k stand for the upper and lower coordinates of the k-th layer, respectively. The degrees of the freedom (2) are approximated in each element by means of quadratic Lagrange interpolation functions. As can be noted from Figure 1, nine nodes are introduced in each subdomain. As a consequence, the degrees of freedom assume the following aspect:

$$\begin{aligned}
u_x^{(e)}(x,y,t) &= \sum_{i=1}^{9} N_i(x,y) u_{x,i}^{(e)}(t) = \overline{\mathbf{N}} \mathbf{u}_x^{(e)} \\
u_y^{(e)}(x,y,t) &= \sum_{i=1}^{9} N_i(x,y) u_{y,i}^{(e)}(t) = \overline{\mathbf{N}} \mathbf{u}_y^{(e)} \\
u_z^{(e)}(x,y,t) &= \sum_{i=1}^{9} N_i(x,y) u_{z,i}^{(e)}(t) = \overline{\mathbf{N}} \mathbf{u}_z^{(e)} \\
\phi_x^{(e)}(x,y,t) &= \sum_{i=1}^{9} N_i(x,y) \phi_{x,i}^{(e)}(t) = \overline{\mathbf{N}} \boldsymbol{\phi}_x^{(e)} \\
\phi_y^{(e)}(x,y,t) &= \sum_{i=1}^{9} N_i(x,y) \phi_{y,i}^{(e)}(t) = \overline{\mathbf{N}} \boldsymbol{\phi}_y^{(e)}
\end{aligned}, \tag{4}$$

where N_i represents the i-th shape function, whereas $u_{x,i}^{(e)}, u_{y,i}^{(e)}, u_{z,i}^{(e)}, \phi_{x,i}^{(e)}, \phi_{y,i}^{(e)}$ denote the nodal displacements, which can be included in the corresponding vectors

$$\begin{aligned}
\mathbf{u}_x^{(e)} &= \begin{bmatrix} u_{x,1}^{(e)} & \cdots & u_{x,9}^{(e)} \end{bmatrix}^T, \mathbf{u}_y^{(e)} = \begin{bmatrix} u_{y,1}^{(e)} & \cdots & u_{y,9}^{(e)} \end{bmatrix}^T, \mathbf{u}_z^{(e)} = \begin{bmatrix} u_{z,1}^{(e)} & \cdots & u_{z,9}^{(e)} \end{bmatrix}^T \\
\boldsymbol{\phi}_x^{(e)} &= \begin{bmatrix} \phi_{x,1}^{(e)} & \cdots & \phi_{x,9}^{(e)} \end{bmatrix}^T, \boldsymbol{\phi}_y^{(e)} = \begin{bmatrix} \phi_{y,1}^{(e)} & \cdots & \phi_{y,9}^{(e)} \end{bmatrix}^T
\end{aligned}. \tag{5}$$

On the other hand, the shape functions linked to the nine nodes of the finite element are included in the vector $\overline{\mathbf{N}}$, defined below:

$$\overline{\mathbf{N}} = \begin{bmatrix} N_1 & \cdots & N_9 \end{bmatrix}. \tag{6}$$

For the sake of clarity, it should be recalled that the nodes are identified in each element by following the numbering specified in Figure 1.

At this point, the nodal degrees of freedom can be collected in a sole vector $\overline{\mathbf{u}}^{(e)}$ to simplify the nomenclature:

$$\begin{aligned}
\overline{\mathbf{u}}^{(e)} &= \begin{bmatrix} \mathbf{u}_x^{(e)} & \mathbf{u}_y^{(e)} & \mathbf{u}_z^{(e)} & \boldsymbol{\phi}_x^{(e)} & \boldsymbol{\phi}_y^{(e)} \end{bmatrix}^T \\
&= \begin{bmatrix} u_{x,1}^{(e)} & \cdots & u_{x,9}^{(e)} & u_{y,1}^{(e)} & \cdots & u_{y,9}^{(e)} & u_{z,1}^{(e)} & \cdots & u_{z,9}^{(e)} & \phi_{x,1}^{(e)} & \cdots & \phi_{x,9}^{(e)} & \phi_{y,1}^{(e)} & \cdots & \phi_{y,9}^{(e)} \end{bmatrix}^T
\end{aligned}, \tag{7}$$

and to write the definitions (4) by using the following matrix notation:

$$\begin{bmatrix} u_x^{(e)} \\ u_y^{(e)} \\ u_z^{(e)} \\ \phi_x^{(e)} \\ \phi_y^{(e)} \end{bmatrix} = \begin{bmatrix} \overline{\mathbf{N}} & 0 & 0 & 0 & 0 \\ 0 & \overline{\mathbf{N}} & 0 & 0 & 0 \\ 0 & 0 & \overline{\mathbf{N}} & 0 & 0 \\ 0 & 0 & 0 & \overline{\mathbf{N}} & 0 \\ 0 & 0 & 0 & 0 & \overline{\mathbf{N}} \end{bmatrix} \begin{bmatrix} \mathbf{u}_x^{(e)} \\ \mathbf{u}_y^{(e)} \\ \mathbf{u}_z^{(e)} \\ \boldsymbol{\Phi}_x^{(e)} \\ \boldsymbol{\Phi}_y^{(e)} \end{bmatrix} \Leftrightarrow \underset{5\times 1}{\mathbf{u}^{(e)}} = \underset{5\times(9\times 5)}{\mathbf{N}} \underset{(9\times 5)\times 1}{\overline{\mathbf{u}}^{(e)}}. \tag{8}$$

The size of each matrix is indicated under the corresponding symbol. It is important to specify that the same approximation is employed for all degrees of freedom (both translational and rotational displacements).

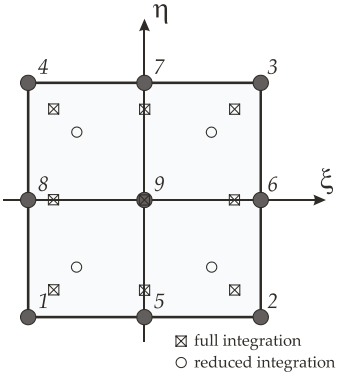

Figure 1. Nine-node quadratic Lagrange rectangular element.

As mentioned in the books by Reddy [14] and Ferreira [17], it is convenient to introduce the natural coordinates ξ, η within the reference finite element, which is called the master element (or parent element). In this reference system, which is also depicted in Figure 1, the shape functions $N_i = N_i(\xi, \eta)$ assume the following definitions:

$$\begin{array}{lll} N_1 = \frac{1}{4}\left(\xi^2 - \xi\right)\left(\eta^2 - \eta\right) & N_2 = \frac{1}{4}\left(\xi^2 + \xi\right)\left(\eta^2 - \eta\right) & N_3 = \frac{1}{4}\left(\xi^2 + \xi\right)\left(\eta^2 + \eta\right) \\ N_4 = \frac{1}{4}\left(\xi^2 - \xi\right)\left(\eta^2 + \eta\right) & N_5 = \frac{1}{2}\left(1 - \xi^2\right)\left(\eta^2 - \eta\right) & N_6 = \frac{1}{2}\left(\xi^2 + \xi\right)\left(1 - \eta^2\right) \\ N_7 = \frac{1}{2}\left(1 - \xi^2\right)\left(\eta^2 + \eta\right) & N_8 = \frac{1}{2}\left(\xi^2 - \xi\right)\left(1 - \eta^2\right) & N_9 = \left(1 - \xi^2\right)\left(1 - \eta^2\right) \end{array}, \tag{9}$$

for $\xi, \eta \in [-1, 1]$. The same functions are also used to describe the geometry of each discrete element according to the principles of the isoparametric FE formulation. The coordinate change between the physical domain and the parent element is accomplished through the relations shown below

$$x^{(e)} = \sum_{i=1}^{9} N_i(\xi, \eta) x_i^{(e)}, y^{(e)} = \sum_{i=1}^{9} N_i(\xi, \eta) y_i^{(e)}, \tag{10}$$

where the couple $x_i^{(e)}, y_i^{(e)}$ defines the coordinates of the i-th node of the generic element. For the sake of conciseness, these quantities can be collected in the corresponding vectors $\mathbf{x}^{(e)}, \mathbf{y}^{(e)}$:

$$\mathbf{x}^e = \begin{bmatrix} x_1^{(e)} & \cdots & x_9^{(e)} \end{bmatrix}^T, \mathbf{y}^e = \begin{bmatrix} y_1^{(e)} & \cdots & y_9^{(e)} \end{bmatrix}^T. \tag{11}$$

The Jacobian matrix **J** related to the coordinate change (10) can be now introduced in order to evaluate the derivatives with respect to the natural coordinates of the parent element:

$$\mathbf{J}=\begin{bmatrix} \frac{\partial x^{(e)}}{\partial \xi} & \frac{\partial y^{(e)}}{\partial \xi} \\ \frac{\partial x^{(e)}}{\partial \eta} & \frac{\partial y^{(e)}}{\partial \eta} \end{bmatrix}=\begin{bmatrix} \sum_{i=1}^{9} x_i^{(e)}\frac{\partial N_i}{\partial \xi} & \sum_{i=1}^{9} y_i^{(e)}\frac{\partial N_i}{\partial \xi} \\ \sum_{i=1}^{9} x_i^{(e)}\frac{\partial N_i}{\partial \eta} & \sum_{i=1}^{9} y_i^{(e)}\frac{\partial N_i}{\partial \eta} \end{bmatrix}=\begin{bmatrix} \mathbf{B}_\xi \\ \mathbf{B}_\eta \end{bmatrix}\begin{bmatrix} \mathbf{x}^{(e)} & \mathbf{y}^{(e)} \end{bmatrix}=\begin{bmatrix} \mathbf{B}_\xi \mathbf{x}^{(e)} & \mathbf{B}_\xi \mathbf{y}^{(e)} \\ \mathbf{B}_\eta \mathbf{x}^{(e)} & \mathbf{B}_\eta \mathbf{y}^{(e)} \end{bmatrix}, \quad (12)$$

where the vectors $\mathbf{B}_\xi, \mathbf{B}_\eta$ collect the derivatives of the shape functions (9) with respect to ξ, η

$$\mathbf{B}_\xi=\begin{bmatrix} \frac{\partial N_1}{\partial \xi} & \cdots & \frac{N_9}{\partial \xi} \end{bmatrix}, \mathbf{B}_\eta=\begin{bmatrix} \frac{\partial N_1}{\partial \eta} & \cdots & \frac{N_9}{\partial \eta} \end{bmatrix}. \quad (13)$$

At this point, the compatibility equations can be presented to define the strain components in each element. In particular, the membrane strains are given by

$$\varepsilon_x^{(e)}=\frac{\partial u_x^{(e)}}{\partial x}=\mathbf{B}_x\mathbf{u}_x^{(e)}, \varepsilon_y^{(e)}=\frac{\partial u_y^{(e)}}{\partial y}=\mathbf{B}_y\mathbf{u}_y^{(e)}, \gamma_{xy}^{(e)}=\frac{\partial u_y^{(e)}}{\partial x}+\frac{\partial u_x^{(e)}}{\partial y}=\mathbf{B}_x\mathbf{u}_y^{(e)}+\mathbf{B}_y\mathbf{u}_x^{(e)}. \quad (14)$$

On the other hand, the bending and twisting curvatures can be defined as follows:

$$k_x^{(e)}=\frac{\partial \phi_x^{(e)}}{\partial x}=\mathbf{B}_x\boldsymbol{\phi}_x^{(e)}, k_y^{(e)}=\frac{\partial \phi_y^{(e)}}{\partial y}=\mathbf{B}_y\boldsymbol{\phi}_y^{(e)}, k_{xy}^{(e)}=\frac{\partial \phi_y^{(e)}}{\partial x}+\frac{\partial \phi_x^{(e)}}{\partial y}=\mathbf{B}_x\boldsymbol{\phi}_y^{(e)}+\mathbf{B}_y\boldsymbol{\phi}_x^{(e)}. \quad (15)$$

Finally, the shear strains assume the following definitions:

$$\gamma_{xz}^{(e)}=\frac{\partial u_z^{(e)}}{\partial x}+\phi_x^{(e)}=\mathbf{B}_x\mathbf{u}_z^{(e)}+\overline{\mathbf{N}}\boldsymbol{\phi}_x^{(e)}, \gamma_{yz}^{(e)}=\frac{\partial u_z^{(e)}}{\partial y}+\phi_y^{(e)}=\mathbf{B}_y\mathbf{u}_z^{(e)}+\overline{\mathbf{N}}\boldsymbol{\phi}_y^{(e)}. \quad (16)$$

Note that the derivatives of the shape functions with respect to the physical coordinates x, y are introduced and collected in the corresponding vectors $\mathbf{B}_x, \mathbf{B}_y$. They can be computed as follows by inverting the Jacobian matrix (this procedure is admissible if its determinant is greater than zero):

$$\begin{bmatrix} \mathbf{B}_x \\ \mathbf{B}_y \end{bmatrix}=\mathbf{J}^{-1}\begin{bmatrix} \mathbf{B}_\xi \\ \mathbf{B}_\eta \end{bmatrix}. \quad (17)$$

The following matrix notation can be used to collect and define the strains previously introduced in (14)–(16):

$$\begin{bmatrix} \varepsilon_x^{(e)} \\ \varepsilon_y^{(e)} \\ \gamma_{xy}^{(e)} \\ k_x^{(e)} \\ k_y^{(e)} \\ k_{xy}^{(e)} \\ \gamma_{xz}^{(e)} \\ \gamma_{yz}^{(e)} \end{bmatrix}=\begin{bmatrix} \mathbf{B}_x & 0 & 0 & 0 & 0 \\ 0 & \mathbf{B}_y & 0 & 0 & 0 \\ \mathbf{B}_y & \mathbf{B}_x & 0 & 0 & 0 \\ 0 & 0 & 0 & \mathbf{B}_x & 0 \\ 0 & 0 & 0 & 0 & \mathbf{B}_y \\ 0 & 0 & 0 & \mathbf{B}_y & \mathbf{B}_x \\ 0 & 0 & \mathbf{B}_x & \overline{\mathbf{N}} & 0 \\ 0 & 0 & \mathbf{B}_y & 0 & \overline{\mathbf{N}} \end{bmatrix}\begin{bmatrix} \mathbf{u}_x^{(e)} \\ \mathbf{u}_y^{(e)} \\ \mathbf{u}_z^{(e)} \\ \boldsymbol{\phi}_x^{(e)} \\ \boldsymbol{\phi}_y^{(e)} \end{bmatrix} \Leftrightarrow \underset{8\times 1}{\boldsymbol{\eta}^{(e)}}=\underset{8\times(9\times 5)}{\mathbf{B}}\underset{(9\times 5)\times 1}{\overline{\mathbf{u}}^{(e)}}. \quad (18)$$

The vector $\boldsymbol{\eta}^{(e)}$ collects the aforementioned strain components. Such terms are needed to compute the stress resultants in each element by means of the constitutive relation shown below in matrix form:

$$\begin{bmatrix} N_x^{(e)} \\ N_y^{(e)} \\ N_{xy}^{(e)} \\ M_x^{(e)} \\ M_y^{(e)} \\ M_{xy}^{(e)} \\ T_x^{(e)} \\ T_y^{(e)} \end{bmatrix} = \begin{bmatrix} A_{11} & A_{12} & A_{16} & B_{11} & B_{12} & B_{16} & 0 & 0 \\ A_{12} & A_{22} & A_{26} & B_{12} & B_{22} & B_{26} & 0 & 0 \\ A_{16} & A_{26} & A_{66} & B_{16} & B_{26} & B_{66} & 0 & 0 \\ B_{11} & B_{12} & B_{16} & D_{11} & D_{12} & D_{16} & 0 & 0 \\ B_{12} & B_{22} & B_{26} & D_{12} & D_{22} & D_{26} & 0 & 0 \\ B_{16} & B_{26} & B_{66} & D_{16} & D_{26} & D_{66} & 0 & 0 \\ 0 & 0 & 0 & 0 & 0 & 0 & \kappa A_{44} & \kappa A_{45} \\ 0 & 0 & 0 & 0 & 0 & 0 & \kappa A_{45} & \kappa A_{55} \end{bmatrix} \begin{bmatrix} \varepsilon_x^{(e)} \\ \varepsilon_y^{(e)} \\ \gamma_{xy}^{(e)} \\ k_x^{(e)} \\ k_y^{(e)} \\ k_{xy}^{(e)} \\ \gamma_{xz}^{(e)} \\ \gamma_{yz}^{(e)} \end{bmatrix}, \tag{19}$$

in which $N_x^{(e)}, N_y^{(e)}, N_{xy}^{(e)}$ are the membrane forces, $M_x^{(e)}, M_y^{(e)}, M_{xy}^{(e)}$ the bending and twisting moments, and $T_x^{(e)}, T_y^{(e)}$ the shear stresses. On the other hand, κ stands for the shear correction factor. For moderately thick and thick plates, which are commonly studied through the FSDT, the shear correction factor is generally assumed equal to $5/6$. Nevertheless, the same structural model can be employed to accurately investigate the mechanical behavior of thin plates, which are usually analyzed in the theoretical framework provided by the classical laminated plate theory (CLPT), taking the Kirchhoff hypothesis into account. This theory neglects the shear stresses, and the same circumstance can be obtained from the FSDT by setting 10^6 as the shear correction factor. In other words, the effect of shear stresses is negligible if the shear stiffness is extremely large [71].

The stress resultants can be also expressed as follows in extended matrix form in terms of nodal displacements, having in mind the definitions (18)

$$\begin{bmatrix} N_x^{(e)} \\ N_y^{(e)} \\ N_{xy}^{(e)} \\ M_x^{(e)} \\ M_y^{(e)} \\ M_{xy}^{(e)} \\ T_x^{(e)} \\ T_y^{(e)} \end{bmatrix} = \begin{bmatrix} A_{11}\mathbf{B}_x + A_{16}\mathbf{B}_y & A_{12}\mathbf{B}_y + A_{16}\mathbf{B}_x & 0 & B_{11}\mathbf{B}_x + B_{16}\mathbf{B}_y & B_{12}\mathbf{B}_y + B_{16}\mathbf{B}_x \\ A_{12}\mathbf{B}_x + A_{26}\mathbf{B}_y & A_{22}\mathbf{B}_y + A_{26}\mathbf{B}_x & 0 & B_{12}\mathbf{B}_x + B_{26}\mathbf{B}_y & B_{22}\mathbf{B}_y + B_{26}\mathbf{B}_x \\ A_{16}\mathbf{B}_x + A_{66}\mathbf{B}_y & A_{26}\mathbf{B}_y + A_{66}\mathbf{B}_x & 0 & B_{16}\mathbf{B}_x + B_{66}\mathbf{B}_y & B_{26}\mathbf{B}_y + B_{66}\mathbf{B}_x \\ B_{11}\mathbf{B}_x + B_{16}\mathbf{B}_y & B_{12}\mathbf{B}_y + B_{16}\mathbf{B}_x & 0 & D_{11}\mathbf{B}_x + D_{16}\mathbf{B}_y & D_{12}\mathbf{B}_y + D_{16}\mathbf{B}_x \\ B_{12}\mathbf{B}_x + B_{26}\mathbf{B}_y & B_{22}\mathbf{B}_y + B_{26}\mathbf{B}_x & 0 & D_{12}\mathbf{B}_x + D_{26}\mathbf{B}_y & D_{22}\mathbf{B}_y + D_{26}\mathbf{B}_x \\ B_{16}\mathbf{B}_x + B_{66}\mathbf{B}_y & B_{26}\mathbf{B}_y + B_{66}\mathbf{B}_x & 0 & D_{16}\mathbf{B}_x + D_{66}\mathbf{B}_y & D_{26}\mathbf{B}_y + D_{66}\mathbf{B}_x \\ 0 & 0 & \kappa A_{44}\mathbf{B}_x + \kappa A_{45}\mathbf{B}_y & \kappa A_{44}\overline{\mathbf{N}} & \kappa A_{45}\overline{\mathbf{N}} \\ 0 & 0 & \kappa A_{45}\mathbf{B}_x + \kappa A_{55}\mathbf{B}_y & \kappa A_{45}\overline{\mathbf{N}} & \kappa A_{55}\overline{\mathbf{N}} \end{bmatrix} \begin{bmatrix} \mathbf{u}_x^{(e)} \\ \mathbf{u}_y^{(e)} \\ \mathbf{u}_z^{(e)} \\ \boldsymbol{\phi}_x^{(e)} \\ \boldsymbol{\phi}_y^{(e)} \end{bmatrix} \tag{20}$$

or in compact matrix form

$$\underset{8\times 1}{\mathbf{S}^{(e)}} = \underset{8\times 8}{\mathbf{C}} \; \underset{8\times(9\times 5)}{\mathbf{B}} \; \underset{(9\times 5)\times 1}{\overline{\mathbf{u}}^{(e)}}, \tag{21}$$

where the meaning of the constitutive operator $\mathbf{C}$ can be deduced from Equation (19). It should be observed that the mechanical properties are the same in each element, and the corresponding coefficients are defined as

$$\left(A_{ij}, B_{ij}, D_{ij}\right) = \sum_{k=1}^{N_L} \int_{z_k}^{z_{k+1}} \overline{Q}_{ij}^{(k)} \left(1, z, z^2\right) dz, \tag{22}$$

where $\overline{Q}_{ij}^{(k)}$ represents the stiffnesses of the k-th orthotropic layer, which can be oriented as $\theta^{(k)}$. Once the orientation of the fibers is defined, the following relations are employed to compute the coefficients $\overline{Q}_{ij}^{(k)}$:

$$\begin{aligned}
\overline{Q}_{11}^{(k)} &= Q_{11}^{(k)}\cos^4\theta^{(k)} + 2\Big(Q_{12}^{(k)} + 2Q_{66}^{(k)}\Big)\sin^2\theta^{(k)}\cos^2\theta^{(k)} + Q_{22}^{(k)}\sin^4\theta^{(k)}\\
\overline{Q}_{12}^{(k)} &= \Big(Q_{11}^{(k)} + Q_{22}^{(k)} - 4Q_{66}^{(k)}\Big)\sin^2\theta^{(k)}\cos^2\theta^{(k)} + Q_{12}^{(k)}\Big(\sin^4\theta^{(k)} + \cos^4\theta^{(k)}\Big)\\
\overline{Q}_{22}^{(k)} &= Q_{11}^{(k)}\sin^4\theta^{(k)} + 2\Big(Q_{12}^{(k)} + 2Q_{66}^{(k)}\Big)\sin^2\theta^{(k)}\cos^2\theta^{(k)} + Q_{22}^{(k)}\cos^4\theta^{(k)}\\
\overline{Q}_{16}^{(k)} &= \Big(Q_{11}^{(k)} - Q_{12}^{(k)} - 2Q_{66}^{(k)}\Big)\sin\theta^{(k)}\cos^3\theta^{(k)} + \Big(Q_{12}^{(k)} - Q_{22}^{(k)} + 2Q_{66}^{(k)}\Big)\sin^3\theta^{(k)}\cos\theta^{(k)}\\
\overline{Q}_{26}^{(k)} &= \Big(Q_{11}^{(k)} - Q_{12}^{(k)} - 2Q_{66}^{(k)}\Big)\sin^3\theta^{(k)}\cos\theta^{(k)} + \Big(Q_{12}^{(k)} - Q_{22}^{(k)} + 2Q_{66}^{(k)}\Big)\sin\theta^{(k)}\cos^3\theta^{(k)}\\
\overline{Q}_{66}^{(k)} &= \Big(Q_{11}^{(k)} + Q_{22}^{(k)} - 2Q_{12}^{(k)} - 2Q_{66}^{(k)}\Big)\sin^2\theta^{(k)}\cos^2\theta^{(k)} + Q_{66}^{(k)}\Big(\sin^4\theta^{(k)} + \cos^4\theta^{(k)}\Big)\\
\overline{Q}_{44}^{(k)} &= Q_{44}^{(k)}\cos^2\theta^{(k)} + Q_{55}^{(k)}\sin^2\theta^{(k)}\\
\overline{Q}_{45}^{(k)} &= \Big(Q_{44}^{(k)} - Q_{55}^{(k)}\Big)\sin\theta^{(k)}\cos\theta^{(k)}\\
\overline{Q}_{55}^{(k)} &= Q_{55}^{(k)}\cos^2\theta^{(k)} + Q_{44}^{(k)}\sin^2\theta^{(k)}
\end{aligned} \quad , \tag{23}$$

where the quantities $Q_{ij}^{(k)}$ are defined below in terms of the engineering constants of the corresponding layer, which are the Young's moduli $E_{11}^{(k)}, E_{22}^{(k)}$, the shear moduli $G_{12}^{(k)}, G_{13}^{(k)}, G_{23}^{(k)}$, and the Poisson's ratio $\nu_{12}^{(k)}$:

$$Q_{11}^{(k)} = \frac{E_{11}^{(k)}}{1-\nu_{12}^{(k)}\nu_{21}^{(k)}}, \quad Q_{22}^{(k)} = \frac{E_{22}^{(k)}}{1-\nu_{12}^{(k)}\nu_{21}^{(k)}}, \quad Q_{12}^{(k)} = \frac{\nu_{12}^{(k)}E_{22}^{(k)}}{1-\nu_{12}^{(k)}\nu_{21}^{(k)}}, \quad Q_{66}^{(k)} = G_{12}^{(k)}, \quad Q_{44}^{(k)} = G_{13}^{(k)}, \quad Q_{55}^{(k)} = G_{23}^{(k)}. \tag{24}$$

It should be recalled that the Poisson's ratio $\nu_{21}^{(k)}$ can be evaluated by using the well-known relation for orthotropic materials $\nu_{21}^{(k)} = E_{22}^{(k)}\nu_{12}^{(k)}/E_{11}^{(k)}$.

The engineering constants are computed by means of the Halpin–Tsai approach, once the mechanical features of the reinforcing fibers and the epoxy resin of the orthotropic fiber-reinforced layers are known. As highlighted in [35], this methodology can be applied by using Hill's elastic moduli and a semi-empirical approach. The reinforcing fibers are modeled as a transversely isotropic material, and the following engineering constants are required to characterize them: the Young's moduli E_{11}^F, E_{22}^F, the shear modulus G_{12}^F, and the Poisson's ratios ν_{12}^F, ν_{23}^F. The Hills's elastic moduli of the fibers k_F, l_F, m_F, n_F, p_F are given by:

$$\begin{gathered}
k_F = \frac{E_{22}^F}{2\Big(1-\nu_{23}^F - 2\nu_{21}^F\nu_{12}^F\Big)}, \qquad l_F = 2\nu_{12}^F k_F, \qquad m_F = \frac{1-\nu_{23}^F - 2\nu_{21}^F\nu_{12}^F}{1+\nu_{23}^F}k_F,\\
n_F = 2\Big(1-\nu_{23}^F\Big)\frac{E_{11}^F}{E_{22}^F}k_F, \qquad p_F = G_{12}^F
\end{gathered} \quad . \tag{25}$$

On the other hand, the epoxy resin is modeled as an isotropic medium characterized by its Young's modulus E^M and its Poisson's ratio ν^M. The Hill's elastic moduli of the matrix k_M, l_M, m_M, n_M, p_M are defined below:

$$\begin{gathered}
k_M = \frac{E^M}{2(1+\nu^M)(1-2\nu^M)}, \qquad l_M = 2\nu^M k_M, \qquad m_M = \Big(1-2\nu^M\Big)k_M,\\
n_M = 2\Big(1-\nu^M\Big)k_M, \qquad p_M = \Big(1-2\nu^M\Big)k_M
\end{gathered} \quad . \tag{26}$$

At this point, the overall mechanical properties of the composite material can be computed in terms of the Hill's elastic moduli k, l, m, n, p:

$$
\begin{aligned}
k &= \frac{k_M(k_F+m_M)V_M + k_F(k_M+m_M)V_F}{(k_F+m_M)V_M + (k_M+m_M)V_F} \\
l &= V_F l_F + V_M l_M + \frac{l_F - l_M}{k_F - k_M}(k - V_F k_F - V_M k_M) \\
m &= m_M \frac{2V_F m_F(k_M+m_M) + 2V_M m_F m_M + V_M k_M(m_F+m_M)}{2V_F m_M(k_M+m_M) + 2V_M m_F m_M + V_M k_M(m_F+m_M)} \\
n &= V_F n_F + V_M n_M + \left(\frac{l_F - l_M}{k_F - k_M}\right)^2 (k - V_F k_F - V_M k_M) \\
p &= \frac{(p_F+p_M)p_M V_M + 2p_F p_M V_F}{(p_F+p_M)V_M + 2p_M V_F}
\end{aligned}
\quad , \tag{27}
$$

where V_F, V_M are the volume fractions of the fibers and of the matrix, respectively. They are related by the following relation: $V_M = 1 - V_F$. In the current research, a non-uniform distribution of the fibers is defined along the plate thickness. Therefore, the volume fraction of the reinforcing fibers turns out to be a function of the thickness coordinate $V_F = V_F(z) = \widetilde{V}_F f^{(k)}(z)$, in which $\widetilde{V}_F$ represents a constant value. This idea is representative of functionally graded materials. Several distributions $f^{(k)}(z)$ can be introduced toward this aim, and can be applied in each layer separately. The following functions are used in this paper:

$$
f^{(k)}(z) = \begin{cases}
f_{UD}^{(k)}(z) = 1 \\
f_{O}^{(k)}(z) = 1 - \dfrac{1}{2}\left|\dfrac{2(z-z_k)}{z_{k+1}-z_k} - \dfrac{2(z_{k+1}-z)}{z_{k+1}-z_k}\right| \\
f_{X}^{(k)}(z) = \dfrac{1}{2}\left|\dfrac{2(z-z_k)}{z_{k+1}-z_k} - \dfrac{2(z_{k+1}-z)}{z_{k+1}-z_k}\right| \\
f_{V}^{(k)}(z) = \dfrac{z-z_k}{z_{k+1}-z_k} \\
f_{A}^{(k)}(z) = \dfrac{z_{k+1}-z}{z_{k+1}-z_k}
\end{cases} . \tag{28}
$$

For the sake of completeness, these functions are depicted in Figure 2.

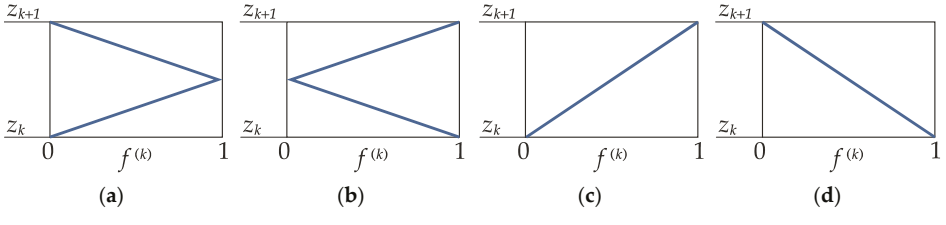

Figure 2. Through-the-thickness variation of $f^{(k)}$: (**a**) $f_O^{(k)}$; (**b**) $f_X^{(k)}$; (**c**) $f_V^{(k)}$; (**d**) $f_A^{(k)}$.

Once the Hill's elastic moduli (27) are computed, the engineering constants of the k-th fiber reinforced composite layer can be evaluated as well. The definitions shown below are required for this purpose:

$$
E_{11}^{(k)} = n - \frac{l^2}{k}, E_{22}^{(k)} = \frac{4m\left(kn - l^2\right)}{kn - l^2 + mn}, \nu_{12}^{(k)} = \frac{l}{2k}, G_{12}^{(k)} = G_{13}^{(k)} = p, G_{23}^{(k)} = m. \tag{29}
$$

It should be noted that these quantities are all functions of the thickness coordinate z due to the relations (28). As a consequence, the material properties $\overline{Q}_{ij}^{(k)}$ defined in (23) depend also on the coordinate z, and the integrals in (22) have to be computed numerically. The function "*trapz*" embedded in MATLAB was employed toward this aim.

At this point, the Hamilton's variational principle can be applied to obtain the equations of motion and the corresponding weak form [23]. As a result, it is possible to write the dynamic fundamental system in each element as follows:

$$\underset{(9\times5)\times(9\times5)}{\mathbf{K}^{(e)}}\ \underset{(9\times5)\times1}{\overline{\mathbf{u}}^{(e)}} + \underset{(9\times5)\times(9\times5)}{\mathbf{M}^{(e)}}\ \underset{(9\times5)\times1}{\ddot{\overline{\mathbf{u}}}^{(e)}} = 0, \tag{30}$$

where the stiffness matrix of the element is denoted by $\mathbf{K}^{(e)}$, whereas the mass matrix is identified by $\mathbf{M}^{(e)}$. On the other hand, the vector $\ddot{\overline{\mathbf{u}}}^{(e)}$ collects the second-order derivatives with respect to the time variable t of the nodal displacements (7). By definition, the stiffness matrix $\mathbf{K}^{(e)}$ assumes the following aspect:

$$\mathbf{K}^{(e)} = \int_x \int_y \underset{(9\times5)\times8}{\mathbf{B}^T}\ \underset{8\times8}{\mathbf{C}}\ \underset{8\times(9\times5)}{\mathbf{B}}\, dxdy = \begin{bmatrix} \mathbf{K}_{11} & \mathbf{K}_{12} & \mathbf{K}_{13} & \mathbf{K}_{14} & \mathbf{K}_{15} \\ \mathbf{K}_{21} & \mathbf{K}_{22} & \mathbf{K}_{23} & \mathbf{K}_{24} & \mathbf{K}_{25} \\ \mathbf{K}_{31} & \mathbf{K}_{32} & \mathbf{K}_{33} & \mathbf{K}_{34} & \mathbf{K}_{35} \\ \mathbf{K}_{41} & \mathbf{K}_{42} & \mathbf{K}_{43} & \mathbf{K}_{44} & \mathbf{K}_{45} \\ \mathbf{K}_{51} & \mathbf{K}_{52} & \mathbf{K}_{53} & \mathbf{K}_{54} & \mathbf{K}_{55} \end{bmatrix}, \tag{31}$$

where the operators $\mathbf{K}_{ij}$ of size 9×9 are illustrated in Appendix A. Analogously, the mass matrix $\mathbf{M}^{(e)}$ can be written as follows:

$$\mathbf{M}^{(e)} = \int_x \int_y \underset{(9\times5)\times5}{\mathbf{N}^T}\ \underset{5\times5}{\mathbf{m}}\ \underset{5\times(9\times5)}{\mathbf{N}}\, dxdy = \begin{bmatrix} \mathbf{M}_{11} & 0 & 0 & \mathbf{M}_{14} & 0 \\ 0 & \mathbf{M}_{22} & 0 & 0 & \mathbf{M}_{25} \\ 0 & 0 & \mathbf{M}_{33} & 0 & 0 \\ \mathbf{M}_{41} & 0 & 0 & \mathbf{M}_{44} & 0 \\ 0 & \mathbf{M}_{52} & 0 & 0 & \mathbf{M}_{55} \end{bmatrix}, \tag{32}$$

where the operators $\mathbf{M}_{ij}$ of size 9×9 are also illustrated in Appendix A. The matrix $\mathbf{m}$ instead collects the inertia terms and assumes the definition shown below:

$$\mathbf{m} = \begin{bmatrix} I_0 & 0 & 0 & I_1 & 0 \\ 0 & I_0 & 0 & 0 & I_1 \\ 0 & 0 & I_0 & 0 & 0 \\ I_1 & 0 & 0 & I_2 & 0 \\ 0 & I_1 & 0 & 0 & I_2 \end{bmatrix}, \tag{33}$$

in which

$$I_i = \sum_{k=1}^{N_L} \int_{z_k}^{z_{k+1}} \rho^{(k)} z^i dz, \tag{34}$$

where $\rho^{(k)}$ is the density of the k-th layer. Its value can be obtained by means of the rule of mixture, combining the densities of the reinforcing fibers $\rho_F^{(k)}$ and of the matrix $\rho_M^{(k)}$:

$$\rho^{(k)} = V_F \rho_F^{(k)} + V_M \rho_M^{(k)}. \tag{35}$$

Note that the density is also a function of the thickness coordinate z due to the through-the-thickness variation of the volume fraction of the fibers. Therefore, the integrals in (34) have to be computed numerically as well.

2.1. Numerical Evaluation of the Fundamental Operators

It is well-known that the integrals in definitions (31) and (32) require a tool to be computed numerically. In the current research, the Gauss–Legendre rule is used. According to this approach, the infinitesimal area $dxdy$ is evaluated in the master element as follows, through the determinant of the Jacobian matrix: $dxdy = \det\mathbf{J}d\xi d\eta$. Consequently, the integral of a generic two-dimensional function $F(x, y)$ can be written as

$$\int_x \int_y F(x,y)dxdy = \int_{-1}^{1}\int_{-1}^{1} F(\xi,\eta)\det\mathbf{J}d\xi d\eta. \tag{36}$$

At this point, the integral is converted into a weighted linear sum by introducing the roots of Legendre polynomials ξ_I, η_J and the corresponding weighting coefficients W_I, W_J:

$$\int_{-1}^{1}\int_{-1}^{1} F(\xi,\eta)\det\mathbf{J}d\xi d\eta \approx \sum_{I=1}^{M}\sum_{J=1}^{N} F\left(\xi_I,\eta_J\right)\det\mathbf{J}|_{\xi_I,\eta_J} W_I W_J. \tag{37}$$

The values of the roots of Legendre polynomials and the corresponding weighting coefficients used in the numerical integration are listed in Table 1. Recall that the full integration is performed by setting $N = M = 3$. On the other hand, the reduced integration is accomplished for $N = M = 2$ as far as the shear terms are concerned. In other words, the elements of the stiffness matrix which involve the mechanical properties A_{44}, A_{45}, A_{55} are computed by means of the reduced integration. This procedure aims to avoid the shear locking problem as highlighted in the book by Reddy [14]. For the sake of completeness, the roots of Legendre polynomials are also depicted in Figure 1, for both the full and reduced integrations.

Table 1. Roots of Legendre polynomials and weighting coefficients for the numerical integration.

N, M	ξ_I, η_J	W_I, W_J
2	$\pm 1/\sqrt{3}$	1
3	$\pm\sqrt{3/5}$	5/9
	0	8/9

Finally, the assembly procedure is performed to enforce the C^0 compatibility conditions among the elements in which the reference domain is divided. In other words, the model is characterized by continuous displacements at the interfaces of the elements. The global discrete system of governing equations assumes the following aspect:

$$\underset{N_{dofs}\times N_{dofs}N_{dofs}\times 1}{\mathbf{K}}\ \underset{}{\mathbf{u}} + \underset{N_{dofs}\times N_{dofs}N_{dofs}\times 1}{\mathbf{M}}\ \ddot{\mathbf{u}} = 0, \tag{38}$$

where the number of degrees of freedom is given by $N_{dofs} = 5 \times N_P$, N_P being the number of nodes of the discrete domain. With reference to Equation (38), $\mathbf{K}, \mathbf{M}$ clearly stand for the global stiffness and mass matrices, whereas $\mathbf{u}$ is the vector of the nodal displacements of the global system defined below:

$$\mathbf{u} = \begin{bmatrix} u_{x,1} & \cdots & u_{x,N_P} & u_{y,1} & \cdots & u_{y,N_P} & u_{z,1} & \cdots & u_{z,N_P} & \phi_{x,1} & \cdots & \phi_{x,N_P} & \phi_{y,1} & \cdots & \phi_{y,N_P} \end{bmatrix}^T, \tag{39}$$

in which the numbering is performed following the scheme in Figure 3. Finally, $\ddot{\mathbf{u}}$ is the vector that collects the second-order time derivatives of the nodal displacements.

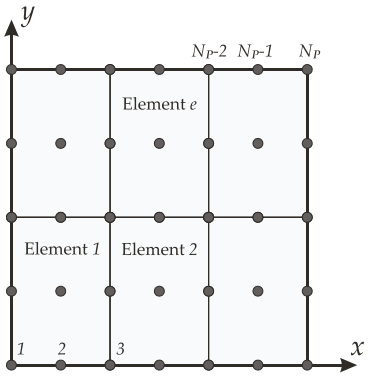

Figure 3. Example of a discrete domain and node numbering.

2.2. Natural Frequency Analysis

Once the discrete fundamental system (38) is defined and the proper boundary conditions are enforced, the separation of variables provide the following relation:

$$\left(\mathbf{K} - \omega^2 \mathbf{M}\right)\mathbf{d} = 0, \tag{40}$$

in which ω represents the circular frequencies of the structural system, whereas the vector $\mathbf{d}$ collects the corresponding modal amplitudes. The natural frequencies of the plate can be evaluated as $f_n = \omega/2\pi$. It can be observed that the expression (40) is a generalized eigenvalue problem. In the present research, the function "*eigs*" embedded in MATLAB was employed to obtain the natural frequencies and the mode shapes of the laminated composite plates.

3. Numerical Applications

The formulation illustrated in the previous section was implemented in a MATLAB code. The current approach was first validated by means of the comparison with the semi-analytical solutions provided by Reddy in his book [23], for both thin and thick simply-supported plates with an antisymmetric cross-ply layup. In these circumstances, a uniform distribution of the fiber was assumed along the plate thickness.

The convergence analysis was also performed for the sake of completeness. Subsequently, the natural frequencies of functionally graded orthotropic laminated plates are discussed. The geometry of the plates considered in the numerical applications was defined by $L_x = L_y = 1$ m, whereas their lamination scheme was given by $\left(0^\circ/90^\circ/0^\circ/90^\circ\right)$. The four layers were characterized by the same value of $\widetilde{V}_F = 0.6$, whereas their thickness was assumed as 2.5×10^{-3} m for thin plates and as 2.5×10^{-2} m for the thick ones. The mechanical properties of the constituents (Carbon fibers and epoxy resin) are listed in Table 2.

Table 2. Mechanical properties of the layer constituents.

Constituent	Young's Moduli	Shear Moduli	Poisson's Ratios	Density
Carbon fibers	$E^F_{11} = 230$ GPa $E^F_{22} = 15$ GPa	$G^F_{12} = 50$ GPa	$\nu^F_{12} = 0.20$ $\nu^F_{23} = 0.25$	$\rho^F = 1800$ kg/m^3
Epoxy resin	$E^M = 3.27$ GPa	-	$\nu^M = 0.38$	$\rho^M = 1200$ kg/m^3

3.1. Convergence and Accuracy

The convergence analysis was performed by increasing the number of discrete elements up to 256, which means 16 elements along each principal direction. The results of this test are presented in Table 3 for a thin plate and in Table 4 for the thicker ones, in terms of the first ten natural frequencies. A very good accuracy was obtained by using only eight finite elements per side, for both cases under consideration. In particular, the percentage error for the first mode shapes was lower than 0.4% if 64 elements were used. Therefore, the formulation and the numerical approach were validated. Only the bending mode shapes were considered in the analyses.

Table 3. Convergence features of the numerical approach and comparison of the first ten natural frequencies (Hz) with the semi-analytical solutions provided by Reddy [23] for a simply-supported thin plate with a through-the-thickness uniform distribution of the reinforcing fibers. CLPT: classical laminated plate theory.

Mode	CLPT Ref. [23]	4 Elements N_{dofs}=125	16 Elements N_{dofs}=405	64 Elements N_{dofs}=1445	256 Elements N_{dofs}=5445
1	43.9262	44.4153	43.9592	43.9284	43.9265
2	123.1041	135.1515	124.3804	123.1900	123.1096
3	123.1041	135.1515	124.3804	123.1901	123.1096
4	175.6547	192.6267	177.6096	175.7865	175.6632
5	265.0021	505.8042	278.5590	265.9668	265.0653
6	265.0021	505.8084	278.5590	265.9668	265.0653
7	300.0618	533.0928	313.2389	300.9965	300.1230
8	300.0618	533.0928	313.2389	300.9965	300.1230
9	395.0350	751.5685	415.3231	396.4841	395.1299
10	465.3946	838.4999	515.4317	470.6168	465.7466

Table 4. Convergence features of the numerical approach and comparison of the first ten natural frequencies (Hz) with the semi-analytical solutions provided by Reddy [23] for a simply-supported thick plate with a through-the-thickness uniform distribution of the reinforcing fibers. FSDT: first-order shear deformation theory.

Mode	FSDT Ref. [23]	4 Elements N_{dofs}=125	16 Elements N_{dofs}=405	64 Elements N_{dofs}=1445	256 Elements N_{dofs}=5445
1	397.3772	400.9285	397.6161	397.3928	397.3782
2	939.4637	987.3930	946.0547	939.9116	939.4924
3	939.4637	987.3930	946.0547	939.9116	939.4924
4	1285.7309	1295.8113	1293.1889	1286.2465	1285.7646
5	1640.7304	2202.4349	1687.2607	1644.1525	1640.9552
6	1640.7304	2219.9298	1687.2607	1644.1525	1640.9552
7	1869.3853	2219.9298	1905.9136	1872.1146	1869.5668
8	1869.3853	2224.7306	1905.9136	1872.1146	1869.5668
9	2313.9852	2486.7150	2349.5762	2316.8723	2314.1827
10	2372.3369	3354.9399	2442.9101	2385.5578	2373.2355

For completeness, the convergence features of the proposed approach are presented in graphical form in Figure 4, where the relative error $e_r = f_n / f_{n,exact} - 1$ was computed for increasing values of the degrees of freedom (N_{dofs}). The graphs are presented in logarithmic scale. It can be observed that a good convergence was reached for both thin and thick plates.

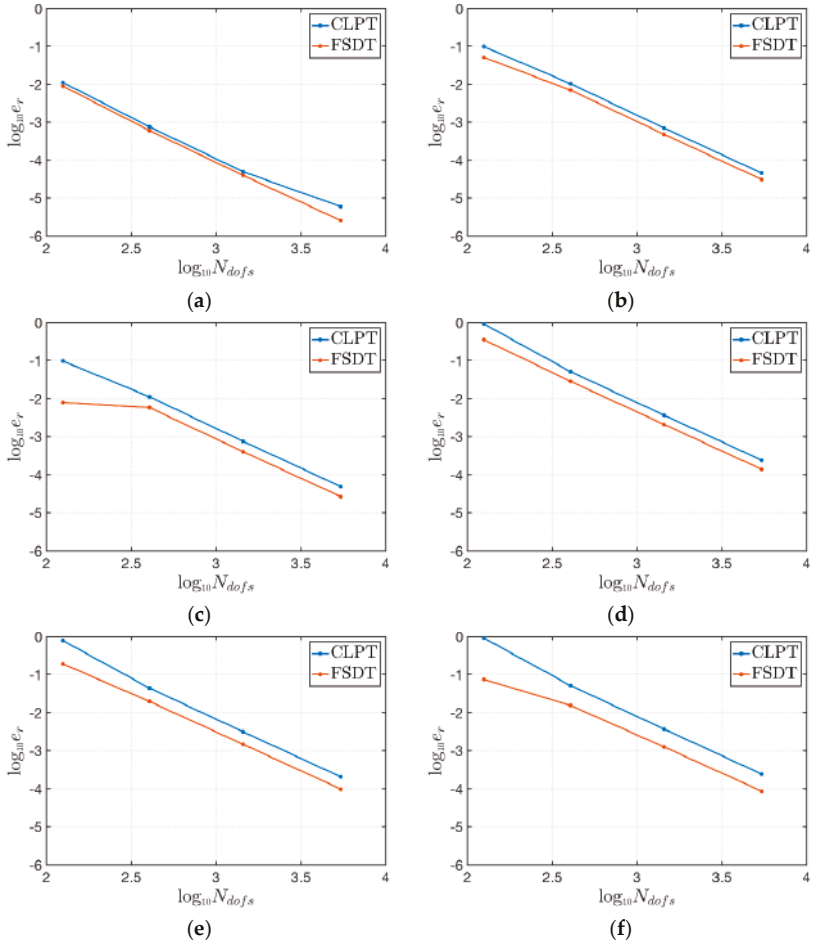

Figure 4. Convergence graphs for thin (CLPT) and thick (FSDT) laminated plates in terms of natural frequencies: (**a**) first frequency; (**b**) second frequency; (**c**) third frequency; (**d**) fourth frequency; (**e**) fifth frequency; (**f**) sixth frequency.

3.2. Natural Frequency Analysis of Functionally Graded Orthotropic Plates

In this section, four different through-the-thickness fiber distributions are analyzed. These four schemes, as well as the functions $f^{(k)}$ employed in each layer, are summarized in Table 5. The layers were numbered from the bottom to the top surface of the plate. As far as the mechanical and geometric features of the plates are concerned, the same values of the previous section were used. Due to the results of the convergence analyses, the plates were discretized by using ten finite elements per side. The first fourteen natural frequencies of a simply-supported thin plate for the various through-the-thickness distributions of the reinforcing fibers specified in Table 5 are presented in Table 6, whereas Table 7 collects the same results for a simply-supported thick plate. Finally, the first six mode shapes are also depicted in graphical form. In particular, Figure 5 presents the mode shapes related to the thin plates, whereas the same results for the thick plates are shown in Figure 6. Note that the mode shapes assumed different aspects by varying the through-the-thickness distributions of the fibers in the four layers, keeping their orientation constant. Analogously, the values of natural frequencies were

affected by the non-uniform distribution of the fibers along the thickness of the structures, for both thin and thick configurations.

Table 5. Definition of the through-the-thickness distribution of the reinforcing fibers.

Scheme	Layer 1	Layer 2	Layer 3	Layer 4
Scheme 1	$f_{UD}^{(1)}$	$f_{UD}^{(2)}$	$f_{UD}^{(3)}$	$f_{UD}^{(4)}$
Scheme 2	$f_{O}^{(1)}$	$f_{O}^{(2)}$	$f_{O}^{(3)}$	$f_{O}^{(4)}$
Scheme 3	$f_{X}^{(1)}$	$f_{X}^{(2)}$	$f_{X}^{(3)}$	$f_{X}^{(4)}$
Scheme 4	$f_{V}^{(1)}$	$f_{UD}^{(2)}$	$f_{UD}^{(3)}$	$f_{A}^{(4)}$

Table 6. First fourteen natural frequencies (Hz) of a simply-supported thin plate for several through-the-thickness distributions of the reinforcing fibers.

Mode	Scheme 1	Scheme 2	Scheme 3	Scheme 4
1	43.9271	33.5339	35.0923	34.5204
2	123.1397	93.9281	97.6817	96.4943
3	123.1397	93.9281	97.6817	96.4994
4	175.7093	134.1367	140.3692	138.0894
5	265.4059	202.3576	209.7406	207.6677
6	265.4059	202.3576	209.7406	207.6780
7	300.4527	229.2791	239.2330	235.8151
8	300.4527	229.2791	239.2330	235.8250
9	395.6415	302.0350	316.0631	310.9587
10	467.6067	356.4637	368.9774	365.6794
11	467.6067	356.4637	368.9774	365.6944
12	494.2235	376.9847	392.0326	387.3268
13	494.2235	376.9847	392.0326	387.3477
14	565.8001	431.8446	451.1608	444.3823

Table 7. First fourteen natural frequencies (Hz) of a simply-supported thick plate for several through-the-thickness distributions of the reinforcing fibers.

Mode	Scheme 1	Scheme 2	Scheme 3	Scheme 4
1	397.3836	306.5341	318.4900	319.8942
2	939.6493	734.9017	753.9989	780.5089
3	939.6493	734.9017	753.9989	780.5337
4	1285.9465	1008.8635	1036.0206	1077.1948
5	1642.1651	1300.8952	1322.6235	1405.6371
6	1642.1651	1300.8952	1322.6235	1405.6638
7	1870.5349	1480.8980	1510.3561	1600.6668
8	1870.5349	1480.8980	1510.3561	1600.6865
9	2315.2138	1839.1055	1872.3302	1997.7076
10	2377.9654	1899.9655	1921.4452	2077.7168
11	2377.9654	1899.9655	1921.4452	2077.7322
12	2545.0693	2031.1334	2059.3510	2219.4198
13	2545.0693	2031.1334	2059.3510	2219.4394
14	2888.3228	2306.5360	2339.2521	2523.7454

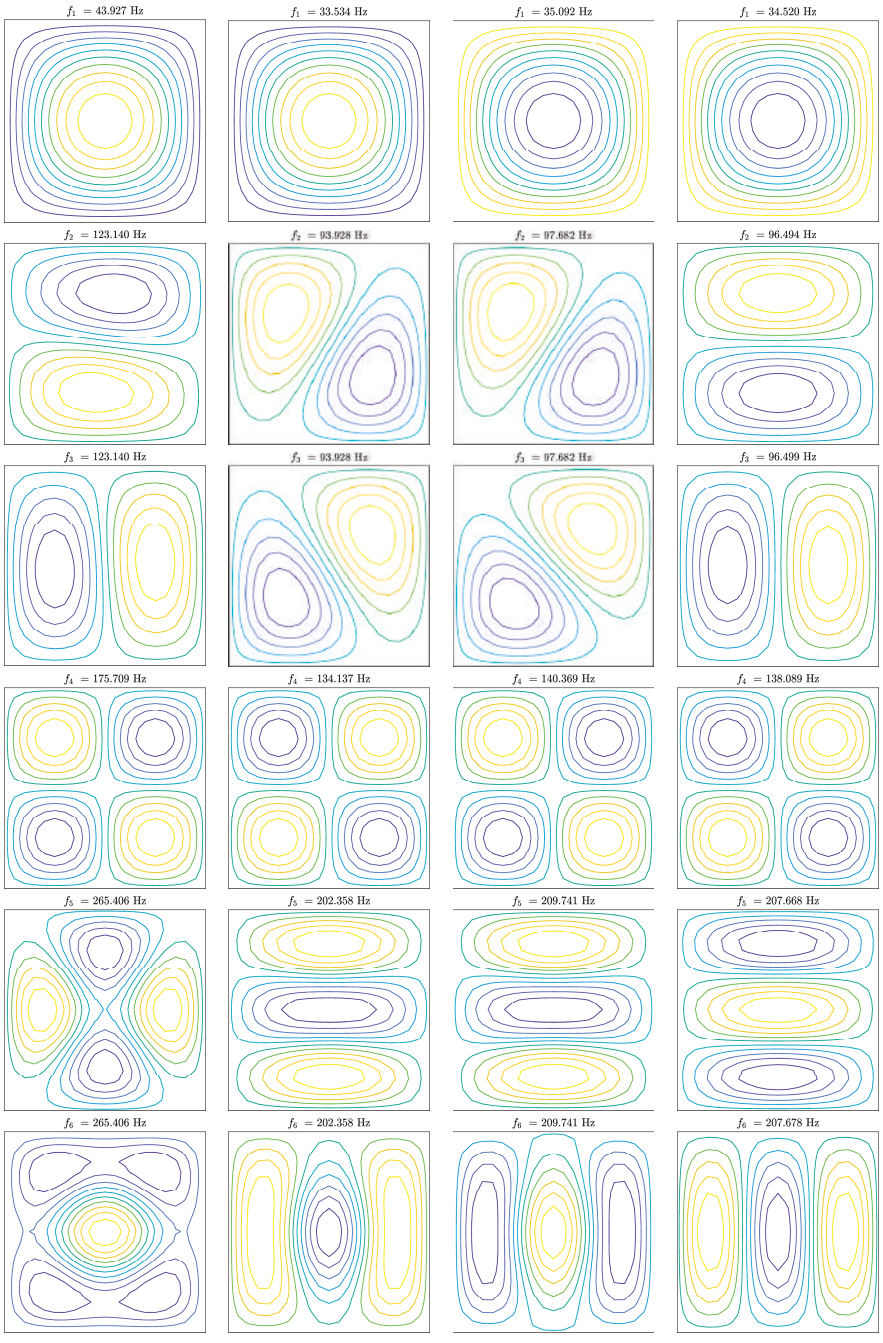

Figure 5. First six mode shapes for a simply-supported laminated thin plate with different fiber distributions: (**a**) Scheme 1 (uniform); (**b**) Scheme 2; (**c**) Scheme 3; (**d**) Scheme 4.

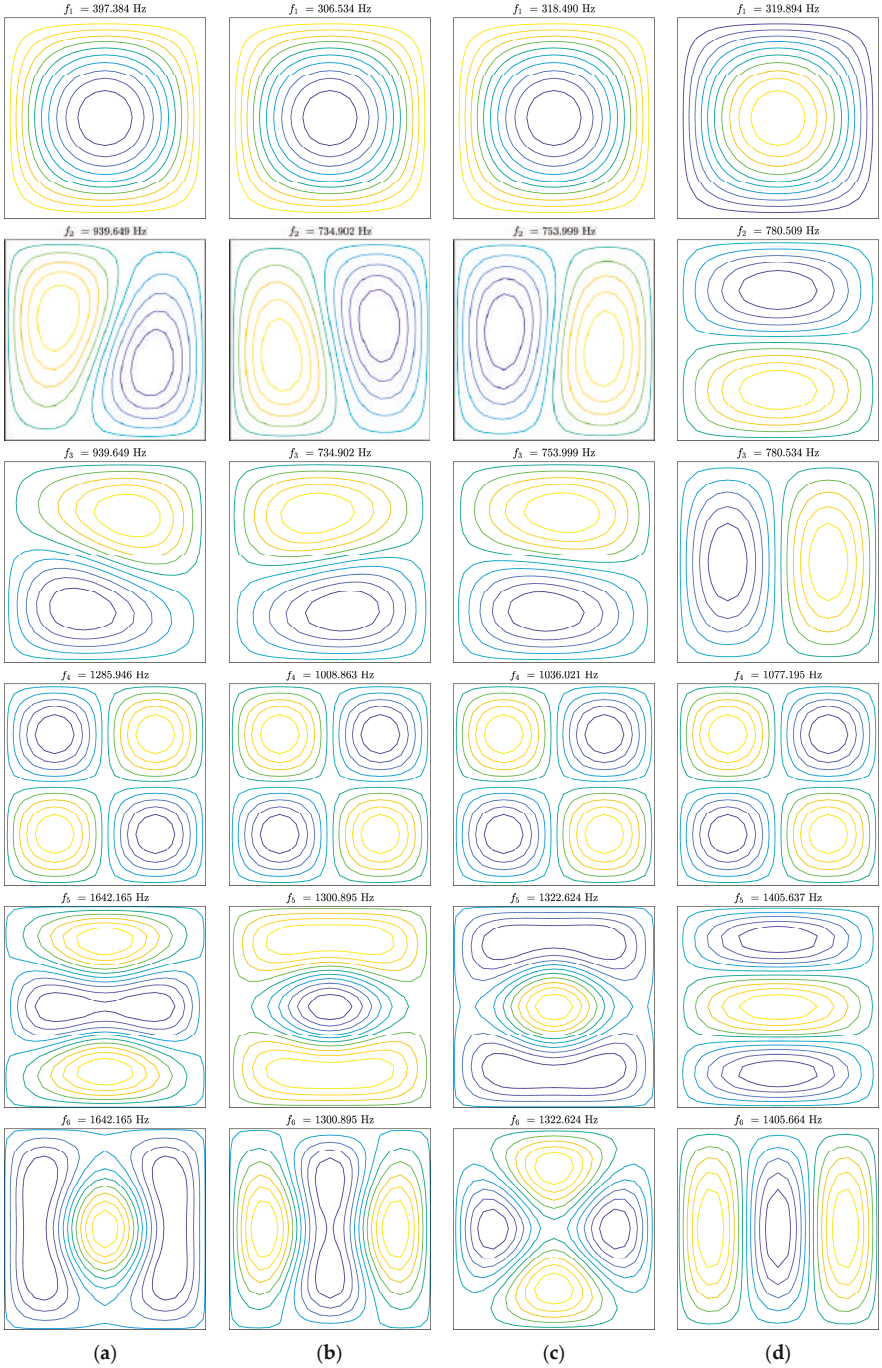

Figure 6. First six mode shapes for a simply-supported laminated thick plate with different fiber distributions: (**a**) Scheme 1 (uniform); (**b**) Scheme 2; (**c**) Scheme 3; (**d**) Scheme 4.

4. Conclusions

A FE formulation was presented and implemented to investigate the natural frequencies of functionally graded orthotropic thin and thick plates with cross-ply layups. The layers of the structures were modeled as fiber-reinforced materials with orthotropic features. The fibers were characterized by a gradual variation of their volume fraction along the thickness of the plates. Toward this aim, several functions depending on the thickness coordinate were introduced. Their effects on the free vibrations were discussed. The research proved that the natural frequencies, as well as the corresponding mode shapes, were affected by the non-uniform placement of the fibers in the thickness direction. In particular, the dynamic response of laminated plates could be changed by varying the through-the-thickness distributions of the volume fraction of the reinforcing fibers, keeping the fiber orientation and the thickness of the various layers constant. The same considerations were deduced for thin and thick plates.

Author Contributions: Conceptualization, M.B. and A.M.T.; methodology, M.B. and A.M.T.; software, M.B. and A.M.T.; validation, M.B. and A.M.T.; formal analysis, M.B. and A.M.T.; investigation, M.B. and A.M.T.; resources, M.B. and A.M.T.; data curation, M.B. and A.M.T.; Writing—Original Draft preparation, M.B. and A.M.T.; Writing—Review and Editing, M.B. and A.M.T.; visualization, M.B. and A.M.T.; supervision, M.B. and A.M.T.; project administration, M.B. and A.M.T.

Funding: This research received no external funding.

Conflicts of Interest: The authors declare no conflict of interest.

Appendix A

The following definitions are required to compute the terms of the element stiffness matrix $\mathbf{K}^{(e)}$ introduced in Equation (31). Recall that the operator at issue is symmetrical. The submatrices $\mathbf{K}_{ij}^{(e)}$ for $i, j = 1, 2, \ldots, 5$ assume the following aspects:

$$\begin{aligned}
\mathbf{K}_{11} &= \int_x \int_y \Big(\mathbf{B}_x^T\Big(A_{11}\mathbf{B}_x + A_{16}\mathbf{B}_y\Big) + \mathbf{B}_y^T\Big(A_{16}\mathbf{B}_x + A_{66}\mathbf{B}_y\Big)\Big)dxdy \\
\mathbf{K}_{12} &= \int_x \int_y \Big(\mathbf{B}_x^T\Big(A_{12}\mathbf{B}_y + A_{16}\mathbf{B}_x\Big) + \mathbf{B}_y^T\Big(A_{26}\mathbf{B}_y + A_{66}\mathbf{B}_x\Big)\Big)dxdy \\
\mathbf{K}_{13} &= 0 \\
\mathbf{K}_{14} &= \int_x \int_y \Big(\mathbf{B}_x^T\Big(B_{11}\mathbf{B}_x + B_{16}\mathbf{B}_y\Big) + \mathbf{B}_y^T\Big(B_{16}\mathbf{B}_x + B_{66}\mathbf{B}_y\Big)\Big)dxdy \\
\mathbf{K}_{15} &= \int_x \int_y \Big(\mathbf{B}_x^T\Big(B_{12}\mathbf{B}_y + B_{16}\mathbf{B}_x\Big) + \mathbf{B}_y^T\Big(B_{26}\mathbf{B}_y + B_{66}\mathbf{B}_x\Big)\Big)dxdy
\end{aligned} \tag{A1}$$

$$\begin{aligned}
\mathbf{K}_{21} &= \mathbf{K}_{12}^T \\
\mathbf{K}_{22} &= \int_x \int_y \Big(\mathbf{B}_y^T\Big(A_{22}\mathbf{B}_y + A_{26}\mathbf{B}_x\Big) + \mathbf{B}_x^T\Big(A_{26}\mathbf{B}_y + A_{66}\mathbf{B}_x\Big)\Big)dxdy \\
\mathbf{K}_{23} &= 0 \\
\mathbf{K}_{24} &= \int_x \int_y \Big(\mathbf{B}_y^T\Big(B_{12}\mathbf{B}_x + B_{26}\mathbf{B}_y\Big) + \mathbf{B}_x^T\Big(B_{16}\mathbf{B}_x + B_{66}\mathbf{B}_y\Big)\Big)dxdy \\
\mathbf{K}_{25} &= \int_x \int_y \Big(\mathbf{B}_y^T\Big(B_{22}\mathbf{B}_y + B_{26}\mathbf{B}_x\Big) + \mathbf{B}_x^T\Big(B_{26}\mathbf{B}_y + B_{66}\mathbf{B}_x\Big)\Big)dxdy
\end{aligned} \tag{A2}$$

$$\begin{aligned}
\mathbf{K}_{31} &= \mathbf{K}_{13}^T \\
\mathbf{K}_{32} &= \mathbf{K}_{23}^T \\
\mathbf{K}_{33} &= \int_x \int_y \Big(\mathbf{B}_x^T\Big(\kappa A_{44}\mathbf{B}_x + \kappa A_{45}\mathbf{B}_y\Big) + \mathbf{B}_y^T\Big(\kappa A_{45}\mathbf{B}_x + \kappa A_{55}\mathbf{B}_y\Big)\Big)dxdy \\
\mathbf{K}_{34} &= \int_x \int_y \Big(\mathbf{B}_x^T\Big(\kappa A_{44}\overline{\mathbf{N}}\Big) + \mathbf{B}_y^T\Big(\kappa A_{45}\overline{\mathbf{N}}\Big)\Big)dxdy \\
\mathbf{K}_{35} &= \int_x \int_y \Big(\mathbf{B}_x^T\Big(\kappa A_{45}\overline{\mathbf{N}}\Big) + \mathbf{B}_y^T\Big(\kappa A_{55}\overline{\mathbf{N}}\Big)\Big)dxdy
\end{aligned} \tag{A3}$$

$$\begin{aligned}
\mathbf{K}_{41} &= \mathbf{K}_{14}^T \\
\mathbf{K}_{42} &= \mathbf{K}_{24}^T \\
\mathbf{K}_{43} &= \mathbf{K}_{34}^T \\
\mathbf{K}_{44} &= \int_x \int_y \left(\mathbf{B}_x^T\left(D_{11}\mathbf{B}_x^e + D_{16}\mathbf{B}_y\right) + \mathbf{B}_y^T\left(D_{16}\mathbf{B}_x + D_{66}\mathbf{B}_y\right)\right)dxdy + \int_x \int_y \overline{\mathbf{N}}^T \kappa A_{44}\overline{\mathbf{N}}dxdy \\
\mathbf{K}_{45} &= \int_x \int_y \left(\mathbf{B}_x^T\left(D_{12}\mathbf{B}_y + D_{16}\mathbf{B}_x\right) + \mathbf{B}_y^T\left(D_{26}\mathbf{B}_y + D_{66}\mathbf{B}_x\right)\right)dxdy + \int_x \int_y \overline{\mathbf{N}}^T \kappa A_{45}\overline{\mathbf{N}}dxdy
\end{aligned} \tag{A4}$$

$$\begin{aligned}
\mathbf{K}_{51} &= \mathbf{K}_{15}^T \\
\mathbf{K}_{52} &= \mathbf{K}_{25}^T \\
\mathbf{K}_{53} &= \mathbf{K}_{35}^T \\
\mathbf{K}_{54} &= \mathbf{K}_{45}^T \\
\mathbf{K}_{55} &= \int_x \int_y \left(\mathbf{B}_y^T\left(D_{22}\mathbf{B}_y + D_{26}\mathbf{B}_x\right) + \mathbf{B}_x^T\left(D_{26}\mathbf{B}_y + D_{66}\mathbf{B}_x\right)\right)dxdy + \int_x \int_y \overline{\mathbf{N}}^T \kappa A_{55}\overline{\mathbf{N}}dxdy
\end{aligned} \tag{A5}$$

Analogously, the following definitions are needed to evaluate the terms of the element mass matrix $\mathbf{M}^{(e)}$ introduced in Equation (32), which also turns out to be symmetrical. The submatrices $\mathbf{M}_{ij}^{(e)}$, for $i, j = 1, 2, \ldots, 5$ assume the following aspects:

$$\begin{aligned}
\mathbf{M}_{11} &= \int_x \int_y \overline{\mathbf{N}}^T I_0 \overline{\mathbf{N}}dxdy \\
\mathbf{M}_{14} &= \int_x \int_y \overline{\mathbf{N}}^T I_1 \overline{\mathbf{N}}dxdy
\end{aligned} \tag{A6}$$

$$\begin{aligned}
\mathbf{M}_{22} &= \int_x \int_y \overline{\mathbf{N}}^T I_0 \overline{\mathbf{N}}dxdy \\
\mathbf{M}_{25} &= \int_x \int_y \overline{\mathbf{N}}^T I_1 \overline{\mathbf{N}}dxdy
\end{aligned} \tag{A7}$$

$$\mathbf{M}_{33} = \int_x \int_y \overline{\mathbf{N}}^T I_0 \overline{\mathbf{N}}dxdy \tag{A8}$$

$$\begin{aligned}
\mathbf{M}_{41} &= \mathbf{M}_{14}^T \\
\mathbf{M}_{44} &= \int_x \int_y \overline{\mathbf{N}}^T I_2 \overline{\mathbf{N}}dxdy
\end{aligned} \tag{A9}$$

$$\begin{aligned}
\mathbf{M}_{52} &= \mathbf{M}_{25}^T \\
\mathbf{M}_{55} &= \int_x \int_y \overline{\mathbf{N}}^T I_2 \overline{\mathbf{N}}dxdy
\end{aligned} \tag{A10}$$

References

1. Kardestuncer, H.; Norrie, D.H. *Finite Element Handbook*; McGraw-Hill: New York, NY, USA, 1987.
2. Duncan, W.J.; Collar, A.R. A method for the solution of oscillations problems by matrices. *Lond. Edinb. Dublin Philos. Mag. J. Sci.* **1934**, *17*, 865–909. [CrossRef]
3. Duncan, W.J.; Collar, A.R. Matrices applied to the motions of damped systems. *Lond. Edinb. Dublin Philos. Mag. J. Sci.* **1935**, *19*, 197–219. [CrossRef]
4. Hrennikoff, A. Solution of Problems of Elasticity by the Frame-Work Method. *ASME J. Appl. Mech.* **1941**, *8*, A619–A715.
5. Courant, R. Variational methods for the solution of problems of equilibrium and vibration. *Bull. Am. Math. Soc.* **1943**, *49*, 1–23. [CrossRef]
6. Clough, R.W. The finite element method in plane stress analysis. In Proceedings of the 2nd A.S.C.E. Conference in Electronics Computation, Pittsburgh, PA, USA, 8–9 September 1960.
7. Melosh, R.J. Basis for derivation of matrices for the direct stiffness method. *AIAA J.* **1963**, *1*, 1631–1637.

8. Ouakka, S.; Fantuzzi, N. Trustworthiness in Modeling Unreinforced and Reinforced T-Joints with Finite Elements. *Math. Comput. Appl.* **2019**, *24*, 27. [CrossRef]
9. Uzun, B.; Civalek, Ö. Nonlocal FEM Formulation for Vibration Analysis of Nanowires on Elastic Matrix with Different Materials. *Math. Comput. Appl.* **2019**, *24*, 38. [CrossRef]
10. Oden, J.T. *Finite Elements of Nonlinear Continua*; McGraw-Hill: New York, NY, USA, 1972.
11. Oden, J.T.; Reddy, J.N. *An Introduction to the Mathematical Theory of Finite Elements*; John Wiley: New York, NY, USA, 1976.
12. Hinton, E. *Numerical Methods and Software for Dynamic Analysis of Plates and Shells*; Pineridge Press: Swansea, UK, 1988.
13. Zienkiewicz, O.C. *The Finite Element Method*; McGraw-Hill: New York, NY, USA, 1991.
14. Reddy, J.N. *An Introduction to the Finite Element Method*; McGraw-Hill: New York, NY, USA, 1993.
15. Onate, E. *Calculo de Estruturas por el Metodo de Elementos Finitos*; CIMNE: Barcelona, Spain, 1995.
16. Hughes, T.J.R. *The Finite Element Method—Linear Static and Dynamic Finite Element Analysis*; Dover Publications: New York, NY, USA, 2000.
17. Ferreira, A.J.M. *MATLAB Codes for Finite Element Analysis*; Springer: New York, NY, USA, 2008.
18. Dezi, L.; Menditto, G.; Tarantino, A.M. Homogeneous structures subjected to successive structural system changes. *J. Eng. Mech. ASCE* **1990**, *116*, 1723–1732. [CrossRef]
19. Dezi, L.; Tarantino, A.M. Time dependent analysis of concrete structures with variable structural system. *ACI Mater. J.* **1991**, *88*, 320–324.
20. Dezi, L.; Menditto, G.; Tarantino, A.M. Viscoelastic heterogeneous structures with variable structural system. *J. Eng. Mech. ASCE* **1993**, *119*, 238–250. [CrossRef]
21. Dezi, L.; Tarantino, A.M. Creep in continuous composite beams. Part I: Theoretical treatment. *J. Struct. Eng. ASCE* **1993**, *119*, 2095–2111. [CrossRef]
22. Reddy, J.N.; Miravete, A. *Practical Analysis of Composite Laminates*; CRC Press: Boca Raton, FL, USA, 1995.
23. Reddy, J.N. *Mechanics of Laminated Composite Plates and Shells—Theory and Analysis*, 2nd ed.; CRC Press: Boca Raton, FL, USA, 2004.
24. Tornabene, F.; Bacciocchi, M. *Anisotropic Doubly-Curved Shells. Higher-Order Strong and Weak Formulations for Arbitrarily Shaped Shell Structures*; Esculapio: Bologna, Italy, 2018.
25. Vinson, J.R. *The Behavior of Shells Composed of Isotropic and Composite Materials*; Springer: New York, NY, USA, 1993.
26. Jones, R.M. *Mechanics of Composite Materials*, 2nd ed.; Taylor & Francis: Philadelphia, PA, USA, 1999.
27. Christensen, R.M. *Mechanics of Composite Materials*; Dover Publications: New York, NY, USA, 2005.
28. Barbero, E.J. *Introduction to Composite Materials Design*; CRC Press: Boca Raton, FL, USA, 2011.
29. Chamis, C.C.; Sendeckyj, G.P. Critique on Theories Predicting Thermoelastic Properties of Fibrous Composites. *J. Compos. Mater.* **1968**, *2*, 332–358. [CrossRef]
30. Halpin, J.C. Effects of Environmental Factors on Composite Materials. Available online: http://citeseerx.ist.psu.edu/viewdoc/download?doi=10.1.1.844.575&rep=rep1&type=pdf (accessed on 18 May 2019).
31. Tsai, S.W. *Structural Behavior of Composite Materials*; NASA: Washington, DC, USA, 1964.
32. Tsai, S.W. *Strength Characteristics of Composite Materials*; NASA: Washington, DC, USA, 1965.
33. Hill, R. Theory of Mechanical Properties of Fibre-Strengthened Materials: I. Elastic Behavior. *J. Mech. Phys. Solids* **1964**, *12*, 199–212. [CrossRef]
34. Hill, R. Theory of Mechanical Properties of Fibre-Strengthened Materials: II. Inelastic Behavior. *J. Mech. Phys. Solids* **1964**, *12*, 213–218. [CrossRef]
35. Tornabene, F.; Bacciocchi, M.; Fantuzzi, N.; Reddy, J.N. Multiscale Approach for Three-Phase CNT/Polymer/Fiber Laminated Nanocomposite Structures. *Polym. Compos.* **2019**, *40*, E102–E126. [CrossRef]
36. Reddy, J.N.; Chin, C.D. Thermomechanical Analysis of Functionally Graded Cylinders and Plates. *J. Therm. Stresses* **1998**, *21*, 593–626. [CrossRef]
37. Reddy, J.N. Analysis of functionally graded plates. *Int. J. Numer. Methods Eng.* **2000**, *47*, 663–684. [CrossRef]
38. Reddy, J.N. Microstructure-dependent couple stress theories of functionally graded beams. *J. Mech. Phys. Solids* **2011**, *59*, 2382–2399. [CrossRef]
39. Reddy, J.N.; Kim, J. A nonlinear modified couple stress-based third-order theory of functionally graded plates. *Compos. Struct.* **2012**, *94*, 1128–1143. [CrossRef]

40. Kim, J.; Reddy, J.N. A general third-order theory of functionally graded plates with modified couple stress effect and the von Kármán nonlinearity: Theory and finite element analysis. *Acta Mech.* **2015**, *226*, 2973–2998. [CrossRef]
41. Kim, J.; Reddy, J.N. Modeling of functionally graded smart plates with gradient elasticity effects. *Mech. Adv. Mater. Struct.* **2017**, *24*, 437–447. [CrossRef]
42. Kim, J.; Zur, K.K.; Reddy, J.N. Bending, free vibration, and buckling of modified couples stress-based functionally graded porous micro-plates. *Compos. Struct.* **2019**, *209*, 879–888. [CrossRef]
43. Gutierrez Rivera, M.; Reddy, J.N. Stress analysis of functionally graded shells using a 7-parameter shell element. *Mech. Res. Commun.* **2016**, *78*, 60–70. [CrossRef]
44. Lanc, D.; Vo, T.P.; Turkalj, G.; Lee, J. Buckling analysis of thin-walled functionally graded sandwich box beams. *Thin Wall. Struct.* **2015**, *86*, 148–156. [CrossRef]
45. Lanc, D.; Turkalj, G.; Vo, T.; Brnic, J. Nonlinear buckling behaviours of thin-walled functionally graded open section beams. *Compos. Struct.* **2016**, *152*, 829–839. [CrossRef]
46. Sofiyev, A.H.; Kuruoglu, N. Dynamic instability of three-layered cylindrical shells containing an FGM interlayer. *Thin Wall. Struct.* **2015**, *93*, 10–21. [CrossRef]
47. Alibeigloo, A. Thermo elasticity solution of sandwich circular plate with functionally graded core using generalized differential quadrature method. *Compos. Struct.* **2016**, *136*, 229–240. [CrossRef]
48. Tornabene, F. Free Vibration Analysis of Functionally Graded Conical, Cylindrical Shell and Annular Plate Structures with a Four-parameter Power-Law Distribution. *Comput. Method. Appl. Mech. Eng.* **2009**, *198*, 2911–2935. [CrossRef]
49. Tornabene, F.; Viola, E. Free Vibration Analysis of Functionally Graded Panels and Shells of Revolution. *Meccanica* **2009**, *44*, 255–281. [CrossRef]
50. Tornabene, F.; Fantuzzi, N.; Viola, E.; Batra, R.C. Stress and strain recovery for functionally graded free-form and doubly-curved sandwich shells using higher-order equivalent single layer theory. *Compos. Struct.* **2015**, *119*, 67–89. [CrossRef]
51. Mercan, K.; Baltacıoglu, A.K.; Civalek, Ö. Free vibration of laminated and FGM/CNT composites annular thick plates with shear deformation by discrete singular convolution method. *Compos. Struct.* **2018**, *186*, 139–153. [CrossRef]
52. Civalek, Ö.; Baltacıoglu, A.K. Free vibration analysis of laminated and FGM composite annular sector plates. *Compos. Part B Eng.* **2019**, *157*, 182–194. [CrossRef]
53. Mróz, Z. Optimal design of structures of composite materials. *Int. J. Solids Struct.* **1970**, *6*, 859–870. [CrossRef]
54. Bert, C.W. Optimal design of a composite-material plate to maximize its fundamental frequency. *J. Sound Vib.* **1977**, *50*, 229–237. [CrossRef]
55. Bruyneel, M. A general and effective approach for the optimal design of fiber reinforced composite structures. *Compos. Sci. Technol.* **2006**, *66*, 1303–1314. [CrossRef]
56. Pelletier, J.L.; Vel, S.S. Multi-objective optimization of fiber reinforced composite laminates for strength, stiffness and minimal mass. *Comput. Struct.* **2006**, *84*, 2065–2080. [CrossRef]
57. Dong, C.; Davies, I.J. Optimal design for the flexural behaviour of glass and carbon fibre reinforced polymer hybrid composites. *Mater. Design.* **2012**, *37*, 450–457. [CrossRef]
58. Ganguli, R. Optimal design of composite structures: a historical review. *J. Indian I. Sci.* **2013**, *93*, 557–570.
59. Ke, L.-L.; Yang, J.; Kitipornchai, S. Nonlinear free vibration of functionally graded carbon nanotube-reinforced composite beams. *Compos. Struct.* **2010**, *92*, 676–683. [CrossRef]
60. Shen, H.-S. Thermal buckling and postbuckling behavior of functionally graded carbon nanotube-reinforced composite cylindrical shells. *Compos. Part B Eng.* **2012**, *43*, 1030–1038. [CrossRef]
61. Zhang, L.W.; Lei, Z.X.; Liew, K.M.; Yu, J.L. Static and dynamic of carbon nanotube reinforced functionally graded cylindrical panels. *Compos. Struct.* **2014**, *111*, 205–212. [CrossRef]
62. Liew, K.M.; Lei, Z.X.; Zhang, L.W. Mechanical analysis of functionally graded carbon nanotube reinforced composites: A review. *Compos. Struct.* **2015**, *120*, 90–97. [CrossRef]
63. Alibeigloo, A. Elasticity solution of functionally graded carbon nanotube-reinforced composite cylindrical panel subjected to thermo mechanical load. *Compos. Part B Eng.* **2016**, *87*, 214–226. [CrossRef]
64. Civalek, Ö. Free vibration of carbon nanotubes reinforced (CNTR) and functionally graded shells and plates based on FSDT via discrete singular convolution method. *Compos. Part B Eng.* **2017**, *111*, 45–59. [CrossRef]

65. Thang, P.T.; Nguyen, T.-T.; Lee, J. A new approach for nonlinear buckling analysis of imperfect functionally graded carbon nanotube-reinforced composite plates. *Compos. Part B Eng.* **2017**, *127*, 166–174. [CrossRef]
66. Zhao, J.; Choe, K.; Shuai, C.; Wang, A.; Wang, Q. Free vibration analysis of functionally graded carbon nanotube reinforced composite truncated conical panels with general boundary conditions. *Compos. Part B Eng.* **2019**, *160*, 225–240. [CrossRef]
67. Civalek, Ö.; Baltacıoglu, A.K. Vibration analysis of circular cylindrical panels with CNT reinforced and FGM composites. *Compos. Struct.* **2018**, *202*, 374–388.
68. Civalek, Ö.; Baltacıoglu, A.K. Vibration of carbon nanotube reinforced composite (CNTRC) annular sector plates by discrete singular convolution method. *Compos. Struct.* **2018**, *203*, 458–465. [CrossRef]
69. Bacciocchi, M.; Tarantino, A.M. Time-dependent behavior of viscoelastic three-phase composite plates reinforced by Carbon nanotubes. *Compos. Struct.* **2019**, *216*, 20–31. [CrossRef]
70. Fantuzzi, N.; Tornabene, F.; Bacciocchi, M.; Neves, A.M.A.; Ferreira, A.J.M. Stability and accuracy of three Fourier expansion-based strong form finite elements for the free vibration analysis of laminated composite plates. *Int. J. Numer. Methods Eng.* **2017**, *111*, 354–382. [CrossRef]
71. Tornabene, F.; Fantuzzi, N.; Bacciocchi, M. On the mechanics of laminated doubly-curved shells subjected to point and line loads. *Int. J. Eng. Sci.* **2016**, *109*, 115–164. [CrossRef]